AN ABSTRACT OF THE THESIS OF

Bethany S. Murphy for the degree of Master of Science in Geology. Presented on May 29, 2015.

Title: Upper-Crustal Magma Evolution at Intermediate Arc Systems: Uranium-Series Zircon Chronochemistry of the Unzen Volcanic Complex, Southwestern Japan

Abstract approved:

Shanaka L. de Silva

Crystal-rich (40-50 vol.%) intermediate lava has been the primary eruptive product of several recent hazardous eruptions: Mt. Pinatubo, Philippines (1991), Soufriere Hills, Montserrat (1995-present), and Unzen, Japan (1990-1995). Despite this association with such devastating eruptions, the formation, timing, and evacuation of such magma is not well understood: do such eruptions tap a long-lived, multi-cycle crystal mush, or, is it generated in a single magmatic cycle prior to eruption?

This thesis explores this question through research at the Unzen Volcanic Complex (UVC), southwestern Japan, where a 500 ka history of crystal-rich dacitic dome eruptions has built the Unzen Volcanic Complex. Previous studies (e.g. Nakamura, 1995) have demonstrated the role of mafic recharge in rejuvenating crystal mush zone a few months prior to the most recent eruptions, but – until now – its formation and evolution have not been investigated using detailed geochronology. Now, this gap has been addressed through U/Th zircon geochronology and zircon chemistry studies (zircon chronochemistry) on several eruptions, spanning in age from the most recent (Heisei-Shinzan; 1990-1995) to lavas of the Older Unzen period (≥200 ka).

Zircon geochronology has revealed the protracted history and evolution of the crystal mush zone at the Unzen Volcanic Complex. Individual zircon surface-interior age pairs, together with zircon age spectra, suggest that portions of this crystal mush have been

present in the crust since at least the late Older Unzen period (≥200 ka). Significant zircon growth appears to occur throughout the eruptive hiatus (200-100 ka), suggesting that magmatic activity continued uninterrupted through this period.

Zircon chemistry shows that UVC crystals are typical of unaltered, igneous zircon, and – overall – zircon crystals show a restricted range in trace element chemistry in all eruption samples. Ti-in-zircon temperatures show that zircon crystalizes from a low temperature (≤790˚C) magma, in agreement with previous temperatures estimates for UVC upper-crustal magma (e.g. Venezky and Rutherford 1999). Subtle variations in trace element chemistry are observed in titanium and hafnium content through time: titanium contents show a moderate negative correlation with time, while hafnium shows a moderate positive correlation. This suggests that the crystal mush zone has evolved towards a more mature, heterogeneous system. Additionally, Older Unzen eruption samples show restricted chemistry, suggesting that crystallization occurred in a more homogenous, less evolved and possibly warmer crystal mush, compared to zircon of Younger Unzen (100 ka – present) that record variable storage conditions skewed towards a more evolved, poorly-mixed crystal mush. Complex age populations, particularly from samples of the Younger Unzen period, suggest that localized regions within the crystal mush may have different thermal histories. These results lead to the conclusion that eruptions at Unzen are tapping a mature and long-lived, multi-cycle mush of significant longevity.

Upper-Crustal Magma Evolution at Intermediate Arc Systems: Uranium-Series Zircon Chronochemistry of the Unzen Volcanic Complex, Southwestern Japan

by
Bethany S. Murphy

A THESIS
submitted to
Oregon State University

in partial fulfillment of
the requirements for the
degree of

Master of Science

Presented May 29, 2015
Commencement June 2015

Master of Science thesis of Bethany S. Murphy presented on May 29, 2015.

APPROVED:

Major Professor, representing Geology

Dean of the College of Earth, Ocean, and Atmospheric Sciences

---

Dean of the Graduate School

I understand that my thesis will become part of the permanent collection of Oregon State University libraries. My signature below authorizes release of my thesis to any reader upon request.

Bethany S. Murphy, Author

ACKNOWLEDGEMENTS

This project would not have been possible without the support and guidance of many individuals. First and foremost, I would like to express my gratitude to my advisor, Shan de Silva, for giving me the opportunity to come to Oregon State and work on such a fascinating volcanic system. Shan's mentorship has allowed me to grow both as an academic and as a field geologist, and I appreciate the significant time he has invested in helping me create a successful and exciting research project.

I would also like to thank Adam Kent and Frank Tepley for serving on my committee and providing valuable advice for improving my work. Both have also served as exceptional instructors in my coursework here at Oregon State, and I am grateful for their guidance.

I would like to thank the many individuals from the Geological Survey of Japan and Kyushu University that made my summer fieldwork at Unzen a success, particularly Shinji Takarada, Takeshi Matsushima, and Hiroshi Shimizu. I would also like to thank all of the staff from the Unzen Area GeoPark and the Shimabara community for graciously sharing their work and city with me.

A heartfelt thank you to my research group: Adonara Mucek, Zakk Carter, Dan Miggins, Jason Kaiser, Stephanie Grocke, Dale Burns, and Michelle Neely. Their doors have always been open for advice. In particular, I would like to thank Ado for her exceptional support throughout the past two years, both as a research-mate and friend. I would also like to express my gratitude to my friend, Dan, whom invested a significant amount of his time helping me learn and improve my laboratory skills. Thank you, also, to all of the VIPERs for sharing your knowledge and friendships.

This project would not have been possible without the dedication of many individuals across numerous laboratories: Matthew Coble and the staff at Stanford's SHIRMP-RG Lab, Adam Kent and the staff at OSU's W.M. Keck Laboratory for Plasma Spectrometry, Kari Cooper and Allison Rubin at the UC-Davis Interdisciplinary Center for Inductively-Coupled Plasma Mass Spectrometry, and Anthony Koppers and the staff at OSU's Argon Geochronology Laboratory.

Thank you to all of the CEOAS faculty and students with whom I've shared classes, projects and friendships. Shout-out to Taylor House and my friends from the Caves. Thank you for making my time at Oregon State bright.

A final thank you to my family for always supporting me in my endeavors.

TABLE OF CONTENTS

TABLE OF CONTENTS (CONTINUED)

LIST OF FIGURES

Figure Page

LIST OF TABLES

1 Introduction

Constraining the timescales of upper-crustal magma formation and evolution at intermediate arc systems is vital for modeling volcanic systems, providing insight into the volcanic-plutonic connection, and interpreting future volcanic hazards. Upper crustal magma is stored in a cold, crystal-rich state known as "crystal mush" (e.g. Bachmann and Bergantz 2008). The mobilization and eruption of crystal mush has produced several notable recent eruptions: Mt. Pinatubo, Philippines (1991; Pallister et al., 1992), Soufriere Hills, Montserrat (1995 to present; Murphy et al., 2000), and Mt. Unzen, Japan (1990 to 1995; Nakada et al., 1999). These volcanoes are arc volcanic systems, generated at convergent margins where oceanic crust subducts beneath continental or oceanic crust (e.g. Eichelberger, 1978). Numerous volcanoes in this genre are located in close proximity to populated regions and pose a significant risk to life and property. In particular, the eruption of crystal-rich lava produces repeated dome building and collapse events that can trigger thousands of pyroclastic flows and lahars throughout the eruptive period, which is often protracted and can continue for years to decades (Pallister et al., 1992; Murphy et al., 2000; Nakada et al., 1999). Despite the hazardous nature of intermediate arc systems, the timescales of magma formation and evolution that feed eruptions are not well constrained.

Eruption of crystal mush can be triggered by the injection of new, high-temperature magma into the base of cold, upper-crustal chambers. The timescales of recharge to eruption are short, on the order of days to decades for small (≤1 km^3 DRE) eruptions (e.g. Venezky and Rutherford, 1999; Kent et al., 2010; Tepley et al., 2013; Tomiya et al., 2013). However, the timescales associated with the formation and residence of upper-crustal crystal mush – which may represent the majority of erupted material (e.g. Bachmann and Bergantz, 2006) – are still not well understood. Do eruptions at intermediate arc systems tap a shared crystal mush zone, accumulating crystals over several periods of magmatism, or does each eruption tap a magma generated in a single, isolated cycle prior to eruption? It is possible to assess the formation and evolution of crystal mush through zircon chemistry and geochronology ("chronochemistry"), a robust accessory mineral commonly found in low abundances in intermediate volcanics.

Zircon is an excellent recorder of crystallization history, as it can survive multiple cycles of magmatism and can be reliably dated through uranium-series dating. Zircon geochronology studies at volcanic systems have already demonstrated that zircon can provide valuable insight into magma evolution (e.g. *review papers*: Cooper and Reid, 2008; Simon et al., 2008). Initial zircon geochronology studies at volcanic systems focused on silicic systems with a history of producing large (≥1000 km^3 DRE) eruptions, both on the magmatic timescales leading to these large, explosive eruptions (e.g. *Taupo Volcanic Zone*: Brown and Fletcher, 1999; Charlier et al., 2003; Charlier et al., 2005; *Yellowstone Caldera*: Bindeman et al., 2001; Vazquez and Reid, 2002; *Long Valley Caldera*: Coath and Reid, 2000) and on the smaller, effusive eruptions between them (e.g. Reid et al., 1997; Simon and Reid, 2005). In recent years, these studies have branched to include smaller systems: the Aucanquilcha volcanic cluster, northern Chile (Walker et al., 2010), Mt. St. Helens, Washington, USA (Claiborne et al., 2010), and the Lassen Volcanic Complex, California, USA (Klemetti and Clynne, 2014). All of these zircon geochronology studies have demonstrated that these crystals ubiquitously predate eruptions by 10^3~10^5 years. Zircon chemistry may reveal the evolution of a waning system (i.e. Klemetti and Clynne, 2014) or one with increasing thermal flux (i.e. Claiborne et al., 2010). For this study, we propose to investigate the history and evolution of a unique sub-genre of arc volcanics: the intermediate arc system, which typically produces small volume (≤1 km^3 DRE), effusive eruptions of restricted andesitic-dacitic composition for long stretches of volcanic history (10^4~10^5 years); notable systems include the Unzen Volcanic Complex (Japan), Mt. Hood (USA), Soufriere Hills (Montserrat), and Mt. Dutton (USA) (e.g. Eichelberger et al., 1978; Kent et al., 2010). Currently, no zircon geochronology studies have been conducted on such systems, but these studies may reveal if this eruptive genre share similar magmatic histories.

Within this context, the goal of this research is to understand the history of upper-crustal magma at intermediate systems using the Unzen Volcanic Complex (Nagasaki Prefecture, Japan) as a case study. The complex has been active since 500 ka and has produced numerous crystal-rich domes of restricted andesitic-dacitic composition (Hoshizumi et al., 1999). This system is an ideal natural laboratory for this research, as it has been well-characterized after inspiring significant research interest since the 1990-1995 eruption (Nakada et al., 1999). Research on the most recent eruption suggests that it

tapped a remnant magma generated during the 1663 or 1792 eruptions (Nakamura, 1995; Nishimura et al., 2005), suggesting at least a 200 year residence. However, no detailed geochronology studies have been undertaken to test this hypothesis. Through zircon geochronology and trace element geochemistry, this research aims to reconstruct the history of upper-crustal magma formation the Unzen Volcanic Complex, and to determine if individual eruptions are sourced from a shared crystal mush of significant longevity. The results from this research will provide valuable insight into the formation and evolution of upper-crustal magma at the Unzen Volcanic Complex, which may be applied to similar intermediate arc systems.

1.1 Geologic background of the Unzen Volcanic Complex

Geologic Setting

The Unzen Volcanic Complex (雲仙岳/"UVC") is a volcanic system located on the Shimabara Peninsula of Kyushu island of southwestern Japan. The UVC is approximately 70 kilometers behind the volcanic front of the Southwest Japan Arc, where the Philippine Sea Plate collides with the Eurasian continental plate (Figure 1.1). No subduction-related seismicity has been observed beneath the volcanic system (Hoshizumi et al., 1999). Magmatism at Unzen is interpreted as a back-arc, extensional regime, where decompression-driven upwelling mantle is responsible for magma generation (Nakada et al., 1999). Kyushu, the most volcanically active of Japan's main islands, also includes the recently active volcanoes Kirishima (2011), Sakurajima (ongoing since 1955) and Aso (ongoing since 2014), all located within the volcanic front (Figure 1.1).

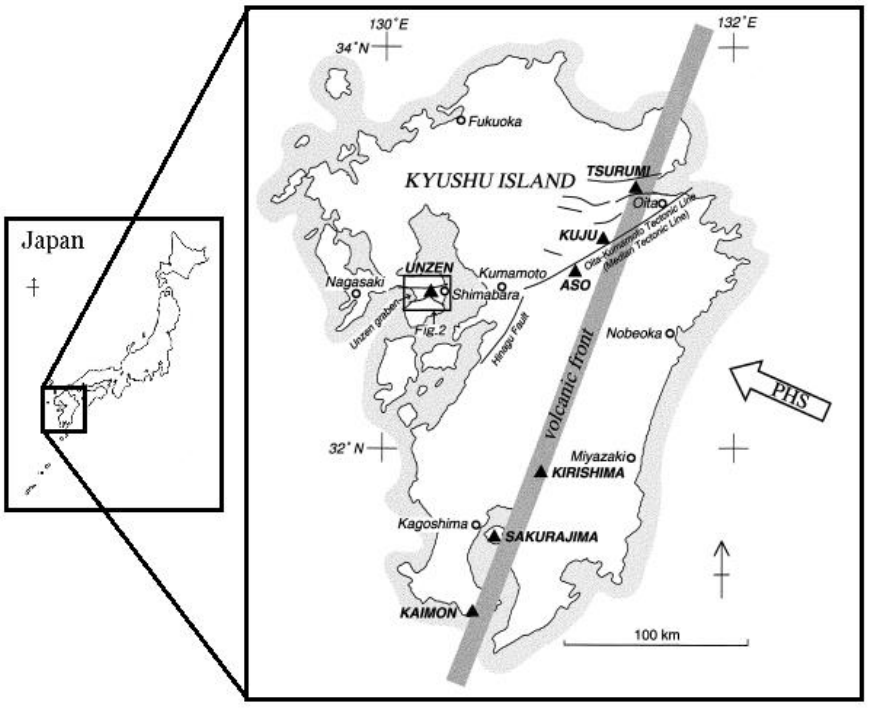

Figure 1.1 Tectonic setting of Unzen Volcanic Complex within Kyushu island. Inset map shows Kyushu's location within Japan. Arrow "PHS" shows the relative direction of the subducting Philippine Sea plate. Solid triangles are active volcanoes (Hoshizumi et al., 1999; inset map added by author).

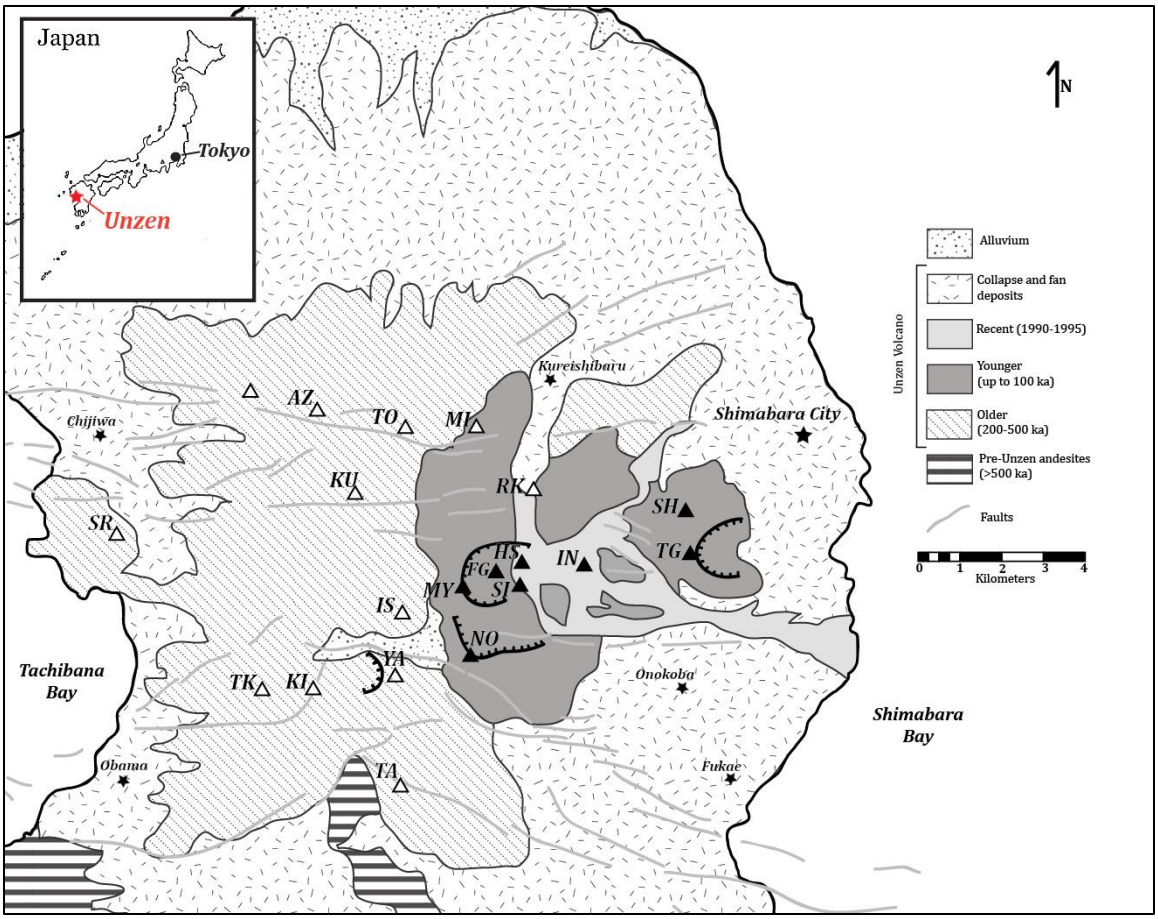

Figure 1.2 Geologic map of the Unzen Volcanic Complex, showing locations of major lava domes. Peaks of Younger Unzen are represented with a solid triangle (**HS** = Heisei-shinzan/平成新山; **FG** = Fugendake/普賢岳; **SI** = Shimanomine/島ノ峰; **IN** =Inaoyama/稲生山; **SH** = Shichimenzan/七面山; **TG** = Tenguyama/天狗山; **MY** = Myokendake/妙見岳; **NO** = Nodake/野岳). Peaks of Older Unzen domes are represented with an open triangle (**YA** = Yadake/矢岳; **KI** = Kinugasayama/絹笠山; **TK** = Takadake/高岳; **IS** = Ishiwariyama/石割山; **SR** = Sarubayama/猿葉山; **KU** = Kusenbudake/九千部岳; **RK** = Rokiyama (Rogiyama)/跨木山; **MI** =Maidake/舞岳; **TO** = Torikabutoyama/鳥甲山; **AZ** =Azumadake/吾妻岳). Figure adapted from Hoshizumi et al. (1999) and Sugimoto et al. (2005).

The Unzen Volcanic Complex is located within a volcanotectonic depression known as the Unzen Graben. It is bounded by E-W striking normal faults to the north and south, which dip towards the center of the depression (Figure 1.2). The Unzen Graben is one of several intra-arc to back-arc extensional zones that extend from northeastern Kyushu through to the Okinawa Trough, which lies southwest of Unzen (Hoshizumi et al., 1999). The compound, polygenetic volcano has a 500 ka history, although volcanism on the Shimabara peninsula has been intermittent since at least 4.6 Ma (Hoshizumi et al., 1999). The following section describes the eruptive history of the Unzen Volcanic Complex.

Overview of Geology and Eruptive History of Unzen Volcanic Complex

The Unzen Volcanic Complex has a 500 ka eruptive history that is generally divided into two periods: Older Unzen (500-200 ka) and Younger Unzen (100 ka-present) volcanoes, separated by an apparent 100 ka eruptive hiatus between 200-100 ka (Hoshizumi et al., 1999). The Pre-Unzen period (≥4.6 Ma-500 ka) was a period of intermittent volcanic activity on the Shimabara Peninsula, consisting of basaltic to andesitic lava flows interbedded with shallow marine and terrestrial deposits (Hoshizumi et al., 1999). Table 1.1 briefly summarizes the geologic history of the Shimabara Peninsula:

Stage	Substage	Units	Age
Unzen volcano	Younger	1663, 1792, 1991–95 eruptions	historical
		Myokendake, Fugendake, Mayuyama cones	150–4 ka
	Older	Maidake, Kusenbudake, Yadake cones	500–150 ka
		Sarubayama, Azumadake, Kabutoyama cones	
		Takaiwayama, Takadake, Kinugasayama cones	
Pre-Unzen volcano	Younger	Takamine, Tonosaka andesite	500 ka
		Harayama, Suwanoike basalt	
	Middle	Atagoyama, Mejima, Uwabaru, Omine basalt	2–1 Ma
		Kunisaki, Minamikushiyama andesite	
		Shobuda, Mukaigoya andesite	
	Older	Odomari, Hayasaki basalt	4 Ma

Table 1.1 Geologic history of the Shimabara Peninsula, SW Japan. See Figure 1.2 for deposit and lava dome locations (Sugimoto et al., 2005).

Pre-Unzen Period (≥4.6 Ma – 500 ka)

Deposits from the Pre-Unzen period (≥4.6 Ma – 500 ka) are exposed primarily on the southern portion of the Shimabara Peninsula. The most notable deposits of this period include the Pliocene Odomari Formation, the Kuchinotsu Group, and the Tonosaka andesite (Hoshizumi et al., 1999). The Odomari Formation is composed of basaltic andesite lava flows, siltstone, and sandstone. The oldest K–Ar date available for this group is a 4.6 Ma basalt flow (Yokoyama et al., 1982). The younger Kuchinotsu Formation overlies the Odomari Group and is composed of non-marine to shallow marine conglomerates, sandstone, and siltstone with interbedded basaltic to andesite lavas; most reported ages are between 2.0 to 1.0 Ma (Otsuka and Furukawa, 1988). Overlying these formations is the Tonosaka andesite (塔ノ坂), which is dated at 500 ka (Nakada and Kamata, 1988). This andesite is thought to represent the last volcanic activity prior to the formation of Unzen Volcanic Complex (Hoshizumi et al., 1999).

Older Unzen Period (500 ka – 200 ka)

The Older Unzen period lasted from 500 ka until approximately 200 ka. Most surface deposits date between 300-200 ka, while drill cores ages from the base of the volcano are between 500-400 ka (Hoshizumi et al., 1999). These deposits are exposed mainly on the western portion of the Shimabara Peninsula, but are covered by Younger Unzen deposits to the east (Figure 1.2). The volcanic edifice of this polygenetic volcano was once centered near the present Younger Unzen volcano edifice, but it was subsequently displaced by several faults and eroded. These deposits have been cut by E–W-trending normal faults, and the Older volcano has subsided more than 200 meters compared to the Younger volcano (Hoshizumi et al., 1999). Several lava domes were produced during this period, including Sarubayama, Kinugasayama and Kusenbudake, but many peaks have been dissected by faults and erosion. Over a 300,000 year period, the Older Unzen Volcano is estimated to have erupted ≥120 km^3 DRE of material (Nakada et al., 1999). Eruptive activity of the Older Unzen period ceased at approximately 200 ka. Erupted materials range from andesites to dacites. The eruptive activity of Older Unzen volcano is characterized mainly by effusive, thick lava flows, with few pyroclastic deposits.

Younger Unzen Period (100 ka – present)

The present period of eruptive activity is known as the Younger Unzen period (100 ka – present). There is approximately a 100 ka hiatus in eruptive activity from Older to Younger Unzen, spanning approximately 200 – 100 ka. Eruptive activity of the Younger period began at 100 ka. This period is characterized by repeated dome building and collapse events, which generated numerous pyroclastic flow deposits. Figure 1.2 details the location of Younger Unzen deposits. Nodake is the oldest volcanic center of Younger Unzen and was active from approximately 100 – 70 ka; it is preserved as an asymmetrical collapse scar (Hoshizumi et al., 1999). Myoken-dake, the next active eruptive center, appears to overlie Nodake; Hoshizumi et al. (1999) suggest that Nodake collapsed prior to the formation of the Myoken-dake volcanic center. The Myoken volcano was active between approximately 30 – 20 ka; it is preserved as a horseshoe-shaped collapse scar. Fugen-dake is the next active volcano, erupting within the scar of Myoken. It has been active since approximately 20 ka until present, most recently in 1663, 1792 and 1990-1995. Mayuyama volcano (composed of Tenguyama and Shichimenzan domes) is a separate volcano located east of Fugen-dake and formed at approximately 5 ka. Eruptive products range from andesite to dacite, including more hydrous mineral phases than during the Older Unzen period.

The historic eruptions of Unzen, centered at Fugen-dake, occurred in 1663, 1792 and 1990-1995. The 1663 eruption was an effusive lava flow (Furuyake lava/古焼け) of olivine-bearing basaltic andesite. It erupted from a vent within the Myoken collapse scar and flowed downslope for 1 kilometer to the north (Hoshizumi et al., 1999). The 1792 eruptions began with volcanotectonic earthquakes and fumarolic activity at Fugen-dake, followed by an andesitic to dacitic lava (Shinyake lava/新焼け) that flowed north-northeastward for 2 kilometers (Hoshizumi et al., 1999). One month after this eruption, a section of Mayuyama volcano, known as Tenguyama, collapsed without warning (collapse scar marked in Figure 1.2). The event is thought to have been triggered by volcano-tectonic (VT) earthquakes related to the earlier Fugen-dake eruption coupled with prior slope instability. The landslide produced a debris avalanche that devastated Shimabara City and generated a tsunami in Shimabara Bay, which struck the opposite end of the bay and reflected back to the Shimabara peninsula. In total, 15,000 people living on the coastline of

the bay were killed (Nakada et al., 1999). Within Shimabara Bay, there are numerous small islands known as the "Tsukumo-jima" (九十九島), or 99 islands, which were formed by large collapse blocks of the 1792 debris avalanche (Hoshizumi et al., 1999). The 1792 collapse of Mayuyama is remembered as the deadliest volcanic disaster in Japan's history.

1990-1995 Eruption

Unzen was dormant for nearly 200 years after the combined Shinyake lava flow and Mayuyama collapse. However, activity renewed in the late 1980s as volcano-tectonic swarms occurred with increasing frequency until eruptive activity began at the surface of Fugen-dake in November 1990. Eruptive activity continued for approximately 4 years, ceasing in 1995. This section summarizes the work of Nakada et al. (1999), which detailed the most recent eruptions. For a year prior to eruptive activity (ca. 1989), a swarm of volcano-tectonic (VT) earthquakes occurred in Tachibana Bay, west of the peninsula (Figure 1.2). A small phreatic eruption began at Fugen in November 1990 (Figure 1.3A). The focus of earthquakes migrated eastward to the summit of Fugen, becoming shallower with time. Phreatomagmatic eruptions began in February 1991, growing progressively into a dacite dome in May 1991 (Figure 1.3B). As the dome grew, it suffered repeated partial collapses. Over 9000 pyroclastic flows were generated throughout the 4 years of dome growth and collapse, flowing eastward into Shimabara City (Figure 1.3C). The total volume of magma erupted was 0.21 km^3 DRE, of which about half remained as the new dome: Heisei-shinzan (平成新山; literally "new mountain of the modern era"; Figure 1.3D). Throughout the eruption, approximately 800 buildings were destroyed by pyroclastic flows and 1700 by lahars. Lahars occurred frequently during rainy seasons throughout the 4 years of eruptive activity (Ohta, 1997). The maximum number of evacuations reached 11,000 individuals in the summer of 1991. The eruption ended in February 1995, when seismicity and effusive lava flows ceased, and the new dome began slow deformation and cooling (Nakada et al., 1999).

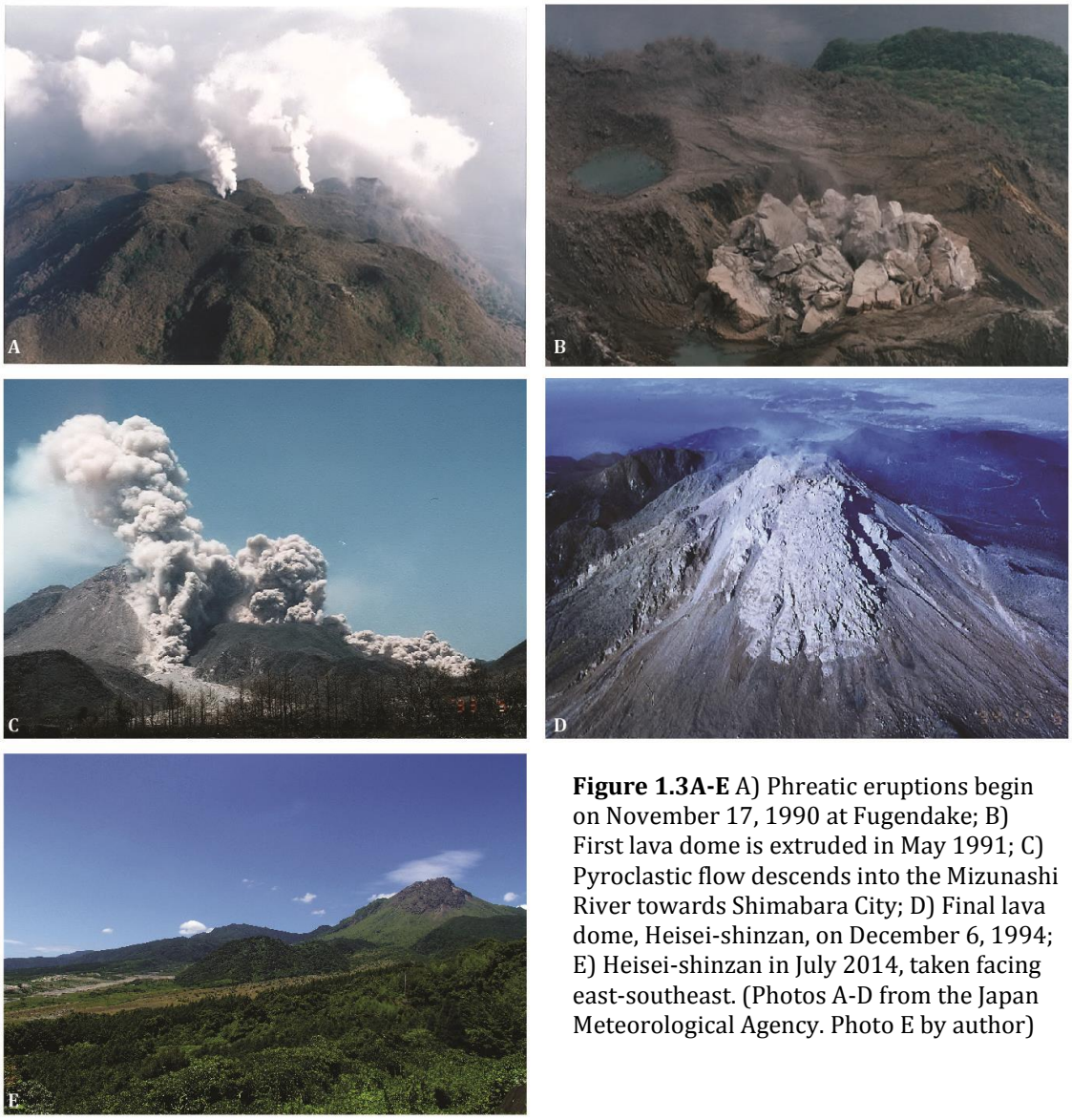

Figure 1.3A-E A) Phreatic eruptions begin on November 17, 1990 at Fugendake; B) First lava dome is extruded in May 1991; C) Pyroclastic flow descends into the Mizunashi River towards Shimabara City; D) Final lava dome, Heisei-shinzan, on December 6, 1994; E) Heisei-shinzan in July 2014, taken facing east-southeast. (Photos A-D from the Japan Meteorological Agency. Photo E by author)

Unzen magma chambers

The active magmatic system of the Unzen Volcanic Complex lies beneath the western side of the complex and Tachibana Bay (Umakoshi et al., 2001; Kohno et al., 2008). Umakoshi et al. (2001) hypothesized a model for the Unzen magmatic system using leveling surveys and the location and mechanisms of volcano-tectonic (VT) earthquakes from 1985-1995. Four magma chambers are interpreted to exist beneath the UVC. The deepest magma chamber (>15 km depth) lies beneath Tachibana Bay, west of the peninsula (Figure 1.4). During the 1990-1995 eruption, it is thought that magma (high-T endmember/recharge magma; e.g. Nishimura et al., 2005) traveled east at ~ 45˚ angle, beneath the major focal region of the VT earthquakes. A high temperature, ductile, low Q body was observed between 2-7 km depth (Figure 1.4; Umakoshi et al., 2001). This low seismicity region is likely the location the UVC upper-crustal magma chamber, which may house the low-temperature, crystal-rich magma endmember.

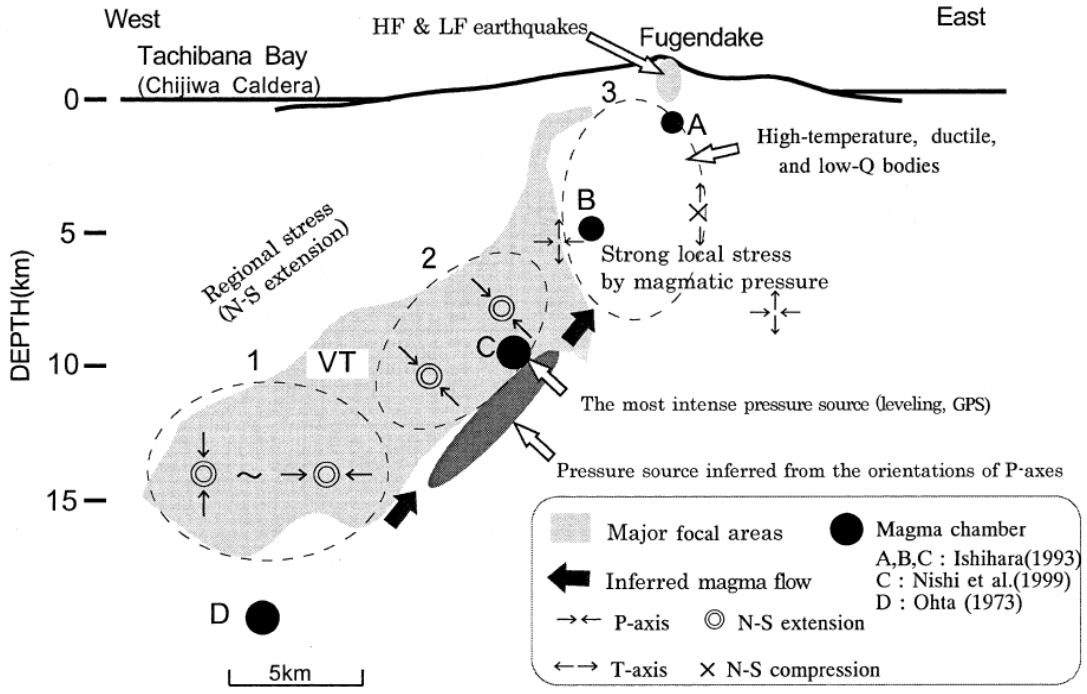

Figure 1.4 Umakoshi et al. (2001) model of the magmatic system beneath the Shimabara peninsula.

1.2 Research objectives

Past studies on the most recent (1990-1995) eruption at the Unzen Volcanic Complex (UVC) suggest that it tapped a remnant magma generated during the 1663 or 1792 eruptions (Nakamura, 1995; Nishimura et al., 2005). This implies that the formation and evacuation of material erupted during the most recent eruption occurred over a minimum period of 200~300 years. However, no detailed geochronology studies have been undertaken at the UVC to confirm this assertion. Studies at other arc volcanic systems, such as Mt. St. Helens (Claiborne et al., 2010), the Lassen Volcanic Center (Klemetti and Clynne, 2014), and the Aucanquilcha volcanic cluster (Walker et al., 2010) have demonstrated that individual crystals within a lava can predate the eruption by 10^2-10^5 years, suggesting that eruptions may source material from a crystal mush, an upper-crustal magma in "cold storage" (e.g. Bachmann and Bergantz 2006; Cooper and Kent, 2014). Within this context, the overall objective of this study is to use detailed zircon chronochemistry to reconstruct the history of upper-crustal magma that sources eruptions at the UVC. In doing so, this research aims to answer the following questions related to the evolution and residence of the UVC crystal mush:

1) Do individual domes or eruptions at the UVC tap distinct batches of magma, or do they tap a shared source?

Petrographic studies (e.g. Sugimoto et al., 2005; Browne et al., 2006) indicate that UVC lavas are remarkably similar spatially and temporally. Unzen lavas are characterized by a high crystal (35-45% phenocrysts) within a narrow range of compositions (57-67 w.t.% silica). The only major temporal distinction is that Younger Unzen deposits (100 ka – present) contain abundant hornblende and biotite phenocrysts, whereas Older Unzen deposits (500-200 ka) contain less abundant hydrous mineral phases and more pyroxenes (Hoshizumi et al., 1999). The consistent petrographic and geochemical characteristics of the lavas, within a relatively restricted area (20 x 25 km), suggest a common magma source.

2) If a single shared source is present, how long has it existed in the upper crust (i.e. magmatic longevity)?

Limited studies on active intermediate arc systems of similar age to the UVC (Mt. St. Helens, Claiborne et al., 2010; Lassen Volcanic Center, Klemetti and Clynne, 2014; Mt. Hood, Cooper and Kent 2014) suggest that upper-crustal magma can be stored in a near-solidus state for a significant period (10^4-10^5 years) and remobilized to produce eruptions. This study aims to test these estimations at the Unzen Volcanic Complex.

3) Does the UVC magmatic record reveal magmatic quiescence coindicing with the eruptive hiatus (200-100 ka)?

The existence of an eruptive hiatus at the UVC from 200-100 ka is hypothesized based on surface geology and geochronology, although it is possible that thick deposits of the Younger Unzen may cover older deposits (Hoshizumi et al., 1999). The existence of an eruptive hiatus may be supported by an absence of crystal growth during this period, indicating a corresponding lull in magmatic activity. Zircon geochronology may also be able to reveal if the end of the eruptive hiatus at 100 ka represents the emplacement of a new crystal mush, distinct from the Older Unzen period. However, zircon geochronology studies at Lassen Volcanic Center indicate that a zircon growth continued during the system's 100 ka eruptive hiatus period (Klemetti and Clynne 2014), so it may not be possible to confirm or refute the apparent eruptive hiatus at Unzen if zircon growth occurred during this period.

4) How has the magmatic system at the UVC evolved over the past 350 ka?

Trace element analysis of zircon, coupled with geochronology, can be used to determine baseline conditions of the Unzen crystal mush, such as melt temperatures during zircon crystallization, the extent of plagioclase fractionation and melt evolution. Coupled with uranium-series ages, trace element data can reveal how crystal mush storage conditions have changed through time.

1.3 Hypotheses

The primary objective of this thesis is to determine the history of the UVC crystal mush, in order to better understand the timing of the upper-crustal chamber formation and evacuation at intermediate arc systems. To do so, we tested the hypothesis that the 1990-1995 eruption at the UVC tapped a shared, multi-cycle crystal mush of significant age, which been tapped repeatedly to produce eruptions.

Hypothesis 1: A single, shared crystal mush has sourced eruptions at the Unzen Volcanic Complex.

To address this hypothesis, the first step was to collect U/Th ages from zircon surfaces and interiors from each sample. Secondly, trace element analysis of zircon crystals was collected in order to determine the crystallization conditions and geochemical traits of each sample. If each sample analyzed contained zircon crystals with overlapping age ranges and shared populations, we can be reasonably confident that all shared a common source. Additionally, trace element data revealing similar conditions of zircon crystallization and geochemical traits across samples further strengthens the argument that a single, shared upper-crustal magma chamber is tapped during eruptions.

Hypothesis 2: The UVC crystal mush was formed by the accumulation of crystals through multiple cycles of magmatism and is of significant age (>100 ka).

The use of zircon geochronology on domes of varying ages from a single system can test the presence of a long-lived, multi-cycle crystal mush. Coupled with accurate eruption ages, measured discrepancies between the age distribution of zircon crystals and eruption age can determine zircon crystallization history in magmas, as well as reveal the presence of inherited zircon (Reid et al., 1997; Bindeman et al., 2001). By analyzing the distribution and patterns of zircon surface and interior ages, it is possible to determine if the erupted material was sourced from a crystal mush with a history significantly predating eruption. Additionally, comparing age distributions from multiple samples can reveal shared histories. Zircon crystallization ages can be readily determined through uranium-series

geochronology and used to constrain the timescale of magma formation; spikes in zircon crystallization can be used to infer periods of heightened magmatism.

Hypothesis 3: The Younger Unzen period represents the evacuation of new crystal mush, separate from the Older Unzen eruptive period.

Zircon interior and surface ages can be used to determine periods of magmatic activity, when active crystal growth was occurring. The presence or absence of zircon surface-interior pairs within Younger Unzen erupted material that bridge the gap from the Older Unzen period will determine if magma sourcing Younger eruptions represents a newly emplaced magma, separate from the Older mush. Additionally, if significant growth of zircon occurred during the 200-100 ka period of hiatus, it would demonstrate that magmatic activity continued uninterrupted and may suggest the apparent eruptive hiatus at the UVC should reevaluated.

Table 1.2 Table of research objectives, hypotheses and methods.

Primary Objective	Hypothesis	Methodology
Reconstruct the history and evolution of the upper-crustal magma at the Unzen Volcanic Complex	**1.** A single, shared crystal mush has sourced eruptions at the Unzen Volcanic Complex.	1. U/Th zircon geochronology: overlapping age spectra and common zircon populations 2. Zircon trace element chemistry: shared chemistry between samples
	2. The UVC crystal mush was formed by the accumulation of crystals through multiple cycles of magmatism and is of significant age (>100 ka).	1. U/Th zircon geochronology: range of individual and combined crystal ages 2. Zircon trace element chemistry: shared trace element trends across samples through time
	3. The Younger Unzen period represents the evacuation of new crystal mush, separate from the Older Unzen eruptive period.	1. U/Th zircon geochronology: absence of crystal growth during eruptive quiescence 2. Zircon trace element chemistry: distinctive chemistry between periods indicating separate evolution

2 Background: Intermediate arc systems, the Unzen Volcanic Complex, and crystal mush: Insights from zircon?

This study investigates timescales of upper-crustal magma formation, evolution and residence at intermediate arc systems. This magma is thought to remain in a low-temperature, high-crystallinity state known as "crystal mush". The following sections serve as a brief background on the main elements of this study: 1) intermediate arc systems, 2) crystal mush characteristics, 3) and using zircon as a window into crystal mush evolution.

2.1 Intermediate arc systems and the Unzen Volcanic Complex

Arc volcanic systems are formed at convergent margins, where volcanism is generated by the subduction of oceanic crust beneath either continental crust (i.e. continental arc volcanism) or other oceanic crust (i.e. island arc volcanism). Examples of continental arc systems include the Cascade Arc (USA), the Southwest Japan Arc, and the Andean Volcanic Belt; island arc systems include the Lesser Antilles Arc (Caribbean Sea) and the Izu-Bonin Arc (Japan). Often located close to populated centers, arc volcanoes pose a significant risk to life and property to nearby communities (e.g. Mt. Pinatubo, 1991, Pallister et al., 1992; Mt. Unzen, 1990-95, Nakada et al., 1999; Soufriere Hills, 1995-ongoing, Murphy et al., 2000).

Arc volcanism can be produced in the front-arc, where magma is generated through slab-derived fluid induced melting, or it can be generated in the back-arc extensional regime, where magma is generated through decompression-driven melting (Winter, 2010). While arc volcanism can generate lavas that span the complete suit of compositions, from basalt through rhyolite, intermediate compositions dominate (Eichelberger, 1978). These intermediate (andesite- low silica dacite) lavas have the potential to erupt both explosively (e.g. Mt. Pinatubo 1991 eruption) or effusively (e.g. 1990-1995 Unzen eruption). Intermediate lavas commonly are crystal-rich (20-45 vol.%) and contain phases that are completely out of chemical equilibrium with each other, such as sodic plagioclase with calcic and olivine with quartz (e.g. Eichelberger, 1978; Bachmann and Bergantz 2006; Kent et al., 2010). These characteristics, and the lack of intermediate composition melt inclusions at arc volcanoes (Reubi and Blundy 2009), have led to the hypothesis that intermediate arc lavas

are ultimately the product of magma mixing between mantle-derived basaltic and crustal-derived silicic (≥66 wt.% silica) endmember melts. Therefore, the abundant intermediate eruptive products at arc systems may be the result of bimodal magmatism between mafic and silicic endmembers.

A subset of arc volcanoes is notable for erupting only restricted ranges of intermediate lava compositions over significant time periods (10^4-10^5 years). This genre of intermediate arc systems includes the Unzen Volcanic Complex (Japan; Nakada et al., 1999), Mt. Hood (USA; Kent et al., 2010), Soufriere Hills (Monserrat; Murphy et al., 2000), and Mount Dutton (USA; Miller et al., 1999). These systems are also notable for producing primarily effusive eruptions of crystal-rich material, characterized by dome building and collapse or thick lava flows. Eruptions can be protracted, lasting from years (1990-1995 Unzen eruption; Nakada et al., 1999) to decades (1995-ongoing Soufriere Hills eruption; Murphy et al., 2000). This group of intermediate arc systems is the primary focus of this study, with the Unzen Volcanic Complex serving as a case study.

Chemical trends at the Unzen Volcanic Complex broadly resemble other arc systems (Figure 3.1). The UVC chemical trends for the major element oxides of aluminum, iron, magnesium, and calcium oxides compatible trends that mirror other major systems (Figure 2.1). Notably, Unzen shows a more restricted range in composition for these oxides at a given composition, varying only 2-3 w.t.%. Aluminum oxide (Al_2O_3) is particularly restrictive over a wide range of compositions, varying only from 19 w.t.% to 15 w.t.% from basaltic to dacitic compositions respectively. Similarly restricted compositional trends are seen at Soufriere Hills, Redoubt and Mt. Hood volcanoes for these oxides. Uniquely, Unzen rocks show a strong incompatible trend in potassium oxide (K_2O). This trend is also seen at Mt. Hood and Lassen, although both show far greater variation in K_2O at a given composition, from 1.5~2 w.t.% at a given silica content, opposed to only Unzen, which varies by ≤1 w.t%. In contrast to the restricted chemical variations of other major oxides, sodium oxide (Na_2O) contents at Unzen vary significantly at any given silica content, from 1-2 w.t.%, and there appears to be a slight incompatible trend; these variations are still within the bounds of other intermediate arc systems. Overall, the Unzen Volcanic Complex closely resembles other arc systems in major chemical trends, but shows considerably less variation in composition at any given silica content.

The chemical trends and compositional variability of minor element concentrations at the Unzen Volcanic Complex are also typical of intermediate arc systems (Figure 2.2). However, the strong incompatible trend seen in K_2O is mirrored by the trace element rubidium (Rb) at Unzen, which is also seen at Lassen, but is absent at Mt. Hood. The barium (Ba) content and incompatibility trend for Unzen, however, closely resemble all the investigated systems except Lassen, which has highly variable barium contents that are as much as two-fold higher than any other system at a given silica content. Trace elements of particular note for this study include zirconium (Zr) and hafnium (Hf). Zirconium contents at the UVC vary considerably from 90-180 ppm from 50-63 w.t.% silica, but appears to behave slightly incompatibly. More silicic compositions (>63 w.t.% silica), show more restrictive zirconium contents of 100-150 ppm. The overall range of zirconium contents is similar to other intermediate systems. Hafnium follows a similar trend as zirconium, with contents varying from 2-4 ppm until approximately 63 w.t.% silica, when it becomes restricted to 2-3 ppm. Hafnium trends at Unzen also closely follow other systems, although Lassen shows a considerable strong incompatibility trend at more silica compositions (>65 w.t.%).

While the UVC chemical trends are within the bounds of typical intermediate arc systems, several systems share other key characteristics with Unzen: the restricted chemical composition of lavas, effusive eruptive style, high crystal content, and characteristic disequilibrium textures (see following section). When considering these factors, the Unzen Volcanic Complex most closely resembles systems such as Mt. Hood (e.g. Koleszar et al., 2012), Soufriere Hills, Montserrat (e.g. Murphy et al., 2000), and Mt. Dutton, Alaska (Miller et al., 1998).

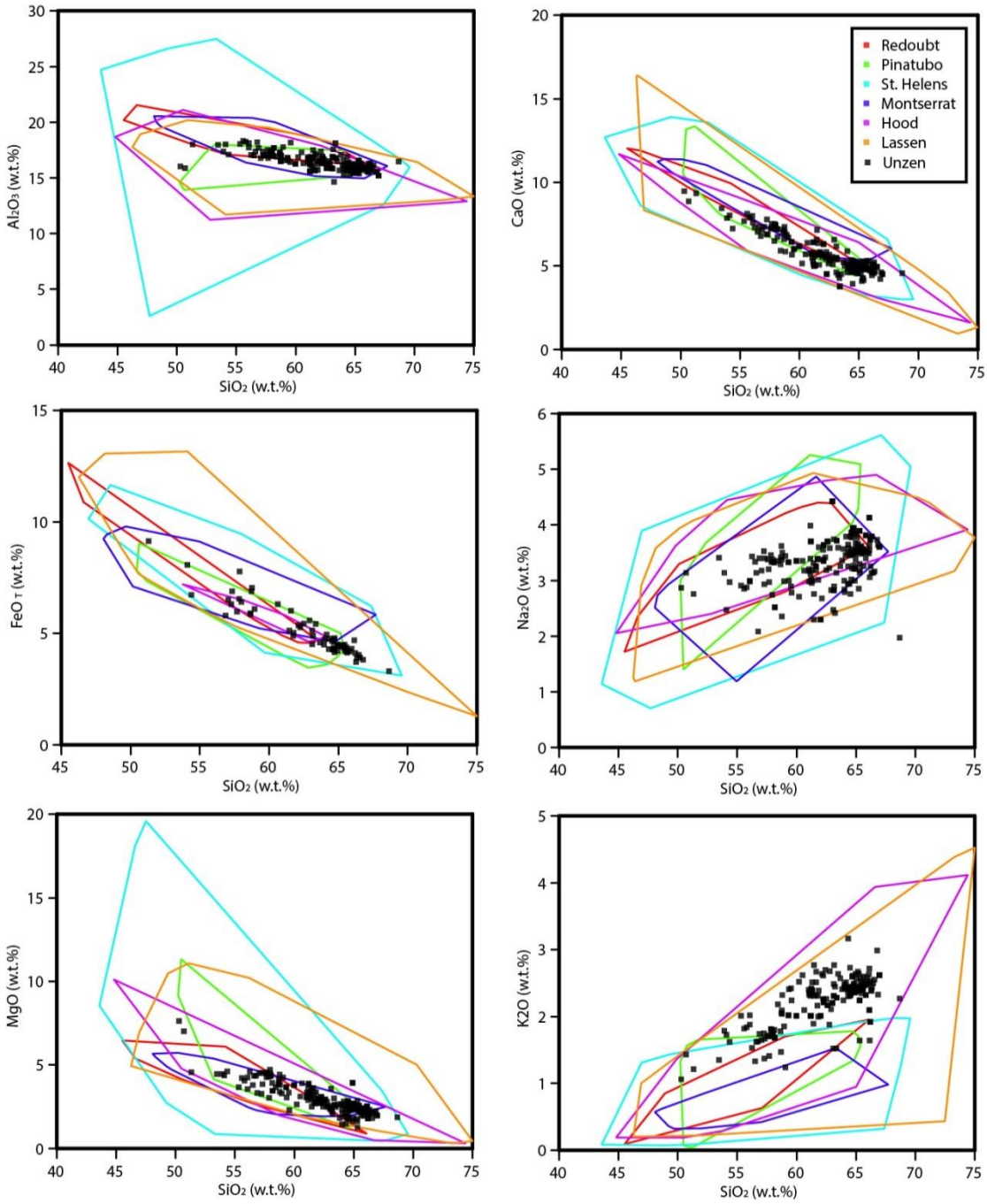

Figure 2.1. Major oxide chemical trends for the UVC (points), including mafic enclave compositions, compared to similar intermediate systems (All data acquired from EarthChemPortal: www.earthchem.org)

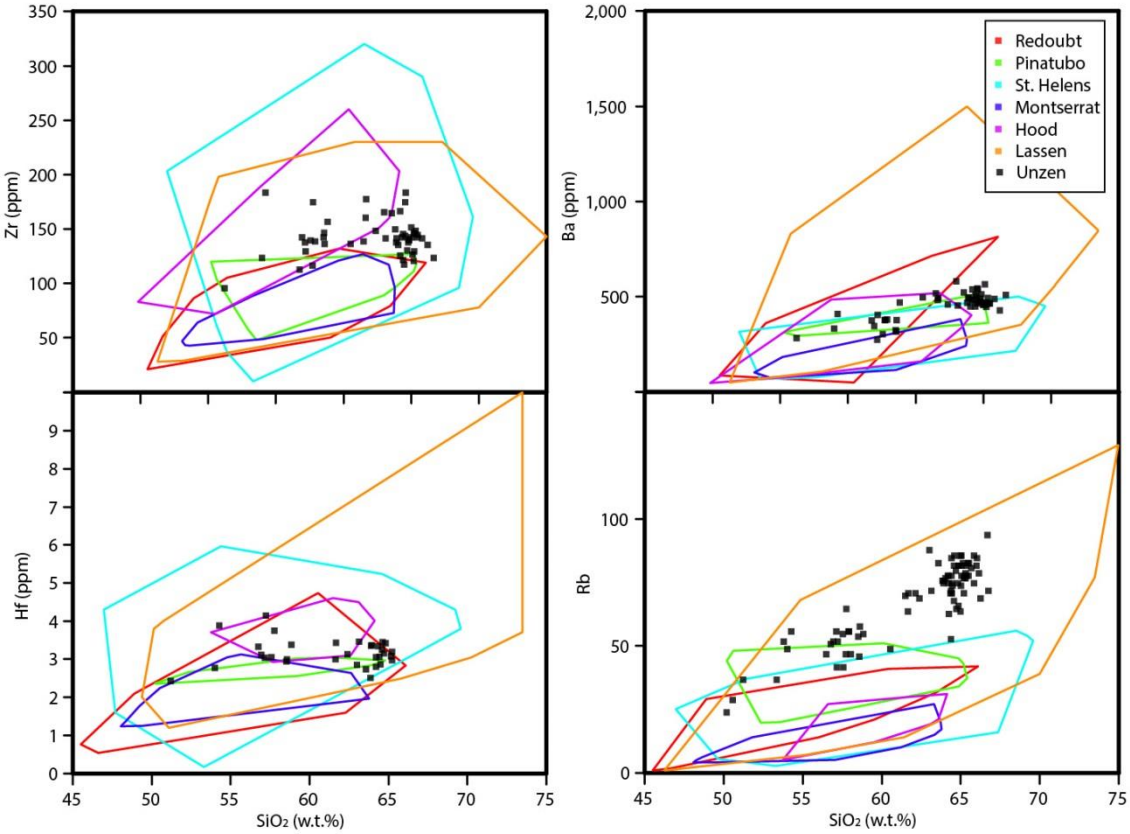

Figure 2.2 Minor/trace element chemical trends for Unzen (points), including mafic enclaves, compared to similar intermediate systems. (All data acquired from EarthChemPortal: www.earthchem.org)

2.2 Upper-crustal magma and crystal mush

Crystal mush has been defined as the crystal-rich state (25%≤N≤50~55%) of a magma before it reaches "critical crystallinity" (N=50~55%), or the rheological lock-up point at which a magma behaves as a solid (where N=vol.% crystals; Wickham 1987; Marsh 1988; Figure 2.4). At critical crystallinity, crystals within the magma become connected, eventually forming a rigid skeleton that cannot flow; Marsh (1981) argued that magmas reaching this state are no longer eruptible and, thus, destined to crystallize as a pluton. Because critical crystallinity is often cited as the upper-bound of the "crystal mush zone" for magma, it is necessary to investigate the factors that influence the rheological lockup points of magmas. While the Marsh (1988, 1996) definition approximates critical crystallinity occurring between N=50~55%, the rheological lock-up point of magmas varies based on silica content (e.g. Wickham 1987; Brophy1991; Spera 2000). Increasing silica content of a magma results in increasing viscosity, due to the polymerization effects of silica (e.g. Spera, 2000), resulting in critical crystallinities occurring at lower vol.% crystals for more silicic magmas. This is supported by observed crystallinities in worldwide lavas, as mafic lavas can erupt with higher crystallinities (up to 60~70% crystals), while rhyolitic lavas typically do not exceed crystal contents of 20~30% (Figure 2.3; Brophy 1991). Critical crystallinity also depends – to smaller extent – on crystal shape: a suspension of equant particles (such as olivine) has a lower viscosity than a suspension with the same volume of prolate or oblate particles (such as plagioclase), as the maximum packing fraction is highest for equant particles (Cimarelli et al. 2011; Meuller et al., 2011). Critical crystallinity defines the upper-limit of the Marsh (1988, 1996) "crystal-mush" zone. However, the definition of "crystal mush" has since evolved to describe magmas held in a highly-crystalline, low-temperature state, near – or even exceeding – critical crystallinity.

While Marsh (1981) argued that magmas beyond critical crystallinity are not eruptible, later petrographic, experimental and modelling studies have shown that magmas held in semi-rigid to crystal-locked states can be reactivated to produce eruptions. For example, crystal-poor rhyolites are thought to be the products of effective crystal-melt segregation from voluminous intermediate-silicic rheologically-locked magmas, through processes such as hindered settling, micro-settling and compaction (Bachmann and

Bergantz 2004). Through different processes, crystal-rich intermediate lavas can also be produced from crystal-rich, rigid magmas through "recharge". Recharge occurs when a high-temperature mafic (e.g. Kent et al., 2010; Tepley et al. 2013) or silicic (e.g. de Silva et al., 2008) magma intrudes into the base of silicic upper-crustal magma chambers. In this case, a thermal boundary layer of remobilized crystal-rich magma rapidly "defrosts" through processes such as conduction, "self-mixing" (convection within the crystal-rich magma; Couch et al., 2001), and volatile exsolution from the intruding magma (Bachmann and Bergantz 2006; Huber et al., 2010), coupled with varying degrees of magma mixing (e.g. Browne et al., 2006; Bachmann and Bergantz 2006); eruption is triggered when the thermally boundary layer becomes unstable and rises buoyantly through the overlying crystal-rich magma (Figure 2.5; Couch et al., 2001; Burgisser and Bergantz 2011). Furthermore, it has been shown at Mt. Hood, OR that upper-crustal magma at intermediate arc systems may be able to remain at near-solidus temperatures and high crystallinities (at or beyond critical crystallinity) for the majority of their storage period, while remaining readily remobilized and erupted in short recharge events (Cooper and Kent 2014). As it is now accepted that magmas at or exceeding critical crystallinity are eruptible, the definition of "crystal mush" has evolved to more generally describe a semi-rigid to rigid magma composed of a framework of interlocked crystals with interstitial liquid (e.g. Bachmann and Bergantz 2008; "rigid sponge" of Hildreth 2004).

The presence and physical architecture of magma reservoirs beneath active systems cannot be directly observed, but instead interpreted through methods such as seismic tomography (e.g. Miller and Smith 1999), observations from exposed plutonic bodies (e.g. Miller and Miller 2002), investigation of erupted materials (e.g. Couch et al., 2001), and modelling (e.g. Bachmann and Bergantz 2006). It is now thought that voluminous zones of crystal mush exist in the upper-crust beneath active volcanic systems, with ephemeral – but often absent – sizeable melt-rich regions (e.g. Bachmann and Bergantz 2008). The Marsh (1988, 1996) "crystal mush" definition is based on the "solidification front" hypothesis, which argues that crystallization increases progressively from an interior; from this perspective, the crystal mush zone is interpreted to occur in the periphery of the magma chamber with a melt-rich center. Under this definition, active magmatic systems exist as "mush columns" within a vertically-extensive system, where thick sills and stocks cool to a

highly crystalline state, commonly maintaining melt-rich interiors, which can be reactivated through regular magma flux from depth (Marsh 2000). This model may reasonably describe active magmatic systems at some hot-spot and fast-spreading mid-ocean ridges systems where melt-rich zones have been observed (Marsh 2000), but sizeable melt-rich regions are often absent at ignimbrite-producing silicic systems and arc volcanic systems (e.g. Bachmann and Bergantz 2008). Instead, magma reservoirs at these systems are thought to be stored within voluminous crystal mush zones, instead of chambers where peripheral crystal mush forms in a solidification front progressively from a melt-rich center.

Upper-crustal magma at intermediate arc systems is thought to exist as an intermediate-silicic crystal mush, at or near critical crystallinity that is typically estimated at ~50 vol.% crystals (e.g. Brophy 1991; Bachmann and Bergantz 2006; Huber et al., 2010). This mush zone is stored in the upper-crust at depths estimated between 2~7 km (e.g. Venezky and Rutherford 1999; Bachmann and Bergantz 2006; Kent et al., 2010). Study of plagioclase zoning and diffusion at Mt. Hood, OR, USA suggests that the pre-eruptive conditions of intermediate arc crystal mush may be characterized by a persistent "cold storage" state, where magma remains in highly-crystalline state at near-solidus temperatures (~700˚C); only a small fraction of magma storage duration (<<1%~12%) may be spent at temperatures above critical crystallinity (Cooper and Kent 2014). Brief mafic recharge events, occurring over timescales on the order of days to years (e.g. Nakamura 1995 at Unzen) to decades (e.g. Murphy et al., 2001 at Monserrat), act to remobilize, mix and erupt crystal mush throughout its storage duration within the upper-crust (Figure 2.5; e.g. Couch et al., 2001).

The storage of upper-crustal magma at intermediate systems is thought to occur within a semi-rigid to rigid crystal mush reservoir, where magma maintains a persistent low-temperature, high-crystallinity state for the majority of its storage duration that is punctuated by brief high-temperature recharge events. However, the timescales of crystal mush formation and storage duration at such systems have yet to be investigated.

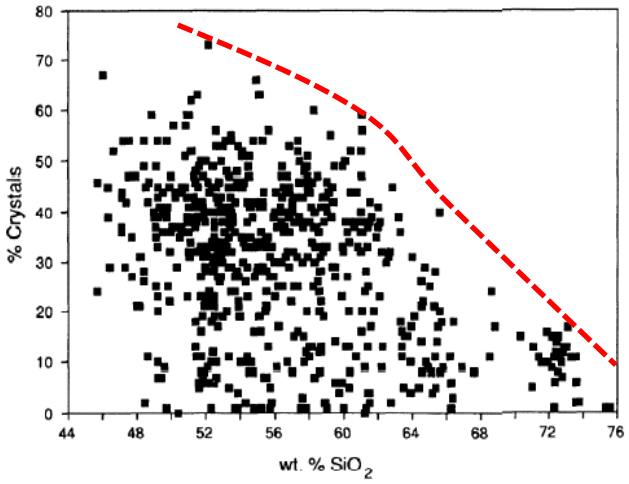

Figure 2.3 Brophy (1991) compilation of worldwide lavas, showing crystal content compared to silica content. Red line added to demonstrate the point of critical crystallinity for specific silica contents.

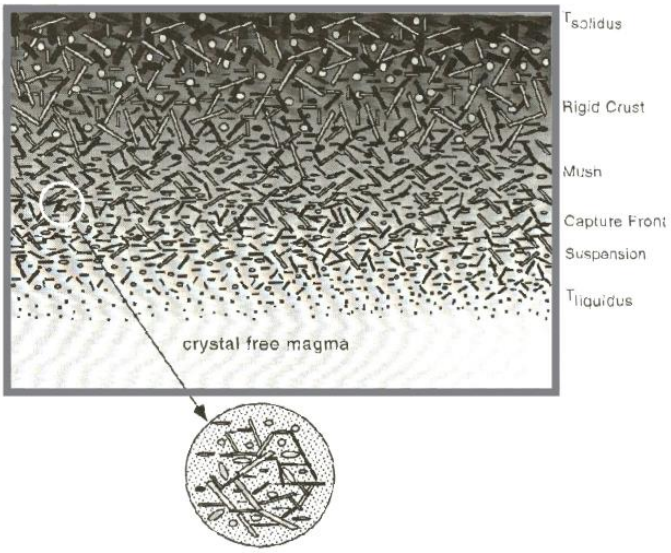

Figure 2.4 Marsh (2000) illustration of the solidification front, showing crystal mush zone. Crystal mush is defined as the point when 25%≤N≤50~55%, where N represents crystallinity. The "mush zone" is a region of high viscosity magma where crystal migration is difficult, but the magma does not yet behave rheological as a solid (which occurs at critical crystallinity, approximately N=50~55%).

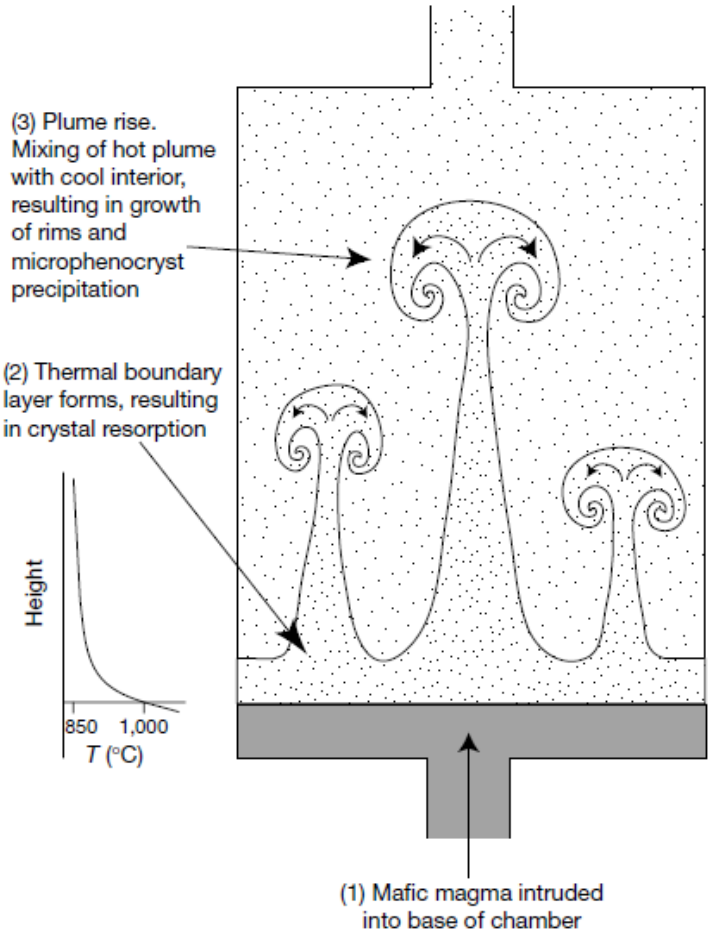

Figure 2.5 Couch et al. (2001) "self-mixing" model for crystal mush remobilization at intermediate arc systems through mafic recharge, hypothesized based petrographic and experimental evidence from the 1995-ongoing Soufriere Hills, Montserrat eruption. Here, a thermal boundary forms between the underlying high-T recharge magma and overlying low-T crystal mush; heat is transferred through conduction, forming a boundary layer that eventually grows unstable (e.g. Burgisser and Bergantz 2011 "unzipping" model) and rises buoyantly through the crystal mush. Convection within the crystal mush occurs: the plume may overturn, mixing the crystal mush, and may trigger an eruption. Not shown here, another process that can allow rapid heat exchange is volatile exsolution from the recharge magma (Bachmann and Bergantz 2006).

2.3 Zircon as a window into upper-crustal magma evolution

Addressing questions of upper-crustal magma formation and storage timescales is difficult because upper-crustal magma cannot be directly sampled, only inferred from erupted materials. Intermediate lavas from intermediate arc systems are interpreted to represent mixed magmas, with a mixture of crystals showing diverse crystallization histories, and thus are may not be representative of the pre-eruptive conditions of crystal mush (e.g. Reubi and Blundy 2009). While melt inclusions may provide insight into melt compositions during host mineral crystallization, the effects of localized melt conditions, post-entrapment crystallization, and diffusive re-equilibration can make their significance difficult to assess (Faure and Schiano, 2005; Kent, 2008; Cottrell et al. 2002; Danyushevsky et al. 2000); dating inclusions is also a challenge, so assessing changes in magmatic conditions through time is not possible. Zircon, however, may provide insight into shallow magma reservoir conditions, as it can be readily dated and geochemical traits may reveal the conditions of the melt from which it crystallized.

Zircon has long been established as a reliable chronometer through uranium-series geochronology. ^{238}U decays to ^{206}Pb through a series of shorter lived nuclides, including ^{230}Th (Figure 2.6). U/Th dating can be used to date materials between 1000-400,000 years, given the half-life of ~75 ka for the ^{230}Th daughter (Cooper and Reid 2008). U-Pb dating has been used to date materials of considerable age, up to 4.4 billion years (Harrison et al., 2005). During crystallization, zircon preferentially concentrates uranium over thorium (e.g. Mahood and Hildreth 1983). After incorporation, uranium, thorium and lead do not readily diffuse within or out of zircon at magmatic temperatures (Watson et al., 1997; Cherniak & Watson, 2001). These characteristics make zircon ideal for uranium-series dating methods. In addition to its usefulness as a chronometer, zircon chemically records the conditions of its host melt, such as temperature and chemical signature (e.g. Ferry and Watson 2007; Cooper and Reid 2008). Thus, zircon is a robust recorder of crystallization history because 1) zircon crystallizes in a magma once zirconium is saturated in the melt, which commonly occurs during the pre-eruptive history of magma chambers (Harrison and Watson, 1983), 2) zircon crystals can survive multiple cycles of magmatism, and 3) zircon dissolves rapidly in hydrous silicic melts at temperatures above zircon saturation (Harrison & Watson, 1983;

Baker et al., 2002). Coupled with age dates, zircon chemical data can record the evolution of the magma reservoir in which it crystallized.

Numerous zircon geochronology studies have been completed on volcanic systems in the past two decades in an attempt to constrain magma residence timescales. Initial studies of volcanic systems focused on silicic systems with a history of producing large (≥1000 km^3 DRE) eruptions. Studies have focused both on the magmatic timescales leading to such large, explosive eruptions (e.g. *Taupo Volcanic Zone*: Brown and Fletcher, 1999; Charlier et al., 2003; Charlier et al., 2005; *Yellowstone Caldera*: Bindeman et al., 2001; Vazquez and Reid, 2002*; Long Valley Caldera*: Coath and Reid, 2000), as well as on the smaller, effusive eruptions between them (e.g. Reid et al., 1997; Simon and Reid, 2005). All of these zircon geochronology studies have demonstrated that these crystals ubiquitously predate eruption ages by 10^3~10^5+ years. Interpretations of crystals ages from these silicic systems suggest that large (≥1000 km^3 DRE) eruptions tap a melt that evolved and evacuated in a single cycle prior to eruption. Individual large silicic eruptions from the same system are sourced from melt that differentiated and evolved independently tens of thousands of years prior to eruption; these eruptions do not tap a shared, long-standing melt-rich magma. Instead, effective crystal-melt separation from a "mushy" chamber generates a single rhyolitic melt that evolves and evacuates in a single, semi-isolated cycle (e.g. Johnson et al., 1989; Vazquez and Reid 2002; Simon and Reid 2005; Storm et al., 2011); zircon crystals from the crystal mush are not effectively entrained in the extracted melt, reflected by restricted age spectra reflecting growth from after melt separation (e.g. Simon and Reid 2005; Walker et al., 2010). The presence of older cores may indicate re-melting & eruption of older volcanics, instead of the presence of a long-standing melt (e.g. Charlier et al., 2005; Bindeman et al., 2006); the absence of zircon crystals that predate ignimbrite eruptions or "flare-up" periods in subsequent eruptions suggests the wide-scale eradication of zircon within the crystal mush (e.g. Walker et al., 2010).

Studies of post-ignimbrite smaller, effusive eruptions at these silicic systems (e.g. *Deer Mtn. and Inyo domes from Long Valley Caldera*, Reid et al., 1997; *post-2.6 Ma ignimbrite domes of the Altiplano-Puna Volcanic zone*, Tierney 2011), however, suggest that such eruptions are sourced from a common crystal mush, not a melt that has undergone effective crystal-melt separation. This is shown by overlapping age spectra and similar crystal age

populations. In recent years, zircon studies have branched to include non-ignimbrite producing systems, which suggest a similar process: the Aucanquilcha volcanic cluster, northern Chile (Walker et al., 2010), Mt. St. Helens, Washington, USA (Claiborne et al., 2010), and the Lassen Volcanic Complex (Klemetti and Clynne, 2014). These systems have often produced series of smaller (approx. ≤1 km^3 DRE) eruptions, many of which are crystal-rich intermediate-silicic lavas. These zircon studies suggest that eruptions at such systems tap a long-lived (10^4~10^5 years) crystal mush zone that is repeatedly reheated, mixed and remobilized through brief episodes (10s to 100s of years) of the magma recharge (injection of young, hotter magma). The recharge magma is likely under-saturated in zircon, reflected by the dearth of eruption-age zircon within lavas; however, the fact that zircon crystals have not been completely dissolved indicates that recharge events are short (<~100 years; e.g. Claiborne et al., 2010; Klemetti and Clynne 2014). These assertions are supported by recent work outside of zircon geochronology (i.e. uranium-series dating, crystal-size distribution and trace-element zoning of plagioclase) completed on lavas from Mt. Hood, Oregon (Cooper and Kent 2014). Cooper and Reid (2014) argue that upper-crustal magma in this setting can be stored in a near-solidus state for a significant period (10^4~10^5 years), with only a small fraction of the total magma storage duration (<<1%-12%) spent at temperatures above critical crystallinity (during recharge events).

Recharge events that manifest as eruptions at non-ignimbrite forming systems may only tap a localized region within the upper-crustal magma, reflected by complex age population distributions. The zircon ages present in any particular eruption would depend both on the physical distribution of zircon populations within the crystal mush, and the path taken by the remobilized magma as it rises through the crystal mush (e.g. Claiborne et al., 2010; Klemetti and Clynne 2014). Zircon chronochemistry can be used as a proxy for local storage conditions of the upper-crustal magma under zircon-saturated conditions, but dissolution during high-temperature, zircon-undersaturated conditions of magmatic recharge likely result in dissolution of crystals and loss of recent growth (Figure 2.7; Reid et al., 2011). Effective crystal-melt separation and the widespread eradication of zircon throughout the crystal mush during recharge events don't appear to occur commonly in these systems.

Although a promising proxy for studies on crystal mush formation and evolution, zircon's usefulness is limited by zircon crystallization conditions of its host melt. Zircon crystallization within a melt is controlled by melt composition (specifically, the cation ratio *M* and Zr contents), which determines the temperature at which a melt will begin to crystallize zircon (zircon saturation temperature, or T_{Zr}; e.g. Hanchar and Watson 2003). For a metaluminous rhyolite (*M*=1.3), T_{Zr} ranges from 900-700˚C depending on Zr contents (Reid et al., 2011). Zircon crystallization occurs in a zircon-saturated melt during (1) down-temperature cooling, (2) isothermal crystallization by water-loss, and (3) up-temperature heating during eruption if profound water exsolution occurs, inferred to be uncommon and only slight, based on slow estimated zircon growth rates of Watson (1996) (Figure 2.7; Reid et al. 2011). Zircon will not crystallize – and existing crystallize with resorb – during conditions outside of zircon-saturation such as decompression of a hydrous melt, where melt Zr content is diluted by major phase dissolution, and magma recharge events, where elevated temperatures create zircon-under saturated conditions (Figure 2.5; e.g. Reid et al., 2011).

Zircon behavior during magma recharge events is of particular interest for studies on crystal mush. During recharge events, a localized region of the crystal mush is rapidly reheated from long-term, near-solidus (≤700˚C) storage conditions (Figure 2.5). Minor up-temperature growth of zircon may be possible if zircon saturation can be maintained; however, this is unlikely because 1) down-temperature zircon crystallization during storage, which removes zirconium from the silicic melt, probably in lower zircon saturation temperature (T_{Zr}) through time, and 2) rapid heat transfer from the recharge magma may result in elevated temperatures without significant mass transfer (e.g. Bachmann and Bergantz 2006), such that the effect of increasing temperatures is not buffered by addition of Zr from the underlying magma but – instead – through zircon dissolution (Figure 2.7). Therefore, recharge conditions within the crystal mush likely favor zircon resorption, not growth (Reid et al., 2011). Because recharge events are short (typically on the order of weeks to years; e.g. Nakamura 1995 for the Unzen Volcanic Complex), complete dissolution of crystals may not occur, and erupted material will contain a complex mixture of zircon populations. After recharge, gradually cooling occurs in the local regions of the crystal mush that were affected by recharge; after reaching T_{Zr}, down-temperature zircon crystallization

may record melt evolution as the region returns to storage conditions (e.g. Reid et al. 2011; Klemetti and Clynne 2014). Therefore, zircon cannot be used as a proxy for crystal mush conditions during recharge events, as growth does not occur. However, crystal morphology shown in cathodoluminescence images – such as zoning patterns and rounding – may reveal individual crystals' histories of dissolution and growth within the crystal mush (e.g. Vavra 1990).

The complexity of zircon ages within an eruption sample have been interpreted to reflect the physical path taken by the rising remobilized mush through the upper-crustal crystal mush zone. Within the crystal mush, localized regions or pods may have experienced diverse thermal histories, as single recharge events may only reactivate a small volume of the entire storage zone (e.g. Claiborne et al., 2010). "Self-mixing" within the chamber may occur when a remobilized mush plume overturns or induces convects within the crystal mush zone, mixing diverse crystal populations with varying degrees of effectiveness (Couch et al., 2001). Even without effective mixing of the crystal mush zone, complex zircon age populations can be produced, as the physical distribution of zircon age populations within the crystal mush may not be homogeneous. In this case, the physical path taken by a rising remobilized plume through the crystal mush zone will entrain zircon from localized regions or pods with diverse histories (Claiborne et al., 2010). The complex histories of zircon populations observed in eruption samples record local storage conditions within the mush zone, which can be melt evolution by subtle variations in zircon chemistry through time (e.g. Claiborne et al., 2010; Klemetti and Clynne 2014). Zircon chronochemistry records the local evolution of the crystal mush after recharge events and throughout protracted storage in upper-crustal magma.

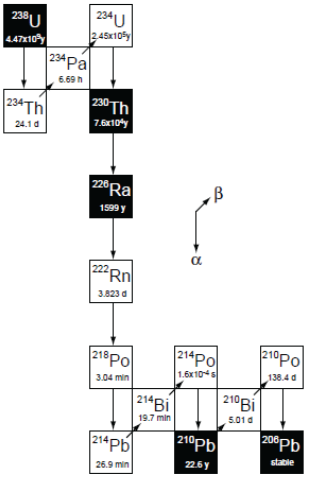

Figure 2.6 ^{238}Uranium decay series and half-lives (Cooper and Reid 2008). α indicates alpha decay (emission of an alpha particle [^4_2He] from the nucleus), and β indicates beta decay (in which a proton transforms in a neutron).

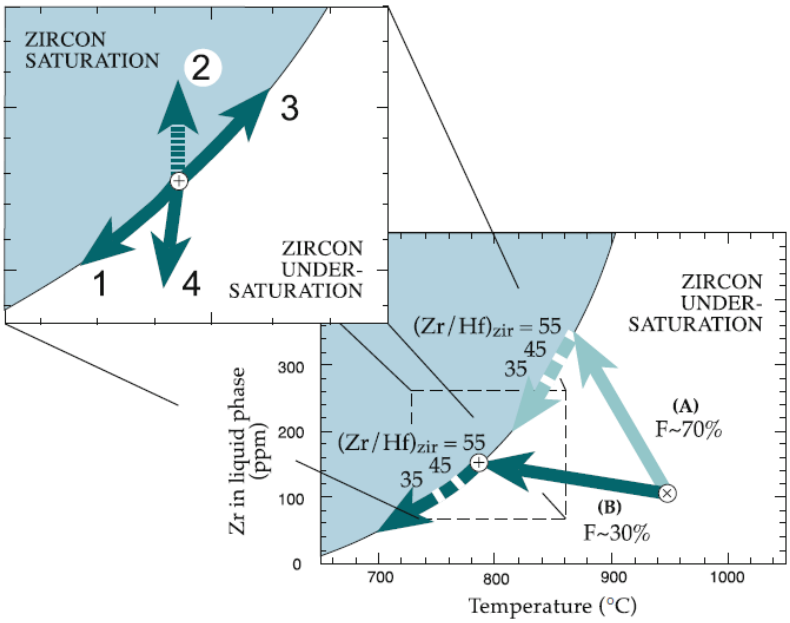

Figure 2.7 Reid et al. (2011) illustration of zirconium-temperature trajectories of melts in the context of zircon saturation (T_{Zr}) fields assuming Zr is incompatible in major phases, shown here for a metalumious rhyolite of *M*=1.3. The main figure shows changes in Zr/Hf of zircon in two hypothetical melts (⊗) labeled by the amount of fractionation before reaching T_{Zr}, with melt A of lower P_{H2O}. The inset figure shows possible Zr-T histories for a melt (⊗) that is zircon-saturated: (1) crystallization by cooling; (2) isothermal crystallization by water-loss (Zr concentration is actually buffered by zircon crystallization, but is shown as an arrow); (3) resorption through heating, as during magma recharge events (possible up-temperature growth during eruption with profound water exsolution); (4) resorption by decompression of a hydrous melt as Zr content is diluted by major phase dissolution (Reid et al., 2011).

3 Methodology

The objective of this study is to investigate the formation and evolution of upper-crustal magma at intermediate arc systems, using the Unzen Volcanic Complex as a case study. To answer the primary research questions and gain insight into crystal mush history at Unzen Volcanic Complex, we employed a variety of methodologies, primarily focused on zircon chronochemistry. A summary of the methods employed follows below.

3.1 Fieldwork and sample collection

Samples were collected for this study during two summer season at the Unzen Volcanic Complex. Two preliminary samples collected in July 2013 by Dr. Shanaka de Silva. Additional samples were at the UVC during from July-August 2014, in collaboration with researchers from the Japan Geological Survey (AIST) and Kyushu University's Shimabara Volcano and Earthquake Observatory (SEVO). Sampling locations targeted lavas that are reported to be relatively well-preserved and to contain >58 wt.% silica (andesitic to dacitic), abundant phenocrysts (>35 vol.%), and mafic inclusions. Samples were taken directly from outcrops whenever possible and from talus if the outcrop was unreachable; in the case of talus, samples were only collected when the originating bedrock could definitively be ascertained. Rock samples were collected from over thirty lavas on the Shimabara Peninsula, including basalts and andesites from the Pre-Unzen period. Weathered and otherwise altered surfaces were chipped off in the field, and samples were cleaned with steel brushes prior to shipment. Fifteen samples were ultimately selected for shipment back to Oregon State University (Figure 3.1; Table 3; see Appendix A for a full list of samples). GPS locations (WGS84), photographs, sample descriptions, and field observations were recorded at the time of collection.

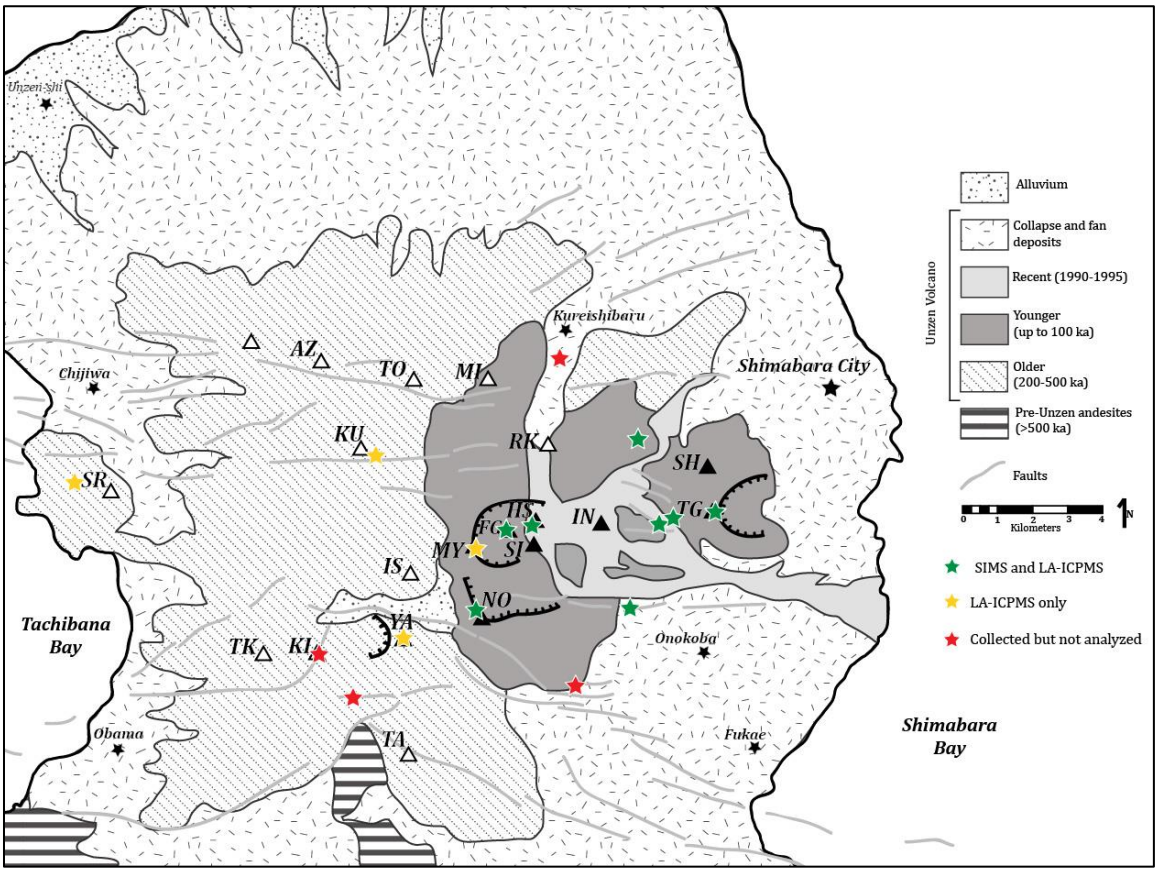

Figure 3.1. Sampling map for summer 2014 fieldwork. Note green stars indicate samples analyzed for both zircon geochronology and trace elements (SIMS and LA-ICPMS), yellow indicates samples analyzed only for zircon trace element chemistry (LA-ICPMS), and red stars indicate samples collected but not included in this research.

Sample	Sample ID	Youngest Reported Age (ka)	Age error (ka)	Age Source	Description	Lat (dec)	Long (dec)	Elevation (m)
U-HEISEI2	UNZ14032	1990-1995 AD		observed	hbl/bio dacite	32.76083	130.29820	1448
U-TENGUYAMA	**UNZ13001** UNZ14023	3	1	Hoshizumi et al. 2013	hbl/bio dacite	32.76341	130.33590	592
U-FUGEN	**UNZ13002** **UNZ14033**	3.4	0.6	Yamagata et al. 2004	hbl/bio andesite	32.75995	130.29215	1354
U-BOTANYAMA	**UNZ14013**	23	4	Unpublished K-Ar	hbl/bio dacite	32.74410	130.31644	447
U-MYOKEN	UNZ14030	28	2	Hoshizumi et al. 1999	hbl/bio dacite	32.75651	130.28568	1324
U-TARUKIHIGASHI	**UNZ14016**	25	12	Hoshizumi et al. 1999	hbl/bio dacite	32.76191	130.32874	440
U-NODAKE	**UNZ14029**	73	4	Hoshizumi et al. 1999	hbl andesite	32.74501	130.28543	1103
U-MINAMISENBONGI	**UNZ14008**	187	53	Hoshizumi et al. 1999	hbl andesite	32.77685	130.32158	369
U-KUSENBUDAKE2	UNZ14028	200	10	Watanabe et al. 1993	hbl/bio andesite	32.77392	130.26328	995
U-IWAGAMIYAMA	**UNZ14017**	213	18	Unpublished Ar-Ar	hbl/bio dacite	32.76143	130.32682	390
U-YADAKE2	UNZ14026	240	10	Watanabe et al. 1993	hbl/bio andesite	32.74117	130.26954	824
U-SARUBAYAMA	UNZ14005	260	20	Watanabe et al. 1993	hbl/bio dacite	32.77063	130.19876	376

Table 3.1 Summary of samples collected and analyzed in this study. Latitude and longitude are reported in decimal degrees (WGS84). "Hbl" = hornblende bearing; "Bio" = biotite bearing; rock types estimated in field. Bolded sample IDs indicate samples analyzed for zircon geochronology; the remaining samples were analyzed for zircon trace elements only

3.2 Thin section petrography

Thin section petrography can give insight into the whole rock chemistry of the sample and relationships between mineral phases, particularly to determine if zircon crystals are a groundmass phase or included in other mineral phases. Thin sections were prepared for all fifteen samples that were shipped to the United States. Rock billets were sent to Wagner Petrographics (sample IDS beginning with UNZ13) and Spectrum Petrographics (sample IDs beginning with UNZ14) for thin sections. Each was made to standard thickness and polished. Mineralogy and phase textures of each dome were then examined at Oregon State University using a petrographic microscope. Phase volume percentages were estimated visually (Table 5.1). Micrographs of each section were taken in both transmitted and cross-polarized light using a Nikon digital camera (DXM1200). See Chapter 4 for a discussion of UVC thin section petrology.

3.3 Zircon separation

Zircon crystals from 12 UVC lavas were separated at Oregon State University. First, whole-rock samples were crushed using a hammer, jaw crusher and mortar & pestle. The sample was sieved to retrieve the ≤250μm fraction. The ≤250μm fraction was collected into a glass beaker and rinsed repeatedly in water to remove clay-sized particles. After drying overnight, strongly magnetic minerals were removed using a hand magnet. The remaining fraction was then further separated using a Frantz machine in 0.1 amp increments from 0.4-0.7 amps. The magnetic portion was labeled and stored.

The non-magnetic portion was then further separated using standard heavy liquid separation techniques. The heavy liquid chosen was methylene iodide (M.E.I; specific gravity of 3.32). The liquid was filtered before and after separation to prevent cross-contamination. A separatory funnel was filled with M.E.I, and the non-magnetic portion of the sample was poured in. Two thorough stirrings, with a fifteen minute wait between each, were done to allow dense grains time to sink. An initial decant was performed to empty the lowest portion of the funnel into filter paper, containing the dense separate. The dense separate was then moved and rinsed thoroughly five times with acetone to remove any M.E.I residue. The final decant removed the float (light separate) and remaining M.E.I. The

float was thoroughly rinsed with acetone to remove M.E.I residue. Both separates were left overnight in the hood to evaporate any remaining M.E.I residue. The light separate was labeled and stored.

Zircon was hand-picked from the dense separate using an acupuncture needle. All identifiable zircon crystals were picked, ranging from euhedral to rounded and broken crystals. Crystals were stored in a glass vial for later preparation steps specific to the analysis method (SIMS and/or LA-ICPMS; see Chapter 5 for results).

Zircon crystals were transported and mounted on site for SIMS analysis. Preliminary samples, UNZ13001 ("Heisei-shinzan"; 1990-1995 eruption) and UNZ13002 (1792 "Mayuyama" debris avalanche), were analyzed at the University of Los Angeles, California on the Cameca IMS-1270 in March 2014. The remaining samples were analyzed at Stanford University's SHRIMP-RG (sensitive high resolution ion microprobe – reverse geometry) in December 2014. Prior to SIMS analyses, zircon crystals were rinsed in dilute HF to remove groundmass and glass at both locations. Site specific SIMS methodologies are discussed below.

3.4 $^{40}Ar/^{39}Ar$ separations

Additional mineral separates were prepared for $^{40}Ar/^{39}Ar$ geochronology of two samples: UNZ14008 ("Minami-senbongi") and UNZ14017 ("Iwagami-yama"). Both coarse-grained (250-600 micron) and fine-grained (125-250 micron) were separated for each mineral or phase. Biotite, hornblende, and plagioclase were separated from UNZ14017. Plagioclase and groundmass were separated from UNZ14008; hornblende phenocrysts appear to have undergone replacement and could not be collected.

After crushing and sieving whole-rock material to the desired size fractions (coarse and fine), samples were rinsed in water to remove dust. After drying, each whole rock sample was split using a the paper funnel method; the magnetized fraction was removed, labeled and stored. Each sample was then separated further using a Frantz machine in 0.1 amp increments from 0.2-0.6 amps; each fraction was removed, labeled and stored. The remaining material was then separated with the Frantz machine at 1.0 and 1.75 amps to remove remaining magnetic groundmass/glass and isolate plagioclase and quartz; each step and the remaining non-magnetic portion were labeled and stored.

For biotite and hornblende separates, the 0.2-0.6 amp separates were analyzed to find the most concentrated fraction of each; Frantz steps were combined to increase sample yield. The concentrated fractions were cleaned in an Ultrasonic Cleaner for approximately 10 minutes, then rinsed with water and allowed to dry overnight. Material less than 125 microns (for the fine-grained fraction) and less than 250 microns (for the coarse-grained fraction) were sieved and removed after drying. The sample was then separated using a solution of lithium heteropolytungstates and water (LST), with a density of 2.85 g/mL, to remove light phases such as feldspars and groundmass. Biotite and hornblende were split and concentrated using the Paper Shaking Method. Biotite and hornblende fractions were then hand-picked under a microscope in attempt to obtain a pure sample, free of matrix and inclusions. Biotite and hornblende contain abundant inclusions, but hand-picking was able to produce a relative pure fraction of each.

Plagioclase was collected from the non-magnetic fraction. This fraction underwent a strong acid leach using the methods of Koppers et al. (2011) to remove adhering clay minerals, glass and matrix. After leaching and rinsing, fines were sieved out (<125 microns for the fine-grained separate, and <250 microns for the coarse-grained separate). Crystals were then hand-picked under a microscope to avoid crystals with matrix and abundant inclusions.

A groundmass concentrate for UNZ14008 was separated using the combined 0.3-0.6 amp fractions. The fraction was rinsed in water, including a 10 minute ultrasonic bath, and dried overnight. This fraction also underwent a strong acid leaching similar to the plagioclase leaching. After leaching and rinsing, the groundmass was hand-picked under a microscope to avoid matrix crystals.

3.5 Host rock isotopic ratios

Host rock isotopic ratios ($^{238}U/^{232}Th$ and $^{230}Th/^{232}Th$) for the Unzen Volcanic Complex were completed at the University of California – Davis Interdisciplinary Center for Inductively-Coupled Plasma Mass Spectrometry by Dr. Kari Cooper and Allison Rubin.

Between ~0.28 to 0.35 grams of each sample was measured out for five representative UVC samples: UNZ14033, UNZ13002, UNZ13001, UNZ14029 were all whole-rock samples (125-250 μm size fraction), and UNZ14008 was a groundmass separate (150-

250 μm size fraction). Also run alongside these samples were a similar amount of two standards, AGV-2 (7) AR and BCR-2 (7) AR, and a blank to measure any contamination. All samples were dissolved in concentrated nitric acid (HNO_3), concentrated hydrofluoric acid (HF), boric acid, and perchloric acid. Following this, all samples were dried down and brought up in hydrochloric acid (HCl) and boric acid and centrifuged to separate undissolved residue from solution. This residue was isolated and the process of dissolution and centrifuging was repeated until no visible residue remained, with all solution pipetted into a clean, weighed stock bottle.

Once all samples were completely in solution, splits of each sample were removed and added to separate beakers. One split, to be analyzed for U and Th ICs, was immediately dried down; the other split, to be analyzed for U and Th IDs, was spiked with a known amount of non-natural U and Th isotopes (^{223}U and ^{229}Th) and was heated, capped, for 2 days to fully equilibrate before being dried down. Once each sample was dried, it was brought up in concentrated nitric acid, dried down, then brought up in 7M nitric acid. These samples were then through a series of ion-exchange columns (of Eichrom prefilter and Truspec resin) to isolate U and Th, which were collected separately, dried down, brought up in concentrated nitric acid, dried down, brought up in concentrated HCl, dried down, and brought up in HCl + trace HF for running on the multicollector.

All analyses were completed on a Nu Plasma multicollector inductively-coupled plasma mass spectrometer (Nu Plasma HR [Nu032] multiple-collection high-resolution double-focusing mass spectrometer ICP system), following the methods of Cooper and Donnelly (2008). $^{238}U/^{232}Th$ values for the UVC ranged from 0.519-0.680, averaging 0.624; $^{230}Th/^{232}Th$ values ranged from 0.642-0.680, averaging 0.667 (Table 3.2). Given the restricted range in values, average isotopic ratios were used in all model age calculations: $^{238}U/^{232}Th = 0.62\pm0.005$, and $^{230}Th/^{232}Th = 0.67\pm0.005$. Variability on the order of ±0.1 for either ratio introduces uncertainly on the scale of thousands of years, particularly for samples with low U/Th. However, this uncertainty does not significantly affect the main conclusions of this study.

Sample name	[U] ppm	[U] ppm, +/- %2s	[Th] ppm	[Th] ppm, +/- %2s	234U/ 238U atomic	(234U) / (238U) activity	232Th/ 230Th atomic	232/ 230 +/- 1SE	232/ 230 +/- 2SE	(238U)/ (232Th)	(230Th)/ (232Th)	(230Th)/ (238U)
UNZ 14008	1.595	0.51	7.120	0.57	5E-05	1.000	272531	372	744	0.680	0.680	1.001
UNZ 14029	1.592	0.51	7.778	0.57	6E-05	1.004	288731	422	844	0.621	0.642	1.034
UNZ 13001	1.619	0.51	7.501	0.57			275314	581	1162	0.655	0.673	1.028
UNZ 13002	1.276	0.51	7.461	0.56			276983	421	842	0.519	0.669	1.289
UNZ 14033	1.626	0.51	7.630	0.56	5E-05	1.000	275634	333	666	0.647	0.672	1.040
UVC Average										*0.624*	*0.667*	*1.078*
AGV-2 (6) AR #2	1.886	0.51	6.062	0.56			196659	188	376	0.944	0.943	0.998
AGV-2 (7) AR	1.884	0.51	6.068	0.56	5E-05	0.996	196881	273	546	0.942	0.941	0.999

Table 3.2. Host rock isotopic ratio results for the UVC and standards (AGV-2).

3.6 Secondary ion mass spectrometry (SIMS)

UCLA Cameca IMS-1270: Preliminary Analyses

Preliminary $^{238}U/^{230}Th$ measurements on zircon were conducted using secondary ion mass spectrometry (SIMS) at the University of Los Angeles, California on the Cameca IMS-1270 in March 2014. The samples analyzed using this method were UNZ13001 ("Heisei-shinzan") and UNZ13002 ("Mayuyama"). Zircon crystals were separated at Oregon State University and then transported to UCLA. At UCLA, a 1 inch aluminum disk was prepared with five ~5 mm diameter wells filled with indium metal. Unpolished zircon crystals were then gently pressed into the mount and thinly coated with Au. The mount was then placed into the SIMS where the zircons were analyzed for U/Th surface ages. After surface analysis, the mount was then polished down to 1 micron diamond grit to exposed crystal interiors and thinly coated with Au. The mount was then again placed in the SIMS and zircon crystals were analyzed for interior ages.

U–Th disequilibrium dating was performed on individual zircons using a the method of Schmitt et al. (2006). A ~40–50 nA mass-filtered O^- beam was focused into a ~35×30 µm oval spot. Secondary ions were accelerated to 12.5 keV with an energy bandpass of 50 eV and analyzed at a mass resolution of ~5000 using an axial electron multiplier collector in peak jumping mode. For each session, relative sensitivities for ^{238}UO and ^{232}ThO were calibrated by measuring the radiogenic $^{206}Pb/^{208}Pb$ ratio of concordant reference zircons AS-3 and 91500 (Paces and Miller, 1993; Wiedenbeck et al., 1995). Raw intensities were corrected for electron multiplied dead-time (25 ns). Background corrections for ^{230}ThO were performed using the averaged intensities measured on two mass stations at 244.038 and 246.300 amu. Intermittently analyzed standard zircons AS-3 and 91500 yielded

(^{230}Th)/(^{238}U) activities that were in secular equilibrium within uncertainty. No coupled age-chemistry data was collected for UNZ13001 and UNZ13002. Host rock isotopic ratios are not currently available for the Unzen Volcanic Complex, but samples have been sent to University of California, Davis in order to properly constrain these values; due to delays in analyses, these values are not presently available (May 2015). Average values for host rock isotopic values were used: ^{238}U/^{232}Th = 0.62±0.005, and ^{230}Th/^{232}Th = 0.67±0.005.

Stanford University SHRIMP-RG

^{238}U/^{230}Th and trace element measurements on zircon were conducted using SIMS at the Stanford University on the SHRIMP-RG in December 2014. Six samples were analyzed for surfaces and interiors: UNZ14016 (Taruki-higashi), UNZ14017 (Iwagamiyama), UNZ14008 (Minami-senbongi), UNZ14013 (Botanyama), UN14Z029 (Nodake), and UNZ14033 (Fugen-dake). Zircon crystals were washed in dilute HF to remove groundmass and glass prior to mounting. Unpolished crystals were gently pressed into an indium round mount and thinly coated with Au. After initial analysis, the mount was polished down to 1 micron diamond grit and cathodoluminescence images were taken of each crystal before re-analysis.

The mount was placed in the SIMS and analyzed for coupled U/Th and trace element measurements. Secondary ions were sputtered from the target spot using an O_2- primary ion beam, which was accelerated at 10 kV and had an intensity varying from 13 to 15 nA. The primary ion beam sputter pit was 35x30 microns in size and a depth of ~2-3 microns for the analyses performed in this study. The duration of each analysis was approximately 35 min, which included a 30 second pre-sputtering of the sample surface by rastering the primary beam, and the primary and secondary auto-tuned to maximize transmission. The acquisition routine includes analysis of ^{30}Si^{16}O$^+$, ^{48}Ti$^+$, ^{56}Fe$^+$, ^{89}Y$^+$, ^{155}Gd$^+$, ^{90}Zr$_2$^{16}O, ^{180}Hf^{16}O$^+$, ^{238}U$^+$, ^{232}Th^{12}C$^+$, ^{230}Th^{16}O$^+$, background measured 0.050 AMU above the ^{230}Th^{16}O$^+$ peak, ^{232}Th^{16}O$^+$, and ^{238}U^{16}O$^+$. ThC was monitored because there is a known carbide interference at both mass 244 and 246.

All peaks were measured on a single EPT® discrete-dynode electron multiplier operated in pulse counting mode. All samples were analyzed with 8 scans (peak-hopping cycles from mass 46 through 254). Measurements were made at mass resolutions of M/DM

= 7800-8400 (10% peak height), which eliminates interfering molecular species at Ti and REE peaks. Because count rates for $^{230}Th^{16}O^{+}$ are very low, 0.073 counts per second on average for unknown samples, a large (13-15 nA) primary beam current and long count times were needed to improve the counting statistics. However, the large beam current also increases secondary ion scattering, which decreases the signal to noise ratio on $^{230}Th16O+$. To minimize the background at $^{230}Th^{16}O^{+}$, the SHRIMP-RG was operated using the energy selection window to only accept high-energy ions into the collector. The energy window was moved until the signal to noise ratio for the standard MADDER (U = 3435 ppm) was >200. Although moving the energy window minimizes the background, it also cuts the total secondary ion transmission by a factor of approximately 4.

Zircon concentration for U and Th are standardized against MADDER (3435 ppm U), which is a well-characterized, homogeneous in-house zircon standards that is calibrated relative to MAD-green (Barth and Wooden, 2010). MADDER crystals were co-mounted with unknowns on each mount. Calculated $(^{238}U)/(^{232}Th)$ and $(^{230}Th)/(^{232}Th)$ ratios were calculated using $\lambda_{238} = 1.55125x10^{-7}$ ka^{-1}, $\lambda_{232} = 4.9475x10^{-8}$ ka^{-1}, $\lambda_{230} = 0.0091577$ ka^{-1}. The $(^{238}U)/(^{232}Th)$ was also corrected for instrument mass fractionation using early-erupted Bishop Tuff ("EBT"; 767.1±0.9 ka; Crowley et al., 2007), which is relatively high-U (1000-4000 ppm) and old enough that the U-Th is in secular equilibrium. For analyses measured in this session $(^{238}U)/(^{232}Th) = 0.9528±0.0026$ (1σ). Data was reduced using the Microsoft Excel add-in programs Squid2.51 and Isoplot 3.764 of Ken Ludwig (2009; 2012), with Zr has the normalizing species. Samples with high iron (> 1 ppm) were not included in the Ti or Ti-in-zircon chronochemistry results, due to the likely would of surface contamination or melt inclusion influence, which can significantly influence titanium concentrations. Average values for host rock isotopic values were used: $^{238}U/^{232}Th = 0.62±0.005$, and $^{230}Th/^{232}Th = 0.67±0.005$.

3.7 Laser ablation inductively coupled mass spectrometry (LA-ICPMS)

Zircon from 12 samples, including the 8 analyzed dated through U/Th SIMS analyses, were analyzed using laser ablation inductively coupled mass spectrometry (LA-ICPMS). In-situ unpolished surfaces and polished interiors of zircon crystals were analyzed for trace element concentrations at Oregon State University's W.M Keck Laboratory using a Photon

Machines Analyte G2 ArF 193 nanometer excimer laser coupled with a Thermo X-series II quadrupole mass spectrometer. For unpolished surface analysis, zircon crystals were mounted onto a thin section with double-sided tape. After analysis, crystals were mounted in epoxy. Prior to mounting, each crystal was investigated for spot depth (typically 5~10 microns) and re-mounted onto double-sided tape, with the analyzed crystal faces reversed so that they were facing outwards in the epoxy mount. An epoxy mount was cured over the crystals, and then polished to reveal interiors. The mount was polished down to a 1-micron diamond paste.

In-situ crystal analysis of zircon for trace element abundances was completed using the methodology of Kent et al. (2004). MADER zircon (Barth and Wooden, 2010) was used as the primary standard, and NIST-612 as a secondary standard; both were analyzed after every 10 unknowns. The spot size was a 40 micron circle, with a pulse rate of 7 Hz, 225 shots and a fluence of 4.84 J/s^2. Spot depths ranged from approximately 5~10 microns. Masses analyzed were ^{29}Si, ^{31}P, ^{49}Ti, ^{50}Ti (*), ^{56}Fe (*), ^{85}Rb (*), ^{89}Y, ^{93}Nb, ^{139}La (*), ^{140}Ce, ^{141}Pr, ^{146}Nd, ^{147}Sm, ^{153}Eu, ^{157}Gd, ^{159}Tb, ^{163}Dy, ^{165}Ho, ^{166}Er, ^{169}Tm, ^{172}Yb, ^{175}Lu, ^{178}Hf, ^{179}Hf, ^{208}Pb, ^{232}Th, and ^{238}U. Elements with asterick (*) were measured, but not included in the final data reduction due to concentrations below-detection limits in MADER standards. Typical uncertainties (st.err%) for each element range from 3~5% for abundant zircon trace elements (Y, MREE,HREE, Hf, U, Th), but range considerably for those with low concentrations: ^{31}P (~5%), ^{49}Ti (~24%), ^{89}Y (~4%), ^{93}Nb (~7%), ^{140}Ce (~4%), ^{141}Pr (~53%), ^{146}Nd (~30%), ^{147}Sm (~8%), ^{153}Eu (~6%), ^{157}Gd (~5%), ^{159}Tb (~6%), ^{163}Dy (~5%), ^{165}Ho (~4%), ^{166}Er (~4%), ^{169}Tm (~4%), ^{172}Yb (~4%), ^{175}Lu (~4%), ^{178}Hf (~4%), ^{179}Hf (~4%), ^{208}Pb (~32%), ^{232}Th (~5%), and ^{238}U (~4%). Titanium concentrations were not considered in the results or discussions of this study due to the high uncertainties in measurement and likelihood of influence by micro-inclusions or contamination.

Raw count data was reduced using in-house LaserTRAM software and assuming stoichiometric zircon SiO_2 (32.80%). The internal standard was ^{29}Si. Data were screened in LaserTRAM to monitor for the presence apatite or melt inclusions. For this reason, phosphorus (^{31}P), iron (^{56}Fe) and rubidium (^{85}Rb) were monitored as a proxy for inclusions, and any analysis with significant cps above background for these elements was discarded. Yttrium cps often steadily increased or steadily decreased during analysis, suggesting that

yttrium contents may be strongly influenced by zonation. Hitting inclusions resulted in a significant discarding of data, particularly for interior analyses. Approximately 10~20% of surfaces measurements were discarded due to cps spikes in P, Fe and Rb, and about 20~30% of interior analyses. Concentrations were calibrated using MADER zircon. Due to low concentrations of lanthanum in MADER, lanthanum concentrations could not be produced for unknown samples.

After processing, an additional ~5% of analyses were later discarded due to remaining anomalously high concentrations of P (>300 ppm), as well as high Nb concentrations (>20 ppm), which is expected to be low in abundance for zircon and is strongly influenced by the presence of apatite and melt inclusions (e.g. Jain et al., 2001; Sano et al., 2002). Anomalously high LREE concentrations were often coupled with high P (>200 ppm) and high Nb (>15 ppm). Y concentrations may also be influenced by inclusions (Jain et al., 2001). Spot analyses with elevated, outlier LREE patterns (i.e. >2σ from mean; less then 5% of spots) were not included in the results or discussion, but are available in the electronic appendix. It should be noted that MREE and HREE (Sm~Lu) of such analyses were within the range of other analyses, demonstrating that variations in LREE elements 1) is likely due to hitting inclusions, 2) does not significantly influence MREE and HREE concentrations, and 3) cannot be directly interpreted as reflecting changes in zircon or melt character (e.g. Hoskins and Schaltegger 2003).

3.8 $^{40}Ar/^{39}Ar$ geochronology

Mineral separates from 2 samples (UNZ14008/Minami-senbongi; UNZ14017/Iwagamiyama) were analyzed using $^{40}Ar/^{39}Ar$ geochronology in May 2015, in order to better constrain eruption ages; these samples produced U/Th zircon age populations during December 2014 SIMS analyses that were significantly younger than available Ar/Ar and/or K/Ar dates. Samples were separated from January-February 2015, sent for irradiation in March 2015 and analyses on the ARGUS-VI began in May 2015. Only plagioclase and groundmass phases were analyzed within the timeframe of this thesis and included in the results.

Five new $^{40}Ar/^{39}Ar$ ages were obtained by incremental heating and total fusion methods using the ARGUS-VI mass spectrometer. 2 plagioclase, 1 biotite, 1 hornblende and

1 groundmass samples were irradiated for 30 minutes in the TRIGA CLICIT nuclear reactor at Oregon State University, along with the FCT sanidine (28.201 ± 0.023 Ma, 1σ) flux monitor (Kuiper et al. 2008). Individual J-values for each sample were calculated by parabolic extrapolation of the measured flux gradient against irradiation height and typically give 0.2-0.3% uncertainties (1σ). The $^{40}Ar/^{39}Ar$ incremental heating age determinations were performed on a multi-collector ARGUS-VI mass spectrometer at Oregon State University that has 5 Faraday collectors (all fitted with 1012 Ohm resistors) and 1 ion-counting CuBe electron multiplier (located in a position next to the lowest mass Faraday collector). This allows simultaneously measurement of all argon isotopes, with mass 36 on the multiplier and masses 37 through 40 on the four adjacent Faradays. This configuration provides the advantages of running in a full multi-collector mode while measuring the lowest peak (on mass 36) on the highly sensitive electron multiplier (which has an extremely low dark-noise and a very high peak/noise ratio). Irradiated samples were loaded into Cu-planchettes (Figure 3.2) in an ultra-high vacuum sample chamber and incrementally heated by scanning a defocused 25 W CO2 laser beam in preset patterns across the sample, in order to release the argon evenly. After heating, reactive gases were cleaned up using an SAES Zr-Al ST101 getter operated at 400°C for ~10 minutes and two SAES Fe-V-Zr ST172 getters operated at 200°C and room temperature, respectively. All ages were calculated using the corrected Steiger and Jäger (1977) decay constant of 5.530 ± 0.097 x 10-10 1/yr (2σ) as reported by Min et al. (2000). For all other constants used in the age calculations, refer to Table 2 in Koppers et al. (2003). Incremental heating plateau ages and isochron ages were calculated as weighted means with 1/σ2 as weighting factor (Taylor 1997) and as YORK2 least-square fits with correlated errors (York 1969) using the ArArCALC v2.6.2 software from Koppers (2002), available from the [http://earthref.org/ArArCALC] website.

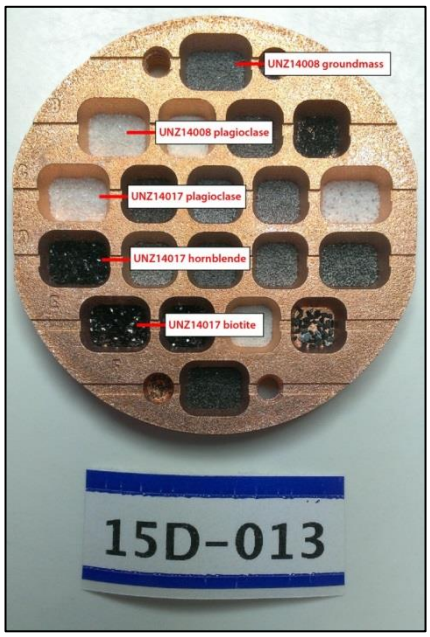

Figure 3.2 Irradiated mineral and groundmass separates from the UVC loaded into Cu-planchette prior to analyses.

3.9 Zircon saturation temperatures and Ti-in-zircon temperatures

Estimations for UVC zircon saturation temperatures and zircon crystallization temperatures (Ti-in-zircon thermometry) were calculated using established methodologies. Zircon saturation temperatures were calculated using previously published melt inclusion and groundmass glass data with the methods of Hanchar & Watson (2003). Zircon crystallization temperatures were modeled using Ti-in-zircon thermometry (Ferry and Watson 2007), assuming a silica activity of 1 and a TiO_2 activity of 0.6. Quartz is a common phenocryst in UVC lavas, so silica activity is assumed to equal 1. Most natural melts capable of crystallizing zircon have TiO_2 activity ≥0.5 (Watson and Harrison 2005), and Fe-Ti oxides are ubiquitously found in the groundmass of UVC lavas; therefore, TiO_2 activity is likely high at the UVC and an estimate value of 0.6 was used. Assuming a too low titanium activity – or a too high silica activity – results in overestimation of temperature, with an error of 0.2 in activity yielding an error of about 30 °C (e.g. Claiborne et al., 2010). These uncertainties do affect the main interpretations.

4 Geochemistry, petrology and zircon saturation temperatures

The lavas of the Unzen Volcanic Complex are primarily crystal-rich intermediates (andesites-dacites), thought to be derived from fractional crystallization of a mantle-derived basalt, magma-mixing and crustal assimilation. UVC lavas are remarkably homogeneous on the hand-sample scale and larger, but petrographic analyses reveal significant microscopic-scale heterogeneities typical of intermediate lavas (e.g. Eichelberger 1978). The following section synthesizes past petrographic and geochemical studies with present petrographic work to produce a narrative of magma generation and evolution at the UVC. Petrographic and geochemical work from this study includes thin section petrography, and estimated zircon saturation temperatures.

4.1 Background: Magma generation and evolution at the UVC

The Unzen Volcanic Complex is characterized by eruptions of crystal-rich lavas within a narrow range of intermediate compositions. Both Older and Younger Unzen deposits are intermediate in composition, ranging from basaltic andesites (rarely) to dacites (Figure 4.1). Both Older and Younger Unzen volcanic rocks contain phenocrysts of plagioclase + hornblende + quartz ± biotite, with ubiquitous Fe-Ti oxides and minor to trace proportions of groundmass pyroxenes ± olivine. Disequilibrium phases and textures are common (Section 4.2), and mafic enclaves (51-59 wt.% silica) typically account for 4-6 vol.% of erupted material (Browne et al., 2006). Generally, Older Unzen volcanic rocks are more mafic, containing more pyroxenes and less hydrous minerals than Younger Unzen volcanic rocks (Sugimoto et al., 2005). Petrographic analyses show evidence for extensive magma mixing between silicic and mafic end members throughout the UVC eruptive period. Four processes are thought to account for the composition of the UVC volcanics: 1) decompression-driven mantle melting (e.g. Hoshizumi et al., 1999), 2) crustal assimilation (Chen et al., 1993; Chen et al., 1999), 3) magma mixing and/or magma mingling (Nishimura et al., 2005; Nakamura 1995; Browne et al., 2006; Sugimoto et al., 2005), and 4) fractional crystallization in a shallow magma chamber (Sugimoto et al., 2005).

Magma generation and crustal assimilation

Magma generation at the UVC is ultimately thought to be driven by back-arc extension leading to decompressional melting of the mantle (e.g. Hoshizumi et al., 1999; Uto et al., 2002). This magma then evolves through fractional crustal assimilation, fractionation crystallization and magma mixing/mingling prior to eruption. Assimilation may play a significant role in UVC magma development, as oxygen and strontium isotopic compositions of Unzen volcanic rocks show broad variations that suggest abundant incorporation of crustal materials (Chen et al., 1993; Chen et al., 1999). The UVC upper-crustal magma may be the product of melted local continental crust mixed with mantle-derived basaltic magma, accompanied by fractional crystallization at shallower depths (Chen et al., 1999; Sugimoto et al., 2005). Chen et al. (1999) estimate that 50-80% of UVC magma is residual mantle magma and 30-70% assimilated crustal material.

Magma mixing and shallow fractional-crystallization

It is thought that magma mixing and/or mingling between a low-temperature silicic endmember and high-temperature mafic endmember occurs in the shallow crust. This process produces mafic enclaves (e.g. Browne et al., 2006; Figure 4.2), as well as the disequilibrium phases and textures seen in thin section (e.g. Sugimoto et al., 2005; Section 4.3). The Unzen volcanic rocks are mainly produced by magma mixing between high-temperature mafic and low-temperature silicic endmembers (e.g. Nishimura et al., 2005; Sugimoto et al., 2005); Browne et al. (2006) argue for a more nuanced process of "mingling" between two endmembers rather than a complete hybridization. The mafic end-member ("recharge" magma) has been suggested to have the chemical characteristics of an ocean-island basalt (Chen et al., 1999). Estimations for the composition of the 1991-1995 eruption's recharge magma include 1) a high-alumina, olivine-bearing basaltic magma (~50 wt.% silica; Browne et al., 2006), 2) an olivine-bearing basaltic andesite resembling the 1663 Furuyake lava (~57 wt.% silica; e.g. Chen et al., 1999), 3) a nearly aphyric pyroxene-bearing andesite (~60 wt.% silica; Holtz et al., 2005). Estimated temperatures for the high-temperature end-member range from 1030-1130˚C (Venezky and Rutherford 1999).

The low-temperature end-member magma of the UVC is thought to be stored in a shallow, upper-crustal magma chamber located between 2-11 km depth (or ~140-250 MPa;

Nishimura et al., 2005; Umakoshi et al., 2001). It's interpreted as a fractionally-crystallized, phenocryst-rich magma derived from the high-T intruding mafic magma (Figure 1.3). Compositional estimates range from ~66 wt.% (Browne et al., 2006) to ~70 wt.% silica (Holtz et al., 2005). Estimated storage temperatures range from 760-800˚C (Holtz et al., 2005; Venezky and Rutherford 1999).

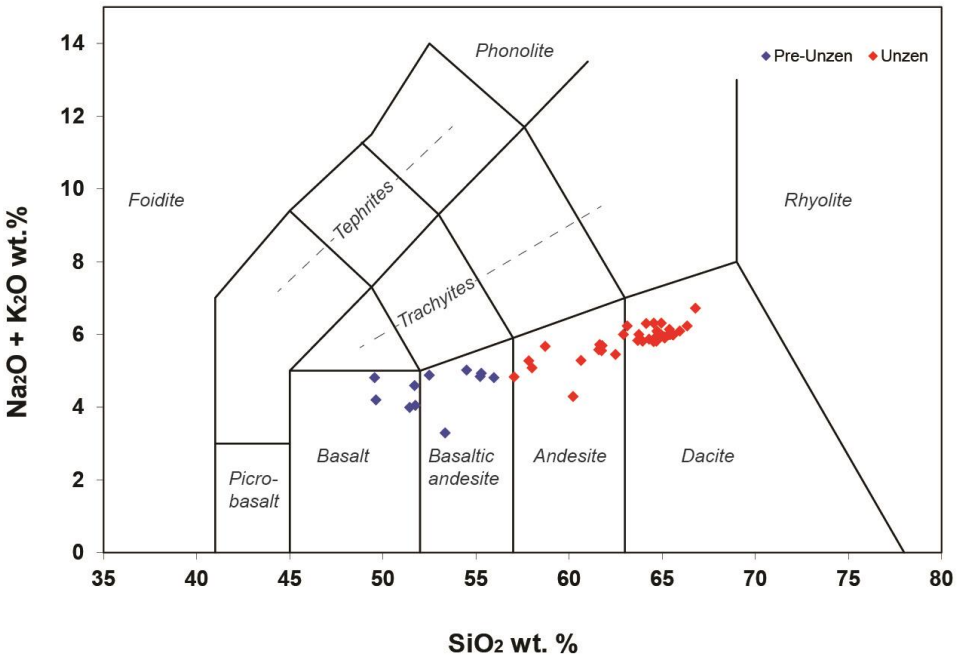

Figure 4.1 Classification of Pre-Unzen (> 500 ka) and Unzen volcanic rocks. Unzen volcanic rocks are primarily andesites to dacites. (Figure by author; data acquired on GEOROC from Nakada & Motomura, 1999; Miyoshi et al., 2008; Sugimoto et al., 2005; and, Browne et al., 2006)

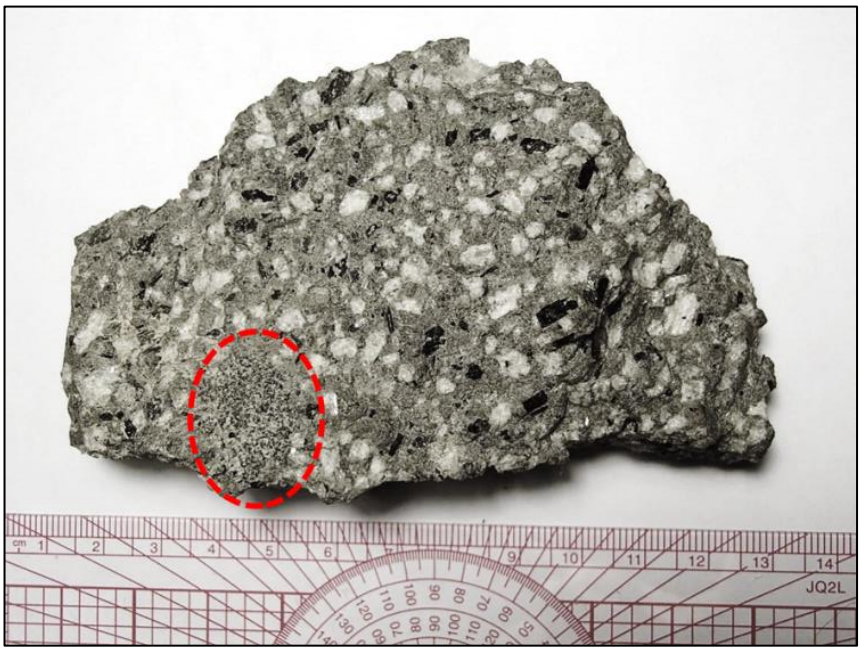

Figure 4.2 Crystal-rich lava erupted at Unzen Volcanic Complex in 1995. Note the fine-grained mafic enclave circled in red. (Sample: UNZ14032, "Heisei-shinzan"; photo by author)

4.2 Thin section petrography

Polished thin sections were prepared for each sample to use for petrographic analysis. Phase volume percentages were estimated with petrographic microscope (Table 4.1). Micrographs of each thin section were taken in transmitted and cross-polarized light. This section summarizes the range of petrographic characteristics observed in the UVC samples. Overall, the UVC lavas sampled are petrographically similar: crystal-rich intermediate lavas with phenocryst of plagioclase >> hornblende ≈ biotite > quartz showing substantial disequilibrium textures. Full thin section descriptions are included in the Appendix B.

Summary

All of the samples share similar phenocryst phases, crystal contents, and textures. Average phenocryst content is high in all samples, averaging ~42 vol.%. The general phenocryst phase assemblage of all the samples can approximated as plagioclase >> hornblende ≈ biotite > quartz (Table 4.1). Phenocrysts of plagioclase and hornblende can extend to over 1 cm in length in samples containing more silicic phase assemblages. Plagioclase ranges from 15-24 vol.%, followed by hornblende at 7-11 vol.%, biotite at 5-10 vol.%, and quartz ranging from trace amounts to 10 vol.%. Accessory, groundmass phases include ubiquitous Fe-Ti oxides (1-5%), pyroxenes (trace to 5%), zircon (trace), and rarely olivine (trace). Coarse-grained mafic enclaves (plagioclase > hornblende) are found in all collected samples, typically representing 1-5% by volume.

Phenocryst contents range from 38-45 vol.%. Plagioclase phenocrysts typically show a continuous range in size from groundmass up to 15 mm; multiple populations are often identifiable, typically split between 1) euhedral, normal oscillatory-zoned grains, 2) dusty-edged, mineral/melt inclusion-rich grains, 3) mottled core grains, and 4) rounded grains of variable textures. Hornblende phenocrysts are typically 2-10 mm, and are also present as a groundmass phase; grains are typically euhedral and occasionally have a fine-grained reaction rim or opaque rim. Biotite phenocrysts range from groundmass up to 5 mm and often have a fine-grained reaction or decompression rims; vapor-phase biotite is found rarely. Quartz phenocrysts range in size from 0.5-5mm and are ubiquitously rounded, embayed and broken in all samples without variation. Rarely, quartz phenocrysts are

surrounded by fine-grained rims of pyroxenes. Glomerocrysts of plagioclase ± hornblende ± biotite are commonly observed.

Groundmasses of all samples contain abundant microlites. Groundmasses are typically devitrified and poorly vesicular (less than 10% by volume). Microlite phases include plagioclase, hornblende, Fe-Ti oxides, biotite, less commonly pyroxenes, and rarely olivine. In two samples (UNZ14029 and UNZ14008), rare small (<1.5 mm) clots of pyroxenes ± olivine are observed, sometimes touching hornblende phenocrysts. The microlite content increases the crystallinity of the lavas beyond the phenocryst volume percent, making the crystallinity of Unzen dome lavas between 50-60 vol.%. Zircon occurs as a trace phase, most commonly found in contact with or as an inclusion in biotite and hornblende; groundmass zircon could not be identified in thin section.

While mafic enclaves were observed in hand-samples of all samples, mafic enclaves were sectioned in only two thin sections: the most recent eruption 1990-1995 (Heisei-shinzan; UNZ13001), and the 1792 Tenguyama debris avalanche (UNZ13002; Figure 4.3 and 4.4). Crystallinities of mafic enclaves are high, between 70-80 vol.%. The phase assemblage is plagioclase at 40-50%, followed by hornblende at 30-40%. Both enclaves are fine-grained (less than 0.5 mm), and crystals are typically euhedral to subhedral. The contact with the host lava is sharp, with no apparent reactive zone.

Petrographic evidence reveals microscopic heterogeneities and disequilibrium assemblages within lavas of the UVC. Multiple populations of plagioclase crystals, with textures suggesting disparate crystallization histories, are well-mixed; hornblende and biotite phenocrysts are opacitized to varying degrees; some hornblende and biotite crystals have reaction rims while neighboring ones do not; quartz and olivine are found together; glomerocrysts of plagioclase, pyroxenes, hydrous minerals and oxides (rarely with olivine) are ubiquitous; rounded quartz phenocrysts occasionally have pyroxene rims; groundmass olivine is often observed in domes and flows, but is low in abundance. Petrographic evidence supports the hypothesis of a mafic end-member mingling with a silicic-endmember, as suggested by numerous researchers (e.g. Sugimoto et al., 2005; Nishimura et al., 2005; Holtz et al., 2005; Browne et al., 2006). Samples collected for this study are typical of UVC lavas, as reported by previously published petrographic studies (e.g. Hoshizumi et al., 1999; Sugimoto et al., 2005).

Sample (Sample ID)	**Iwagamiyama**	**Minami-senbongi**	**Fugen-dake**	**Nodake**	**Taruki-higashi**	**Botanyama**	**Tenguyama**	**Heisei-shinzan**
Sample ID	UNZ14017	UNZ14008	UNZ14033	UNZ14029	UNZ14016	UNZ14013	UNZ14023	UNZ14032
% Glass/Matrix	**55**	**60**	**58**	**62**	**58**	**60**	**55**	**56**
% Phenocrysts	**45**	**40**	**42**	**38**	**42**	**40**	**45**	**44**
Plagioclase	**24**	**20**	**23**	**15 (r)**	**20**	**20 (r)**	**15**	**20**
Hornblende	**7**	**10 (r)**	**7**	**8 (r)**	**7**	**9**	**10**	**11**
Biotite	**7 (r)**	**5 (r)**	**7**	**7 (r)**	**10**	**6 (r)**	**7**	**5**
Quartz	**3 (r)**	**T (r)**	**T (r)**	**T (r)**	**T (r)**	**2 (r)**	**10 (r)**	**7 (r)**
Pyroxenes	**1**	**3**	**3**	**6**		**T**		
Orthopyroxene	*1*	*T*	*1*	*2*	-	*T*	-	-
Clinopyroxene	*T*	*3*	*2*	*4*	-	*T*	-	-
Olivine	**(?)**	**(?)**	**-**	**T**	**-**	**-**	**-**	**-**
Fe-Ti oxides	**3**	**2**	**2**	**1**	**5**	**3**	**3**	**1**
zircon	**T**	**T**	**T**	**T**	**T**	**T**	**T**	**T**

Table 4.1 Summary of thin section petrography for domes analyzed for zircon geochronology. Percentages are based on visually estimated volumes. Orthopyroxene and clinopyroxene abundances are shown in italics as the small grain-sizes of pyroxenes hinder the accurate assessment of modal proportions.
(r) phase where the majority of grains show resorption textures or reaction rims
(?) presence of olivine is uncertain due to minute grain-sizes that may lead to the misidentification of pyroxenes

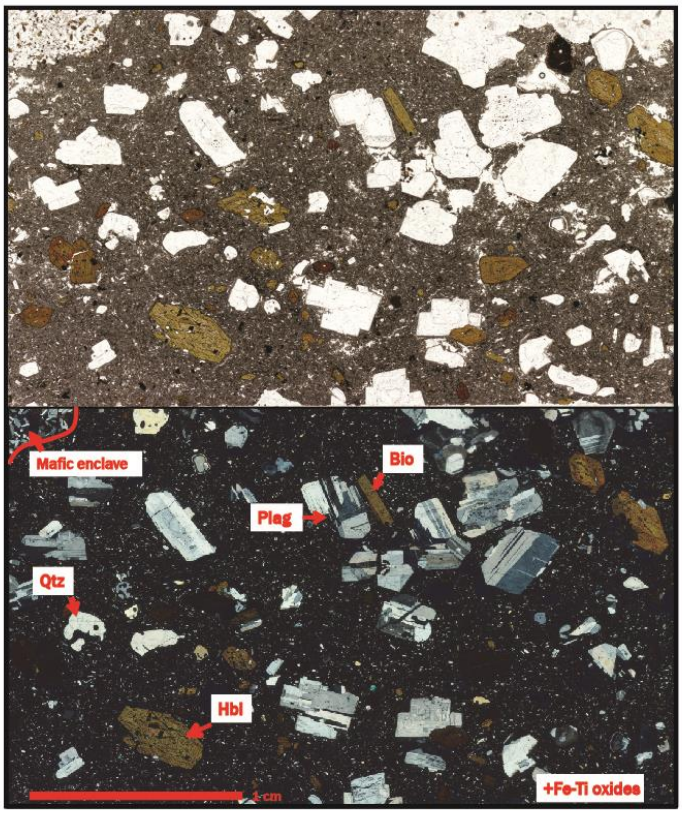

Figure 4.3 Plain polarized and cross-polarized images of thin section from the most recent eruption, Heisei-shinzan. Note the mafic enclave in the upper-left corner (UNZ13001; thin section ID "Unzen_16").

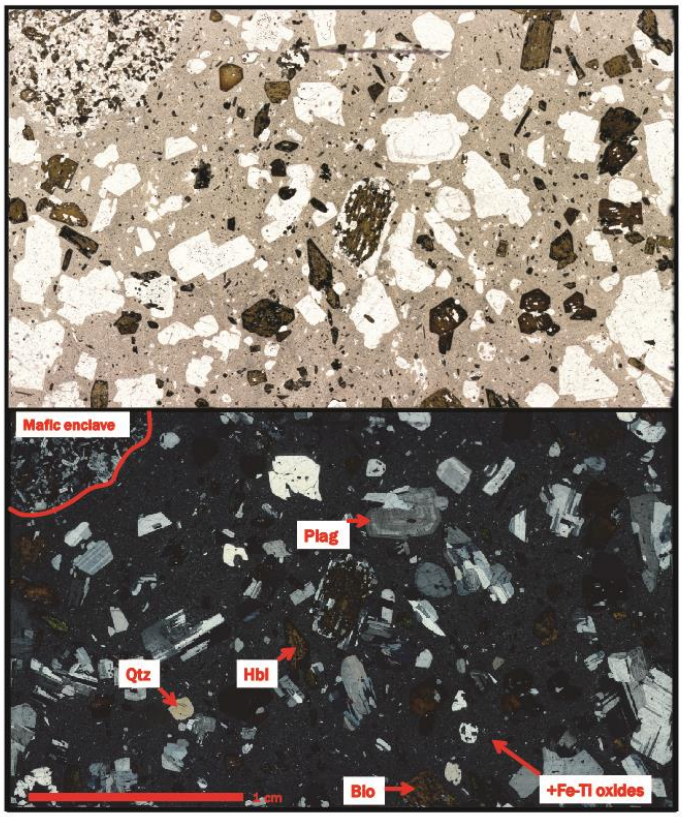

Figure 4.4 Plain polarized and cross-polarized images of thin section from 1792 Mayuyama debris avalanche. Note the mafic enclave in the upper-left corner (UNZ13002; thin section ID "Matuyama_17").

4.3 Zircon saturation thermometry

The zircon saturation temperature (T_{Zr}) of a melt determines the temperature at which zircon can begin to crystallize. Zircon crystallization can only occur when a melt is saturated in zirconium. The temperature when saturation is reached depends on the composition of the melt, specifically the cation ratio *M* ([Na+K+2*Ca]/[Al*Si]) (Hanchar and Watson, 2003). Temperatures above zircon saturation lead to the eventual dissolution of zircon, within the order of 10s to 1000s of years in wet systems (>2 wt.% H_2O) depending on temperature, crystal size and water content of the melt (Harrison and Watson 1983).

Zircon saturation temperatures were calculated for the UVC using the method described in Hanchar and Watson (2003) and published data from samples erupted in 1991-1995: groundmass glass (Nakada and Motomura 1999), and quartz- & plagioclase-hosted melt inclusions (Nishimura et al., 2005). The range of melt compositions over which zircon crystallizes at the UVC, and other intermediate systems, cannot be directly determined as erupted samples represent a magma mixture (i.e. of mafic and silicic endmembers), which does not likely reflect the upper-crustal melt composition where zircon crystallizes. For this reason, whole rock data was not used for these calculations, because 1) it may not be representative of the melt from which zircon crystallized, and 2) cation ratios (*M*) calculated from published bulk whole rock data of the UVC were between *M*≈2.2-3.2, which is outside the calibration range of Watson and Harrison (1983). For this reason, groundmass glass and melt inclusion data were chosen for zircon saturation temperature calculations. While these values are interpreted to resemble the upper-crustal silicic melt from which zircon crystallized, it should be noted that matrix glass is residual melt that may not reflect the composition of melt from which zircon crystallized.

The melt inclusion and glass dataset ranges in composition from 72.8-79.0 wt.% silica. Calculated cation ratios values range from *M*=1.18-1.52, which is well within the calibration range (*M* = 0.9-2.0) of Watson and Harrison (1983). Neither sets of published data included zirconium concentrations, so a fixed value of 143 ppm was assigned to all samples. This value was the measured concentration of zirconium in a groundmass separate (68 wt.% silica) from the same eruption as the dataset used here for T_{Zr} calculations (1990-1995 eruption; Nakada and Motomura 1999), and this concentration is intermediary for the

system (whole rock Zr contents range from 90-180 ppm, as shown in Figure 2.2). Changes in temperature resulting from variable Zr contents can be explored by assigning a representative cation ion ratio (*M*) for the UVC, based on average *M* value for the system (M=1.29; Figure 4.5).

Calculated zircon saturation temperatures at the Unzen Volcanic Complex range from ~768-792˚C (Table 4.2), with an average saturation temperature of ~784 ˚C. Because zirconium contents of published melt inclusion and groundmass samples were not available, an estimated range of concentrations necessary to saturate a melt of the average composition of the samples (*M*=1.29) at a particular temperature was estimated: at a concentration of 50 ppm Zr, T_{Zr}=700˚C; increasing the Zr concentration to 300 ppm raises T_{Zr} to ~850˚C (Figure 4.5). Estimated T_{Zr} temperatures overlap with estimated temperatures of the low-temperature silicic endmember magma at the UVC from published works (760-800˚C; Holtz et al., 2005; Venezky and Rutherford 1999).

Sample ID	Source	Phase	Silica (wt.%)	Cation Ration (*M*)	Zr Saturation T (˚C)
91-4pumice (Ash)	Nakada and Motomura 1999	groundmass glass	74.4	1.37	778
910916c (Ib-3)	Nakada and Motomura 1999	groundmass glass	75.8	1.18	792
92010801 (Ib-4)	Nakada and Motomura 1999	groundmass glass	78.0	1.29	784
92081301 (Ib-7)	Nakada and Motomura 1999	groundmass glass	78.7	1.32	782
93040102 (Ib-10)	Nakada and Motomura 1999	groundmass glass	78.4	1.22	789
94020405 (Ib-12)	Nakada and Motomura 1999	groundmass glass	79.0	1.27	786
94082101 (Ib-13)	Nakada and Motomura 1999	groundmass glass	78.5	1.28	785
Bomb-01	Nishimura et al., 2005	qtz-hosted melt inclusion	74.6	1.24	788
Bomb-02	Nishimura et al., 2005	qtz-hosted melt inclusion	75.7	1.24	788
Bomb-03-1	Nishimura et al., 2005	qtz-hosted melt inclusion	73.6	1.33	781
Bomb-03-2	Nishimura et al., 2005	qtz-hosted melt inclusion	74.5	1.25	787
Bomb-03-3	Nishimura et al., 2005	qtz-hosted melt inclusion	75	1.35	780
VB-01	Nishimura et al., 2005	qtz-hosted melt inclusion	75.1	1.27	786
VB-02	Nishimura et al., 2005	qtz-hosted melt inclusion	74.9	1.26	786
VB-03	Nishimura et al., 2005	qtz-hosted melt inclusion	76.2	1.19	791
Bomb-04-1	Nishimura et al., 2005	plag-hosted melt inclusion	73.5	1.52	768
Bomb-04-2	Nishimura et al., 2005	plag-hosted melt inclusion	72.8	1.35	780
Bomb-05-1	Nishimura et al., 2005	plag-hosted melt inclusion	73	1.25	787
Bomb-05-2	Nishimura et al., 2005	plag-hosted melt inclusion	73.2	1.34	780
Average			*75.5*	*1.29*	*784*

Table 4.2 Estimate zircon saturation temperatures calculated from published melt inclusion and groundmass glass data from the 1990-1995 eruption. No zirconium measurements were included with the data, so a value of 143 ppm was assigned in all calculations.

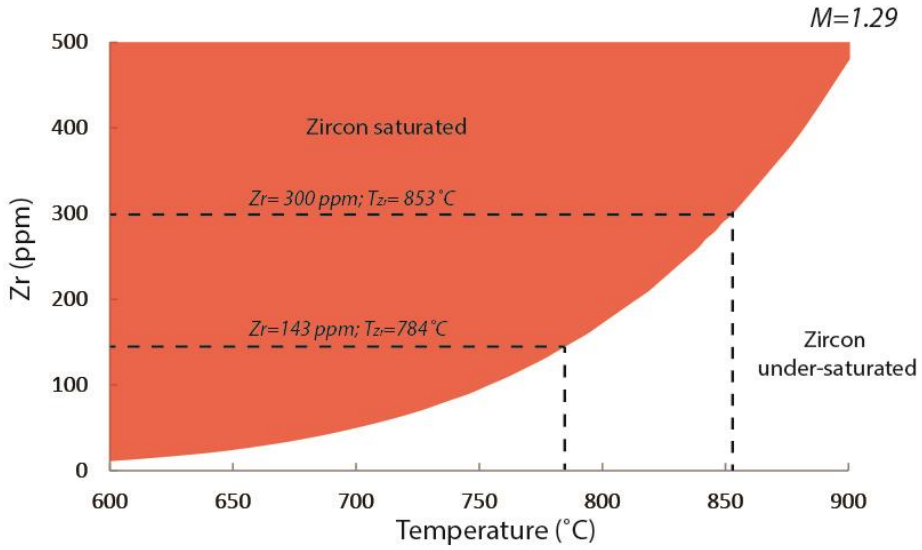

Figure 4.5 Illustration of the range of zirconium concentrations and temperatures over which a melt of *M*=1.29 is zircon saturated.

5 Zircon chronochemistry

Zircon chronochemistry was completed on selected lavas from the Unzen Volcanic Complex, using both secondary ion mass spectrometry (SIMS) and laser ablation inductively coupled mass spectrometry (LA-ICPMS). General zircon chemistry of the UVC was investigated using LA-ICPMS on twelve samples, ranging in eruption age from the most recent eruption to the 260±20 ka Sarubayama eruption (K/Ar; Hoshizumi et al., 1999). Paired surface-interior of individual crystals were analyzed for trace element chemistry, which – coupled with sample eruption ages – allowed a relative age relationship to be established. Zircon surfaces and interiors from 8 of the 12 samples were directly dated with U/Th geochronology using SIMS, and, additionally, limited trace element chemistry from 6 of these samples was measured simultaneously using the SHRIMP-RG. Together, zircon chronochemistry from lavas of the Unzen Volcanic Complex was used to determine the conditions of upper-crustal magma storage, and its evolution through time.

5.1 Zircon crystal morphologies

Mineral separation of 12 crystal-rich andesitic to dacitic lavas yielded a fair amount of zircon crystals from each, ranging in size from ~50-200+ microns. Zircon crystal morphologies varied within samples, although differences between samples were limited largely to crystal size variations. Tenguyama (UNZ13002) and Heisei-shinzan (UNZ13001) produced the largest crystals on average (~175+ μm), while Fugen-dake produced the smallest (~ 90 μm). Each eruption sample produced a variety of crystal morphologies, common between each other (Figure 5.1). Unpolished crystal surfaces ranged from euhedral, doubly-terminated crystals with a variety of aspect ratios to crystals with rounded edges; broken crystals were common, but this likely occurred during sample preparation (Figure 5.1 and 5.2).

Cathodoluminescence (CL) images revealed additional variations in zircon crystals through interior zonation patterns (Figure 5.2): 1) symmetric, euhedral concentrically-zoned crystals, 2) symmetric, concentrically-zoned crystals showing changes in crystal morphology from interior to rim (occasionally separated by rounded zones), 3) concentrically-zoned crystals with rounded zonation (or a mixture of rounded and euhedral

zones), and 4) asymmetric zonation with warped and/or mottled zones (typically interior-most zone). Crystals with rounded or mottles zones suggest past dissolution or growth disturbances (e.g. Hoskins and Schaltegger 2003). No interior morphologies strongly suggested the presence of xenocrystic cores (i.e. rounded with shape discordant with surrounding growth patterns). While all samples contained a mixture of zircon morphologies, euhedral crystals showing normal oscillatory zonation and few rounded zones were most common.

Figure 5.1 Transmitted light image of UVC zircon before picking, showing a range of sizes and morphologies within the same sample (crystals from Botanyama; UNZ14013).

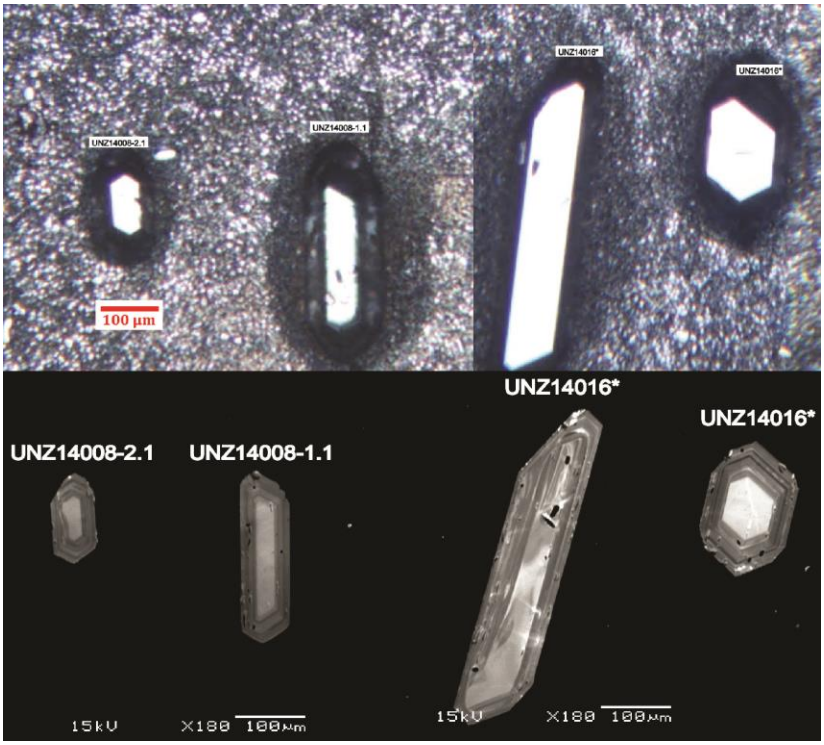

Figure 5.2 Image of UVC zircon crystals analyzed at the SHRIMP-RG before and after polishing. Top photo: transmitted light image of unpolished crystals mounted in indium for surface analysis. Bottom photo: cathodoluminescence (CL) image of same crystals after polishing to reveal interiors; pot marks are likely areas where inclusions were plucked out during polishing. Note the interior zones of the crystals: UNZ14008-1 and UNZ14016*2 show typical concentric zonation, while UNZ14008-2.1 and UNZ14016*1 show asymmetric zonation with a mottled texture suggesting past dissolution.

5.2 Zircon chemistry (LA-ICMPS results)

Trace element chemistry of zircon crystals using LA-ICPMS reveals that there is no systematic variation between crystal surfaces and interiors, or between eruption samples, in rare earth (REE) profiles and most measured trace element concentrations. Yttrium (Y) concentrations range from 200~1800 ppm, with an average concentration for surfaces of 616 ppm (±248 ppm for 1σ), and for interiors of 641 ppm (±210 ppm/1σ). It should be noted that Y contents may strongly be influenced by zonation, as cps often steadily increased or decreased during analysis. Niobium (Nb) concentrations range from 2~10 ppm, with surfaces yielding an average of 4.0 ppm (±2.3 ppm/1σ), and interiors, 4.9 (±2.0 ppm/1σ). Both Y and Nb concentrations for surfaces and interiors overlap, showing no systematic variation. However, Y and Nb show coupled behavior: as Y increases, so does Nb with moderate correlation coefficients of $r_{Pearson}$=0.50 and $r_{Spearman}$=0.54 (Figure 5.3). Elevated Y and Nb concentrations may be due to hitting inclusions during analysis (e.g. Jain et al., 2001). Elevated Y contents also tend to occur with increasing phosphorus content, which may simply reflect xenotime substitution ([$(Y,REE)^{3+} + P^{5+} = Zr^{4+} + Si^{4+}$]; Speer 1982); Nb has a similar coupled-substitution mechanism in zircon (e.g. Hoskins and Schaltegger 2003). There are no apparent variations between surface and interior analyses, or between eruption samples, for Y, Nb and P.

Additionally, no systematic variation is observed in chondrite-normalized rare earth element profiles (Figure 5.4). REE spider diagrams were normalized using C1-chondrite values from McDonough and Sun (1995). Surface and interior analyses overlap, and mean REE profiles for each are virtually indistinguishable (Figure 5.4). Relative to chondrite values, UVC zircon are heavy-rare earth (HREE) enriched and light-rare earth (LREE) depleted. Increased variability in LREE between samples is likely due to the influence of inclusions (e.g. Jain et al., 2001; Sano et al., 2002). Lanthanum (La) concentrations were below detection limits for the calibration standard, MADER, and are, therefore, not reported in the REE profiles for the UVC. The REE profile of UVC zircons shows a pronounced, positive cerium (Ce) anomaly and a negative europium (Eu) anomaly.

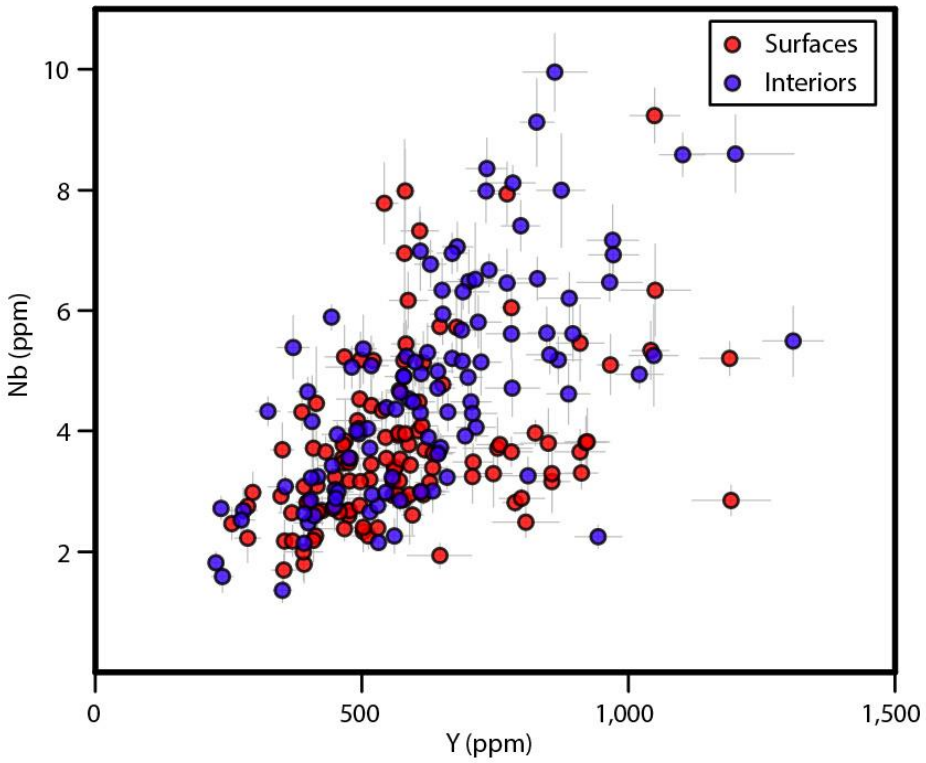

Figure 5.3 Niobium vs. yttrium concentrations for zircon surfaces and interiors, showing similar behavior that may reflect inclusion influence or coupled substitution mechanisms. Correlation coefficients: $r_{Pearson} = 0.50$; $r_{Spearman} = 0.50$.

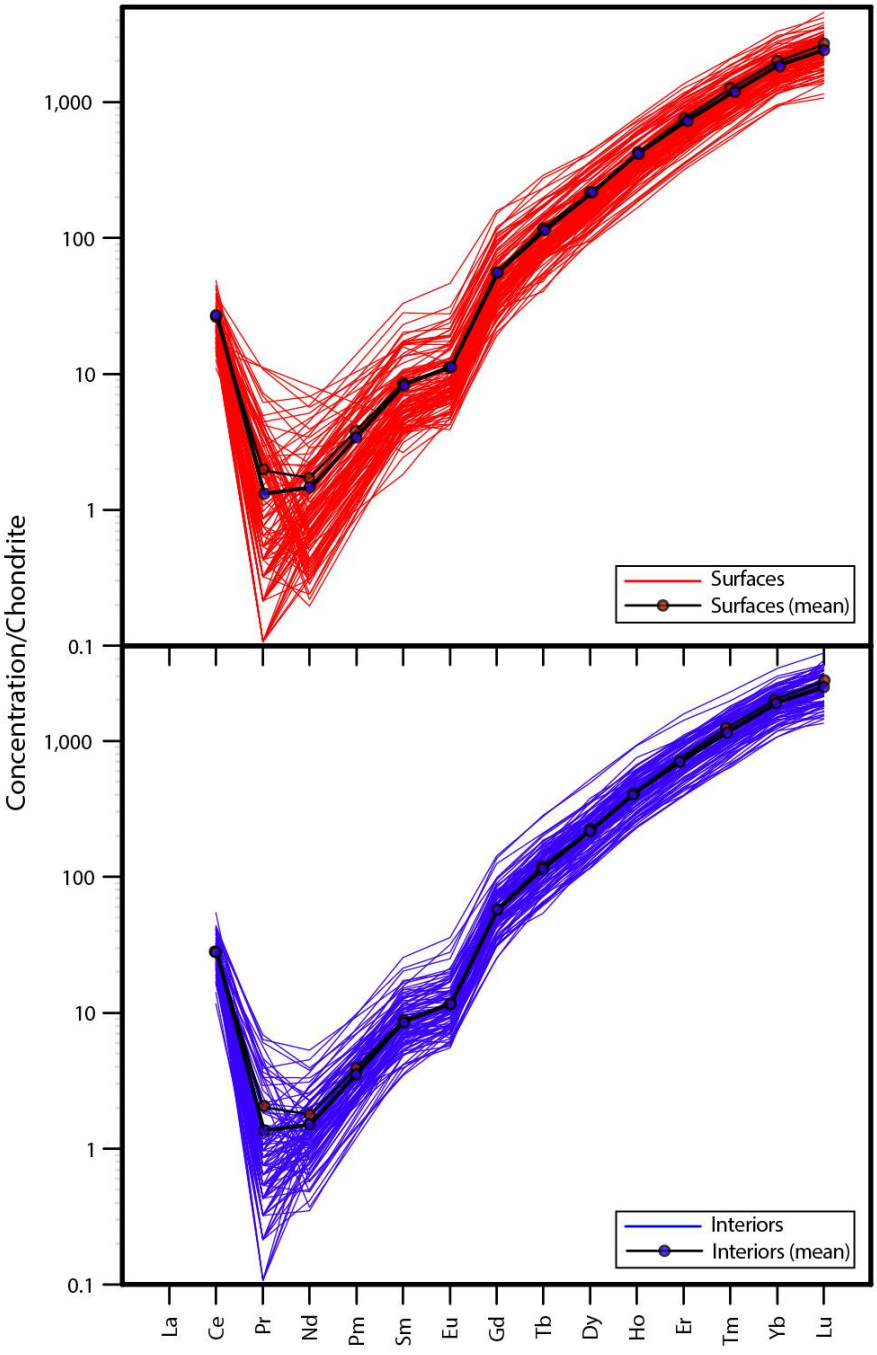

Figure 5.4 C1-chondrite-normalized REE profile showing mean surface and interior values (red and blue lines, respectively). C1-chondrite values from McDonough and Sun 1995. Mean surface and interior lines are shown on both profiles.

While the majority of trace element concentrations from LA-ICPMS analyses do not show systematic variation from interior to surface, subtle variations can be observed in hafnium (Hf). Hafnium surface concentrations average 9881 ppm (±1106 ppm/1σ) with a range of 7500~12400 ppm, while interiors average 8182 ppm (±1388 ppm/1σ) with a range of 4800~11800 ppm (Figure 5.5).

Little variability is observed in Th/U and Eu/Eu* ratios between surface and interior. Th/U ratios show considerable overlap between surfaces and interiors, although interiors are on average lower. Surface Th/U ratios average 0.61 (±0.15/1σ) with range of 0.3~1.0, while interiors average 0.70 (±0.23/1σ), with range of 0.3~1.5. Ratios of Th/U >1.0 are absent in surfaces, but account for approximately 10% of interiors. Th/U ratio appears to increase with increasing Hf content in interiors, but no correlation is observed in surface analyses (Figure 5.5). The range of europium anomaly (Eu/Eu*) values for both surfaces and interiors is nearly identical: ~0.30-0.90 for surfaces (0.52 on average ±0.10/1σ), and 0.32~0.84 for interiors (0.53 on average ±0.09/1σ). There is weak to no correlation (<|0.2|) observed between Hf and Th/U or Eu/Eu* (Figure 5.5; Appendix C).

However, a sample-by-sample comparison of Hf contents, Th/U ratios and Eu/Eu* reveal subtle distinctions between Older and Younger Unzen eruption samples (Figure 5.5). Samples erupted during the Older Unzen period (500 – 200 ka) typically show a restricted range in Th/U ratios (<0.8); Eu/Eu* values are all less than 0.7. Samples erupted in the Younger Unzen period (100 ka – present) show considerably more variation in Th/U, and Eu/Eu* values compared to Older Unzen, covering the entire range of measured values (Figure 5.5). Th/U ratios range from 0.3~1.48; Eu/Eu* values range from 0.3~0.9. The most recently erupted sample, Heisei-shinzan (1991-1995), shows the most variability in Hf, Th/U and Eu/Eu*, covering essentially the entire range of measured values for each element or ratio.

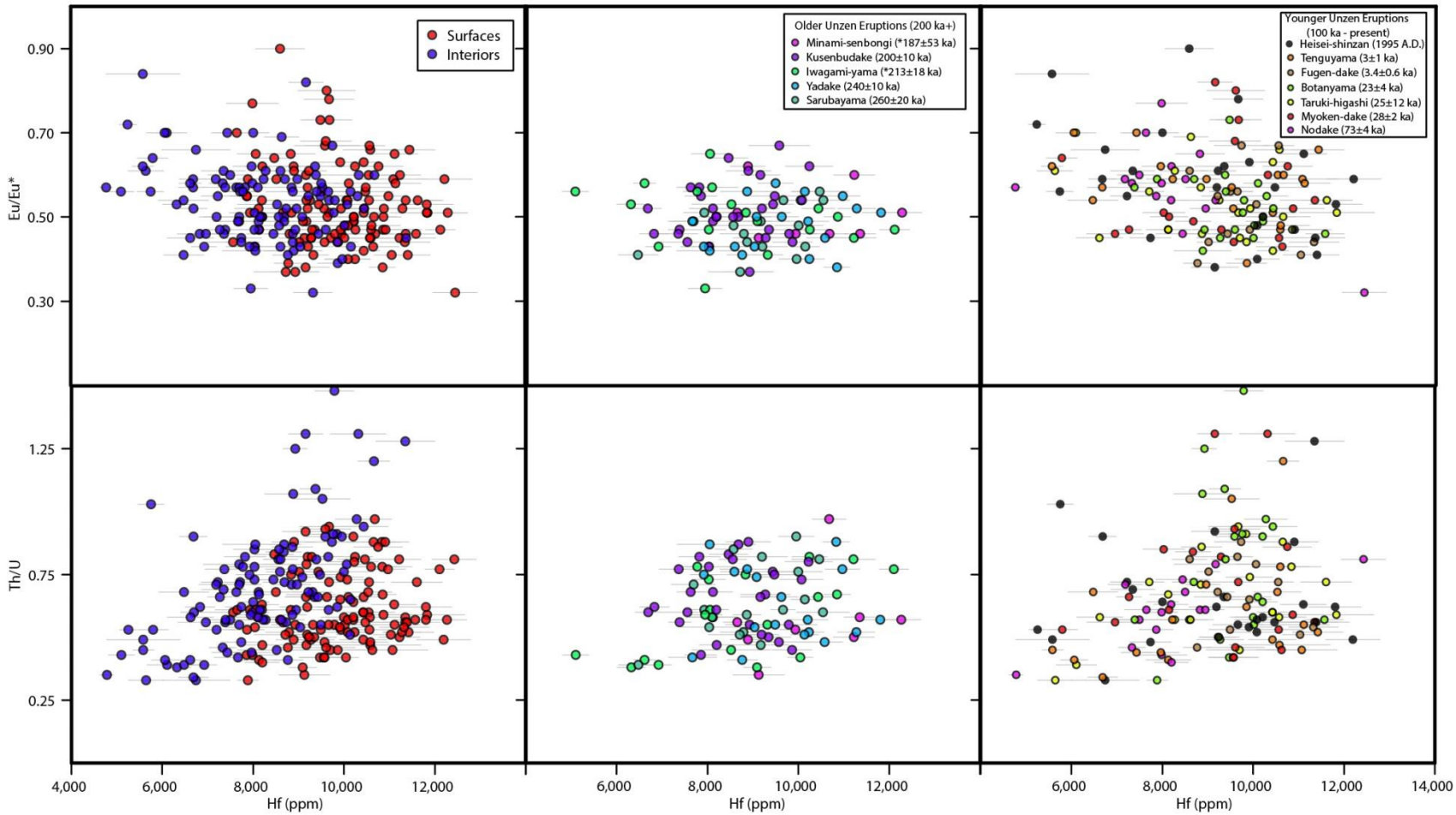

Figure 5.5 Th/U ratios and europium anomalies vs. hafnium concentrations for surfaces and interiors (left), and sample-specific (center and right). Range in Th/U ratios and europium anomalies vs. hafnium concentrations for Older Unzen eruption samples (center), and Younger Unzen eruption samples (right). Older Unzen samples with asterisk (*) indicate that U/Th zircon dating revealed crystals significantly younger than reported K/Ar and Ar/Ar data, indicating that they may be products of the Younger Unzen period.

5.3 Age relationships

5.3.1 Zircon age spectra (SIMS age results)

A total of 185 U/Th spot measurements were collected using SIMS: 28 spots from preliminary samples (UNZ13001 and UNZ13002) on the Cameca 1270, and 157 spots from the SHRIMP-RG. Of the spots measured, a total of 70 unpolished surfaces and 115 polished interiors were collected. Sample analyses range from within-error of present to secular equilibrium (Figure 5.6). Given the number of samples and associated errors, the data is most easily viewed as rank order plots on a dome by dome basis (Figure 5.7). A minority of zircon ages fell on or over the equiline (≥350 ka), with a total of 10 spots producing ages either over the equiline (5 spots) or with positive errors over the equiline (5 spots), representing 5% of analyzed spots. All spots at secular equilibrium were interior analyses. Spots measured over the equiline were not included in probability density function (PDF) plots. Model age errors are reported at 1σ. Probability density function charts were produced in Excel 2010 using the PC-version of Isoplot 4.1 (Ken Ludwig 2009; 2012). Zircon age populations were determined using the Isoplot's Gaussian deconvolution tool, which using the Sambridge-Compston approach, with negative 1σ age errors used in the calculations.

Individual crystals show a significant range in age between surface and interior. Crystal ages range from zero (surface and interior ages within error) to >200 ka (Figure 5.7). Surface model ages are younger on average, but range from ~1 ka – 24 ka. Interior model ages range from ~28 ka – secular equilibrium (>350 ka); the samples containing the most crystals with interiors at secular equilibrium are Minami-senbongi (N=3), followed by Nodake (N=1) and Fugen-dake (N=1). All eruption samples contain crystals with surface-interior pairs that extend from the Younger period into the eruptive hiatus (200-100 ka), and the majority of samples contain at least one zircon crystal with a surface-interior age pair that bridges the gap between the Older (500-200 ka) and Younger (100 ka-present) periods. Most samples also contain older crystals with surface-interior pairs that extend from the eruptive hiatus into the Older period. When zircon crystals from all samples are compiled (surface and interior ages), they reveal a relatively continuous range of model ages from 1 ka through at least 200 ka, when considering increasingly large errors towards

older ages, and possibly through secular equilibrium (~350 ka). While the majority of model ages predate eruption sample eruption ages, at least four samples contain 1~2 model ages within error of eruption age. Two eruption samples produced crystals younger than previously published K/Ar and/or Ar/Ar ages: Minami-senbongi and Iwagamiyama.

Individual age spectra for each eruption sample (Figure 5.8) reveal that all samples contain a range of zircon surfaces and interiors that significantly pre-date eruption (≥100 ka). At least half of the samples contain models ages that are within-error of eruption. The two most recent eruptions (Heisei-shinzan and Tenguyama), however, have no samples within error of eruption, with the closet model ages to eruption predating it by ~15-20 ka; two samples (Minami-senbongi and Iwagamiyama) produced zircon model ages significantly younger (50~100 ka) than available K/Ar and/or Ar/Ar dates, suggesting these measurements do not accurately reflect eruption ages, so it is not possible to determine if eruption-age zircon are present. Probability density function (PDF) plots for each sample reveal a diverse range of peaks, suggesting that zircon growth may be punctuated through time. All Younger Unzen eruption samples contain peaks occurring during the Younger period (100 ka-present), and most samples also have secondary peaks occurring during the eruptive hiatus (200-100 ka); there may be tertiary peaks during the Older period (>200 ka), but – given large errors on samples near the equiline – it is not possible to confirm. Compiled PDF curves for surfaces and interiors from all samples (Figure 5.8) show that the most significant peaks during the Younger Unzen and eruptive hiatus periods.

As a group, surface and interior model ages produce several overlapping age populations (Figure 5.9). Surfaces have unmixing population at approximately 20±3 ka, 52±6 ka, 93±11 ka, and 171±23 ka; interiors produce unmixing populations at 35±5 ka, 71±5 ka, 130±11 ka, and 196±23 ka. Surface and interior analyses reveal distinct age populations, with surface and interior age populations occurring successively, typically separated by at least 10~15 ka (Figure 5.9). Older age populations (>100 ka) between surfaces and interiors overlap with-in error to a small extent. Age populations for both surfaces and interiors occur primarily within the Younger Unzen and eruptive hiatus periods, with a single population within error of the late Older Unzen period. A small percentage of interior spots (<5%) are at secular equilibrium and are not included in PDF or

unmixing population calculations. It should be noted that the relative misfit for the Gaussian unmixing populations is large (0.57 for surfaces; 0.61 for interiors), suggesting these age populations may not accurately reflect the diversity of age populations within the UVC.

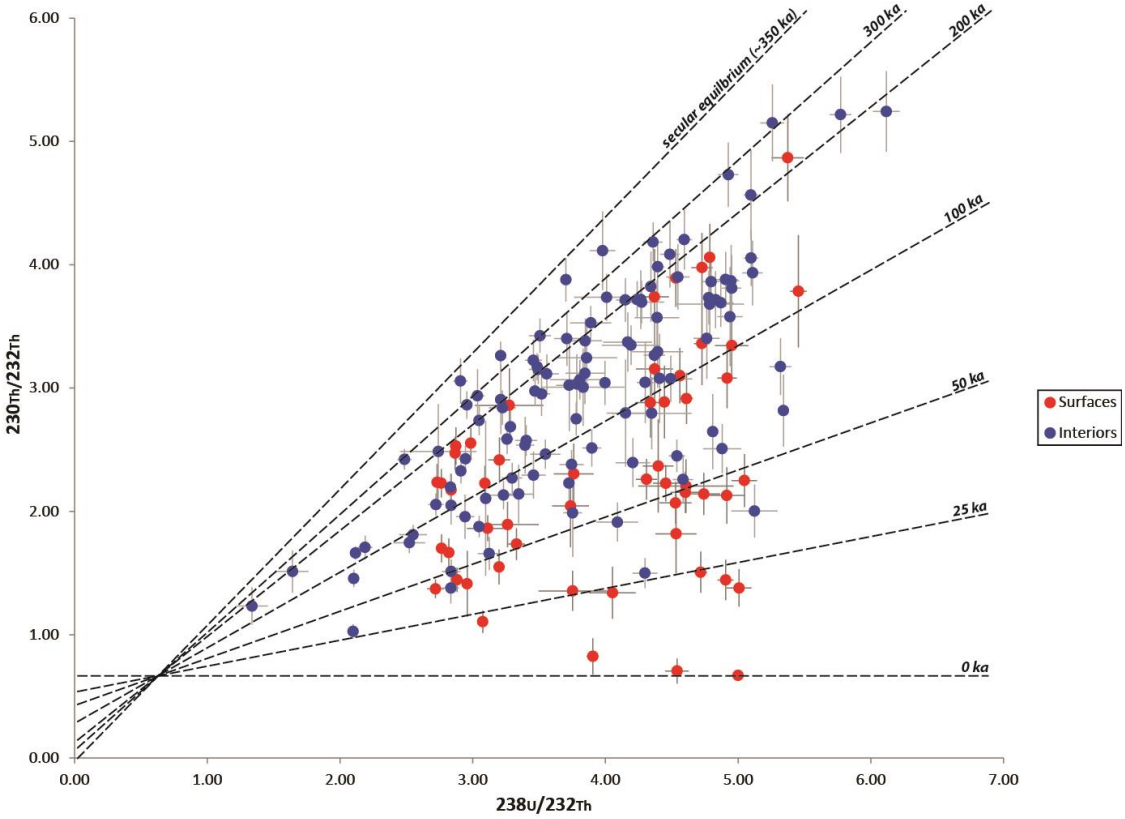

Figure 5.6 $^{238}U/^{230}Th$ isochron diagram showing interior (blue) and surface (red) analyses from all eruptive samples analyzed using SHRIMP-RG. Error bars are 1σ, with reference isochrons. Initial host rock isotopic ratios are $^{238}U/^{232}Th$=0.62 and $^{230}Th/^{232}Th$=0.67.

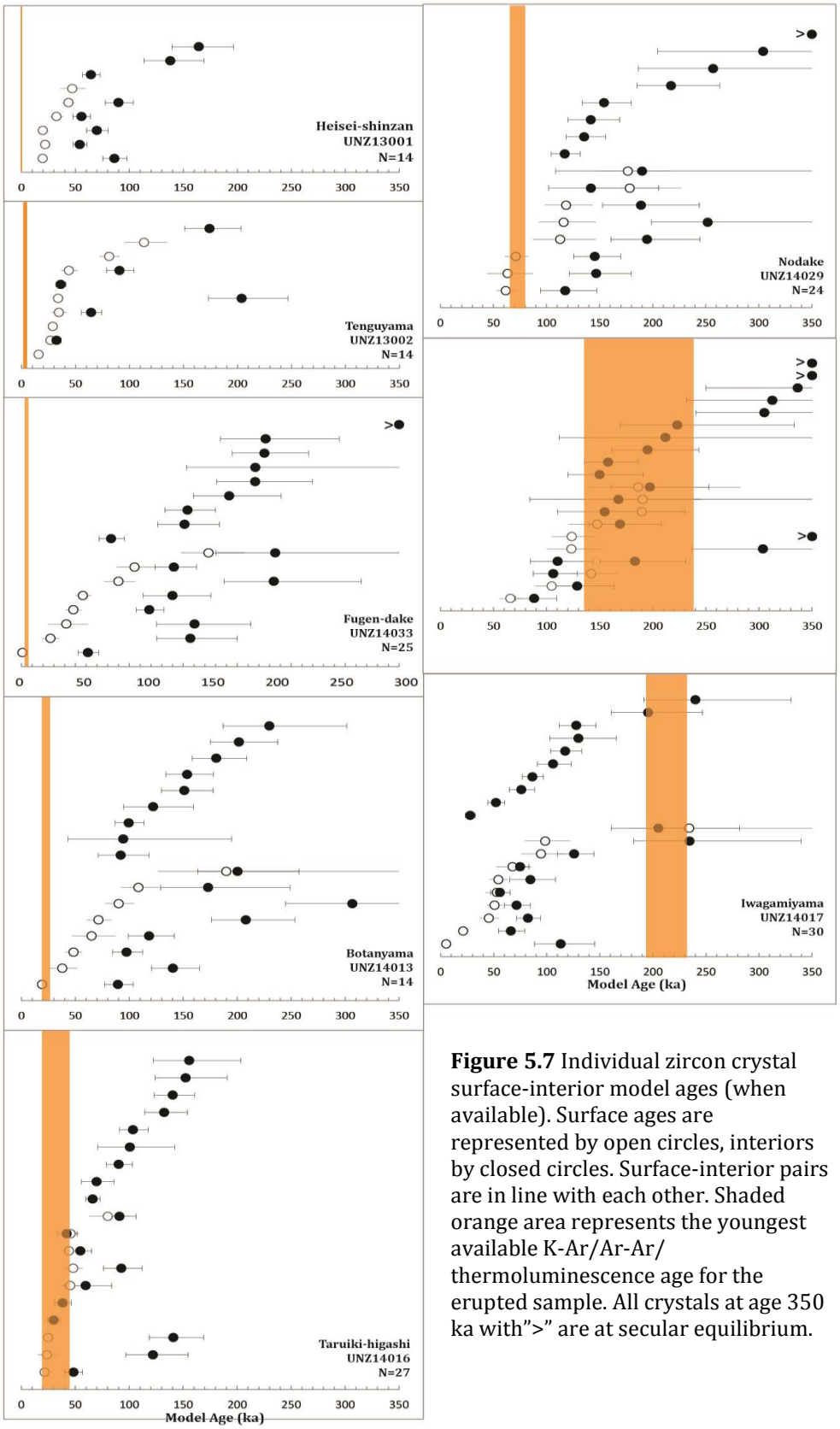

Figure 5.7 Individual zircon crystal surface-interior model ages (when available). Surface ages are represented by open circles, interiors by closed circles. Surface-interior pairs are in line with each other. Shaded orange area represents the youngest available K-Ar/Ar-Ar/ thermoluminescence age for the erupted sample. All crystals at age 350 ka with">" are at secular equilibrium.

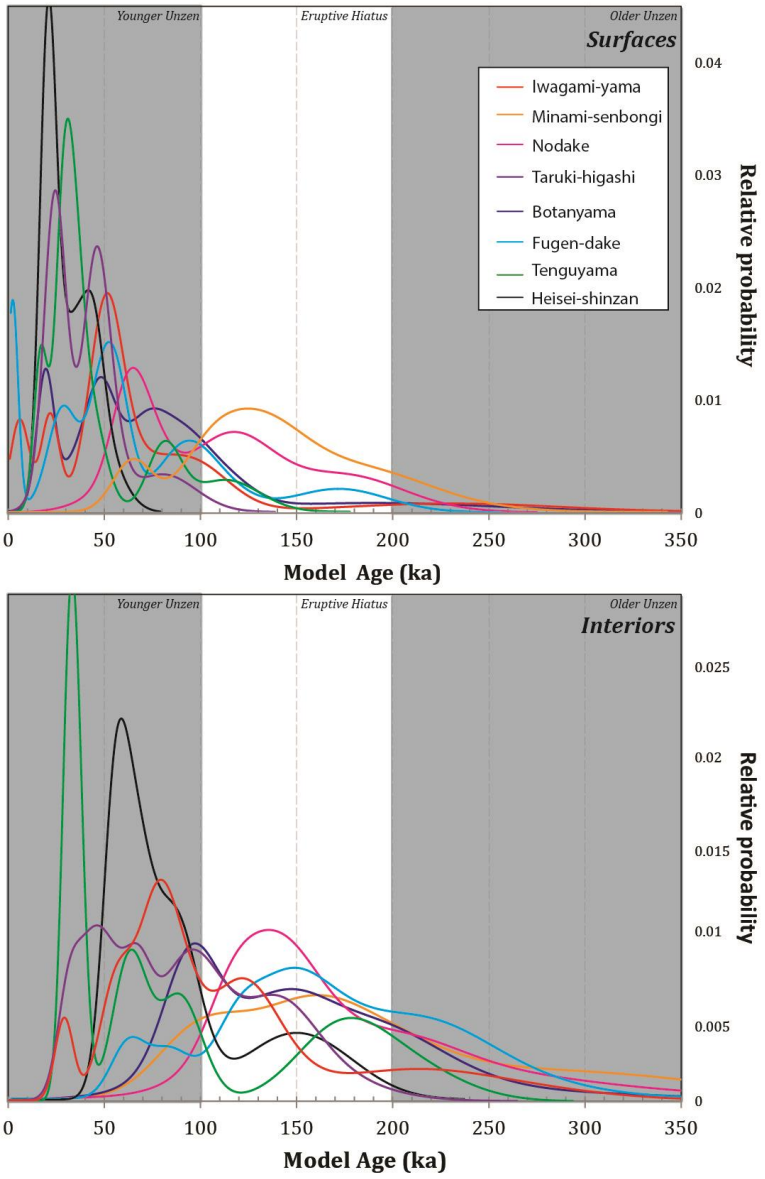

Figure 5.8 Compiled PDF curves for surfaces and interiors of all samples. Relative probability curves decrease towards older model ages, due to increasingly large errors nearing the U/Th equiline.

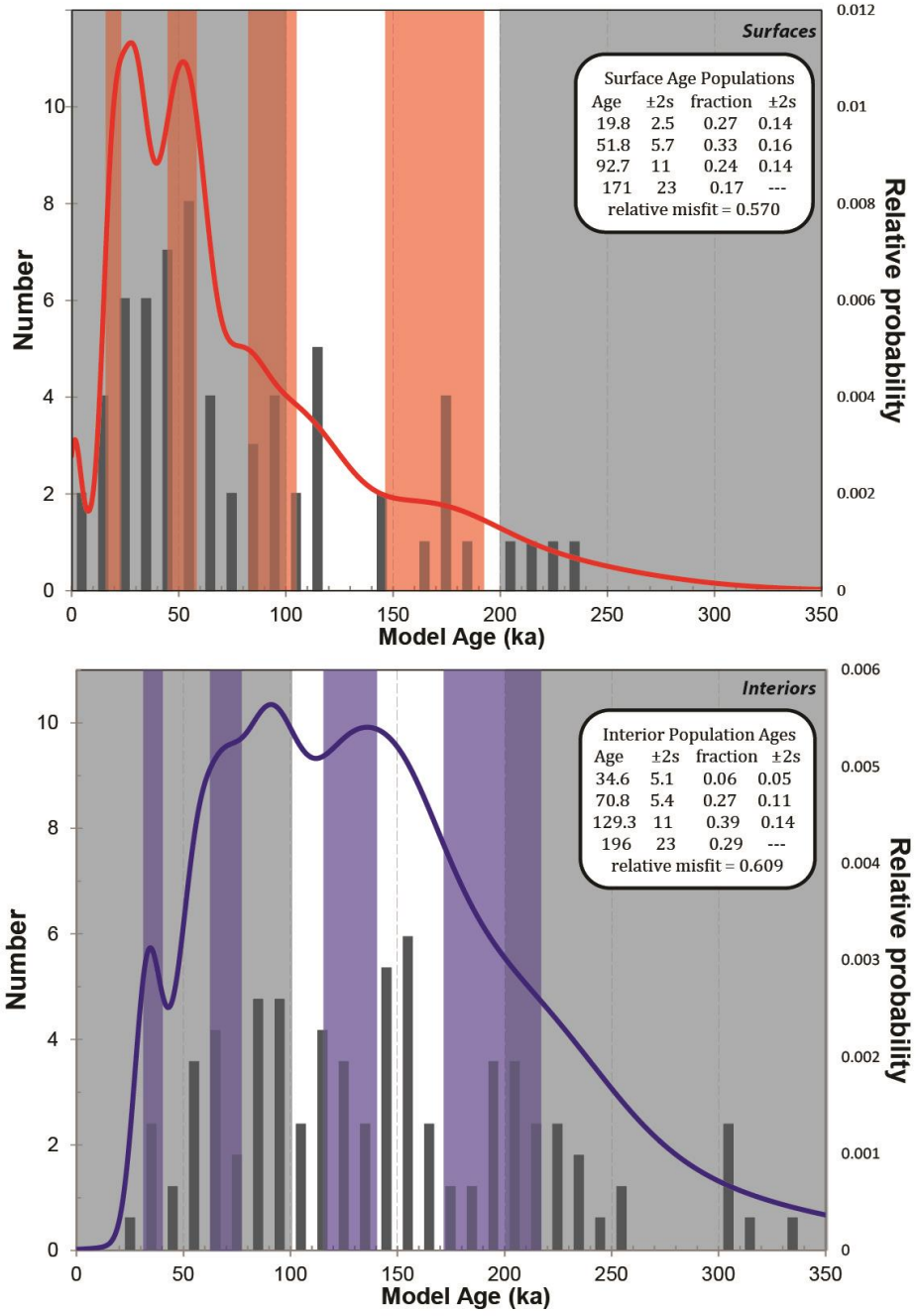

Figure 5.9 Grouped surface (red) and interior (blue) data for all samples. Histograms show number of analysis; samples at secular equilibrium are not included. Unmixing populations represented by red (surface) and blue (interior) fields; age population data is included in the bubble.

5.3.2 Zircon chronochemistry (SIMS coupled age and chemistry results)

Coupled U/Th and trace element data (chronochemistry) was obtained for six samples. Trace element data includes titanium (Ti), hafnium (Hf), gadolinium (Gd), yttrium (Y), uranium (U) and thorium (Th), collected simultaneously with U/Th age measurements using the SHRIMP-RG. Ti and Hf contents appear to vary systematically with time, while Gd, Y, and Th/U remain consistently variable (Figures 5.10 and 5.11).

Ti and Hf show inverse trends with time. Overall, Ti concentrations generally become less variable and decrease with time, with a moderate positive correlation ($r_{Pearson}$= 0.41; $r_{Spearman}$= 0.43; Figure 5.10): during the Older Unzen period (>200 ka) Ti contents ranged from 4.5~9.5 ppm, but range from 3.5~7.5 ppm during the Younger Unzen Period (100 ka-present). The past 50 ka show Ti contents restricted to only 3~5 ppm. Hf contents show the inverse trend, generally increasing with time with a moderate negative correlation with time ($r_{Pearson}$= -0.51; $r_{Spearman}$= -0.53; Figure 5.11): 7000~10,000 ppm in Older Unzen, increasing to 7000~10,500 ppm in Younger Unzen (*note:* Hf contents measured by SIMS are considerable lower and more restricted than those measured by LA-ICPMS). The past 50 ka show Hf contents restricted to high values ranging from 8500~10,500 ppm.

Variations in Th, U, Y and Gd contents are not correlated with time, although all a show a fairly consistent range in values at a given time. Changes in Gd and Y contents are strongly correlated with Th/U ratios (Figure 5.11). The Th/U ratio is generally variable between 0.5~1.0 throughout both eruptive periods and the eruptive hiatus, although rare values >1.0 exist. However, the past 50 ka show a sudden restriction in Th/U, to values between 0.50~0.7. There is no apparent relationship between Th/U and Hf in SIMS measurements (Figure 5.5). Gd and Y show similar behavior to Th/U. Gd is variable between 5~20 ppm through time; however, the past 50 ka also show a sudden restriction to < 10 ppm, which is mirrored by low Th/U values during this time. Uncommonly, Gd contents exceed 20 ppm and are often coupled with high Th/U values (Figure 5.11). Y concentrations range from 250~1300 ppm and are also strongly correlated with Th/U.

Overall, zircon chronochemistry measured using SIMS show trends of increasing Hf and decreasing Ti with time, with values typically being more variable in the Older Unzen period and more restrictive in the Younger Unzen, particularly in the past 50 ka. Th/U, Gd and Y do not show any apparent trends with time, but are strongly correlated to each other.

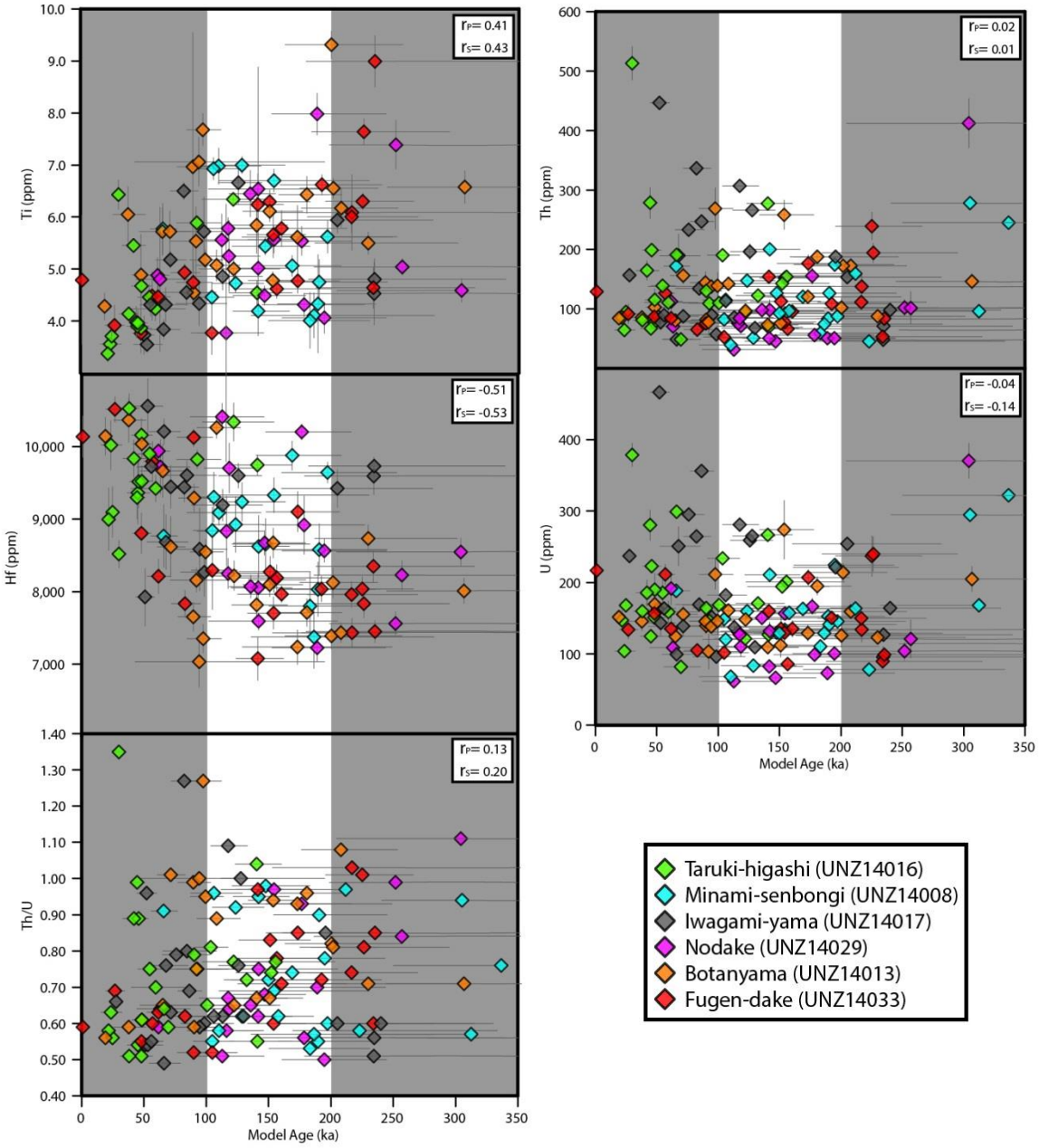

Figure 5.10 Coupled age and trace element data. Pearson product-moment (r_p) and Spearman's rank-order (r_s) correlation coefficients with each variable vs. model age are shown, with detailed calculations available in Appendix C. Shaded regions indicate the Younger and Older Unzen Periods, separated by a period of eruptive quiescence between 200-100 ka.

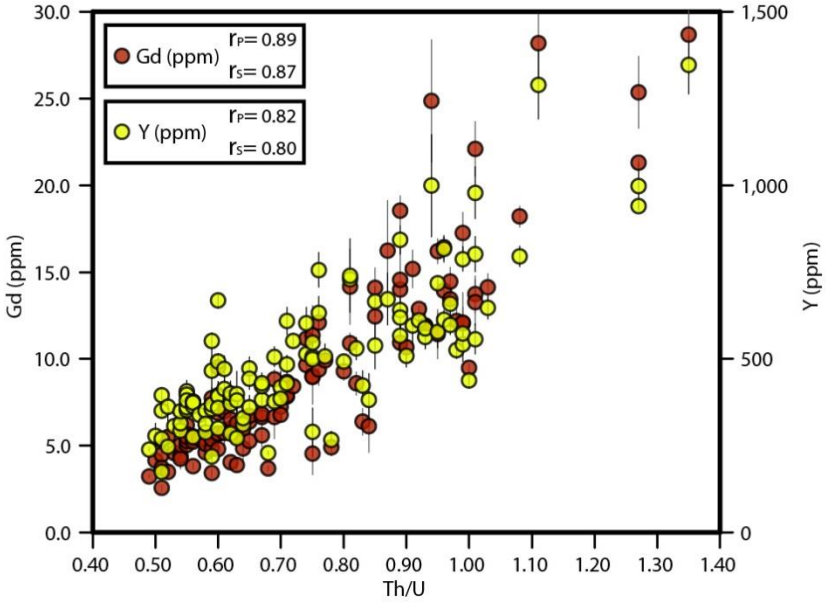

Figure 5.11 Gd and Y vs. Th/U ratios, showing strong positive correlations (r_p=Pearson product-moment correlation coefficient; r_s=Spearman's rank-order correlation coefficient). Like Th/U, neither Gd nor Y show little correlation with time.

5.3.3 $^{40}Ar/^{39}Ar$ geochronology

Age spectra for two eruption samples produced zircon age populations younger than available Ar/Ar and K/Ar eruption ages: Minami-senbongi (UNZ14008) and Iwagami-yama (UNZ14017) (Figure 5.7). In an attempt to better constrain the time of eruption, $^{40}Ar/^{39}Ar$ geochronology was completed on mineral separates and a groundmass concentrate. Fine-grained (150-250 μm fraction) and coarse-grained (250-600 μm fraction) biotite, hornblende, and plagioclase were separated from UNZ14017. Fine-grained and coarse-grained plagioclase and groundmass were separated from UNZ14008; biotite and hornblende crystals were too severely altered for Ar/Ar analyses. Analyses of samples began in May 2015, and limited results are available in this thesis: 1) fine-grained plagioclase multi-crystal incremental heating results for UNZ14017, and 1) coarse-grained plagioclase single-crystal total fusions, 2) fine-grained plagioclase multi-crystal incremental heating, and 3) fine-grained groundmass incremental heating for UNZ14008.

Results for UNZ14017 (Iwagami-yama) are limited to a single multi-crystal incremental heating of fine-grained plagioclase crystals (Table 5.1 and Figure 5.12). Previous estimates of eruption age include 440±240 ka (K/Ar), 335±61 ka (K/Ar), and 213±18 ka (Ar/Ar) (unpublished AIST report 2002). The age spectrum for UNZ14017 shows an initial plateau within error of zero-age until 30% of $^{39}Ar_K$ released, at which point apparent age increases until ~90% $^{39}Ar_K$ released reaching ~3.5 Ma, before tailing off to younger apparent ages in the higher temperature heating steps. Initial K/Ca ratios decrease from 0.17±0.05, eventually leveling off at ~0.052 from 30-90% $^{39}Ar_K$ released, before tailing off to lower values. The inverse isochron diagram shows the $^{39}Ar/^{40}Ar$ vs. $^{36}Ar/^{40}Ar$ and is a good indicator of whether or not a sample contains excess argon. This plot that excess argon is a significant issue for this plagioclase separate. No age plateau or isochron ages were calculated due to excess argon. This analysis yielded a total fusion age of 1.4±0.02 Ma.

Results for UNZ14008 (Minami-senbongi) plagioclase samples include 4 single crystals total fusion experiments (Table 5.2 and Figure 5.13) and a single fine-grained multi-crystal incremental heating experiment (Table 5.3 and Figure 5.14). Previous estimates of eruption age include 187±53 ka (K/Ar; Hoshizumi et al., 1999) and 185±7 ka (K/Ar; unpublished AIST report 2002). Combined single-crystal total fusion ages show a

range in age from within-error of zero-age up to 2.2±0.19 Ma (Figure 5.13). Multi-crystal incremental heating of fine-grained plagioclase produced an age spectrum showing an initial decrease in apparent age from 615.7±433 ka to ~300±20 ka at ~25% $^{39}Ar_K$ released, at which point apparent age increases until ~80% $^{39}Ar_K$ released reaching ~1.7 Ma, then becoming highly variable between 500~1330 ka in the final heating steps (Figure 5.14). Initial K/Ca ratios decrease from 0.15±0.08, eventually leveling at ~0.058 from 35~80% $^{39}Ar_K$ released, then tailing off to lower values at higher temperature steps. The inverse isochron diagram shows that $^{39}Ar/^{40}Ar$ and $^{36}Ar/^{40}Ar$ are highly variable, suggesting again that excess argon is a significant issue for this set of plagioclase analyses. No age plateau or isochron ages was calculated due to excess argon. The multi-crystal analysis yielded a total fusion age of 812±9 ka.

Incremental heating of groundmass from UNZ14008 was also attempted (Figure 5.15). The age spectrum shows an initial increase in apparent age from within-error of zero-age until 20% $^{39}Ar_K$ released, at which point the spectra plateaus at ~195 ka before decreasing at 70% $^{39}Ar_K$ released in the final higher temperature heating steps. Initial K/Ca ratios are high (between 1.8~2.5) until ~35% $^{39}Ar_K$ released, at which point values drastically decrease to ~0.3 until the final high temperature heating step. However, unlike plagioclase analyses, the groundmass yielded a semi-plateau age of 195.6±2.2 ka. This plateau age is also in agreement with its total fusion age of 182.5±1.5 ka, and is also similar when plotted on an inverse isochron plot, which yieled an age of 188.6±12 ka. The inverse isochron diagram shows that $^{39}Ar/^{40}Ar$ values for the calculated age plateau (including 7 heating steps between 5.1-8.4% of laser power) produce an $^{40}Ar/^{36}Ar$ intercept of 333.7±56.8, which is within error of the assumed atmospheric ratio of 295.5.

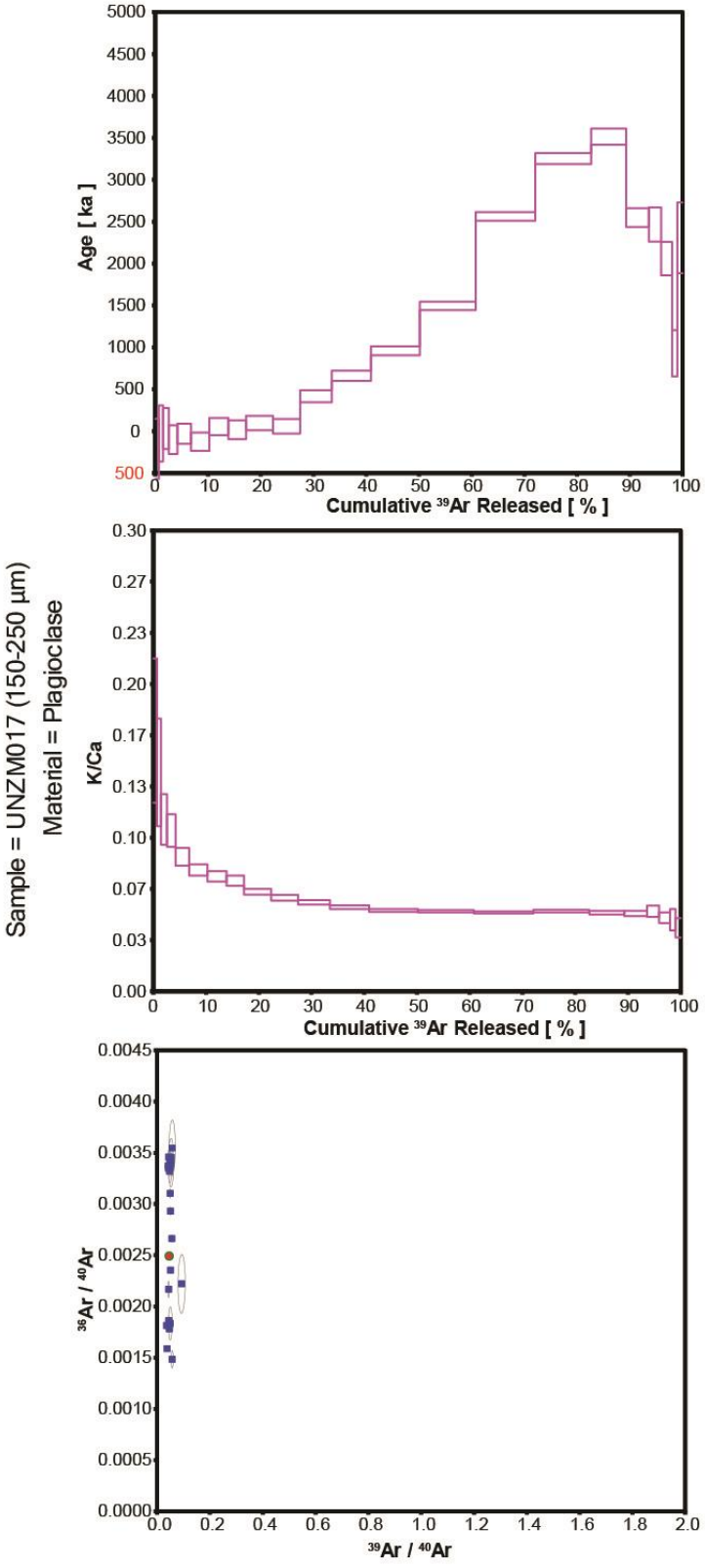

Figure 5.12 Results from UNZ14017 (Iwagamiyama) multi-crystal plagioclase incremental heating experiment. No age plateau was calculated.

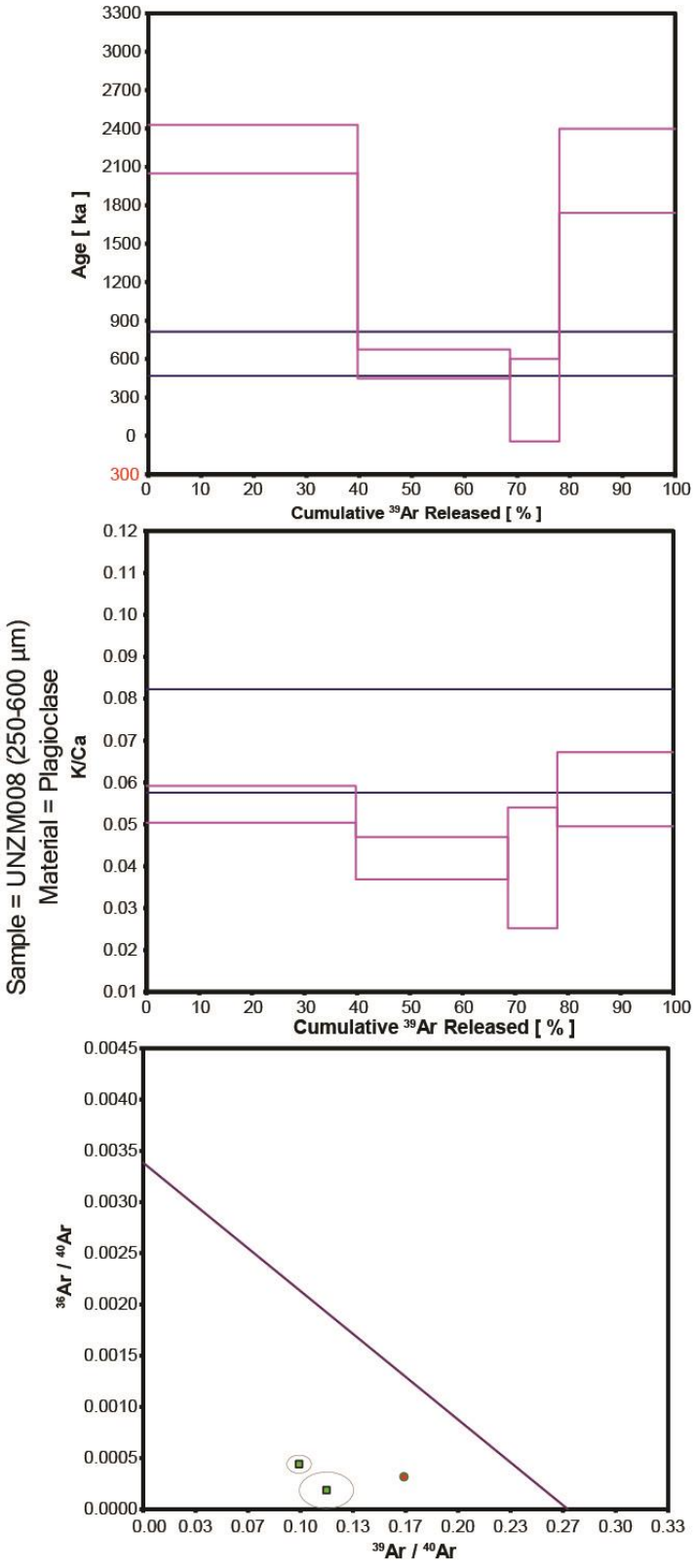

Figure 5.13 Results from UNZ14008 (Minami-senbongi) single-crystal plagioclase total fusion experiment. No age plateau was calculated.

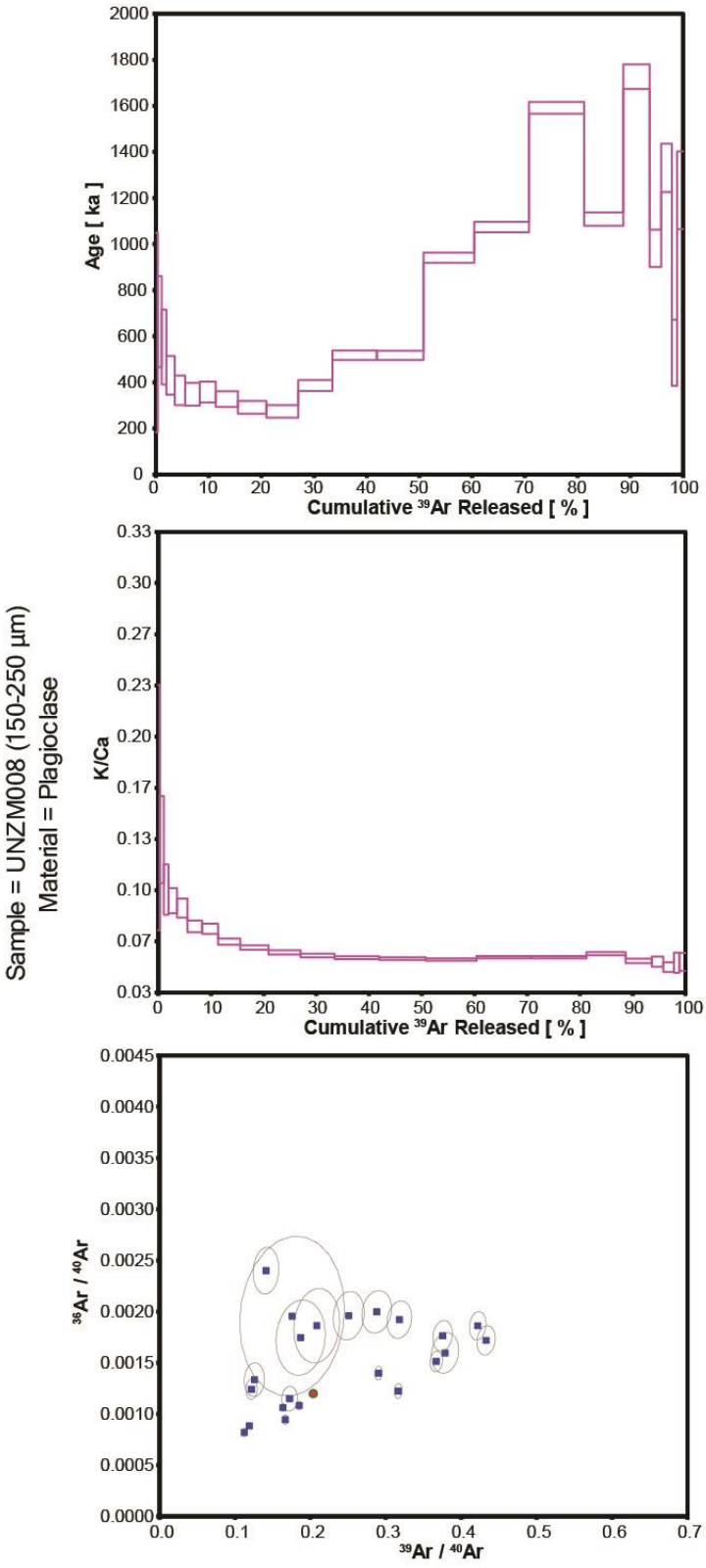

Figure 5.14 Results from UNZ14008 (Minami-senbongi) multi-crystal plagioclase incremental heating experiment. No age plateau was calculated.

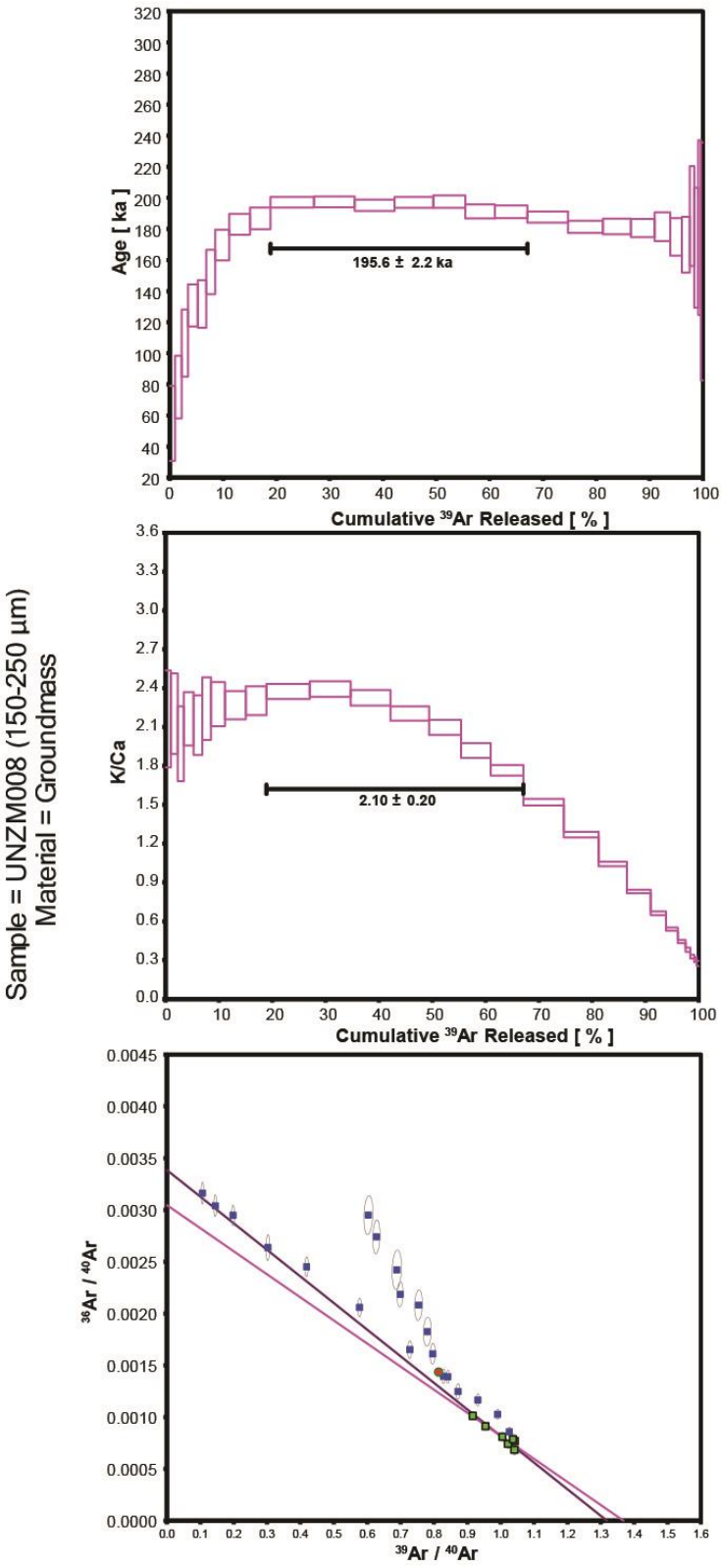

Figure 5.15 Results from UNZ14008 (Minami-senbongi) groundmass concentrate incremental heating experiment.

6 Discussions

Zircon chronochemistry reveals the protracted history of the Unzen Volcanic Complex's upper crustal magma chamber. Past studies suggested that the 1990-1995 eruption at Unzen tapped a magma generated during the 1663 or 1792 eruption (e.g. Nakamura 1995; Nishimura et al., 2005), implying a magma storage time of ~200 years. However, zircon crystals reveal that eruptions at the UVC have been tapping a multi-cycle mush that has been incrementally accumulating since at least the later stages of the Older Unzen period (~200+ ka). Age spectra coupled with zircon chemistry reveal the evolution of the the Unzen Volcanic Complex's upper-crustal magma.

6.1 Zircon crystallization and upper-crustal magma storage

Past studies suggest that the upper-crustal magma of the Unzen Volcanic Complex is stored as a shallow, low-temperature and crystal-rich magma, or "crystal mush". This interpretation is supported by numerous approaches, including petrographic analyses (e.g. Sugimoto et al., 2005; Browne et al., 2006), Fe-Ti oxide re-equilibrium experiments (Venezky and Rutherford 1999), magnetite zoning profiles (Nakamura 1995), melt inclusion analyses (Nishimura et al., 2005), crystallization experiments on Unzen glass (Holtz et al., 2005), and geodetic leveling surveys (Ishihara 1993; Umakoshi et al., 2001). Study of UVC zircon further supports the presence of a low-temperature magma tapped during eruptions at the Unzen Volcanic Complex.

Estimated zircon saturation temperatures (T_{Zr}) and Ti-in-zircon temperatures (T_{Zr}^{Ti}) for the UVC indicate that zircon crystallizes exclusively within the a low-temperature magma. T_{Zr} calculations for UVC from melt inclusions and groundmass glass are between 790~760˚C (Section 4.3). These saturation temperature estimates are supported by Ti-in-zircon temperatures, which reflect actual crystallization temperatures of zircons (e.g. Ferry and Watson 2007), ranging from 790~690 ˚C (Figure 6.1). These crystallization temperatures correspond with estimated temperatures of the shallow, low-temperature (760-800 ˚C) silicic end-member magma for the UVC that is frequently hypothesized by past studies (e.g. Nakamura 1995; Venezky and Rutherford 1999; Holtz et al., 2005; Sugimoto et

al., 2005; Browne et al., 2006). T_{Zr}^{Ti} calculations indicate that zircon crystallization temperatures are too low for growth to occur within the recharge magma (1030-1130˚C) or remobilized magmas (850-965 ˚C) of the UVC (Venezky and Rutherford 1999). T_{Zr} and T_{Zr}^{Ti} suggest that zircon crystallizes exclusively from the upper-crustal magma during storage conditions, which is thought to be in a low-temperature, high-crystalline state of crystal mush. For this reason, zircon chronochemistry can be used to constrain timescales of upper-crustal magma formation and storage condition evolution.

Furthermore, shared zircon chemistry and age spectra, combined with restricted whole-rock chemical trends and petrology between eruption samples dating back to 260 ka, support this study's hypothesis that a single, shared upper-crustal magma has sourced eruptions at the UVC since at least the late Older Unzen period (≥200 ka). First, all eruption samples contain zircon crystals with similar chemistry and age spectra, sharing similar population peaks and individual crystal age ranges (Figures 5.7-5.9). Second, chondrite-normalized REE profiles of zircon crystals are indistinguishable from interiors to surfaces and interiors for crystals from all eruption samples, ranging in age from the most recent into the Older Unzen Period (Figure 6.2); there is also no significant variation in REE chemistry observed between individual eruptions. REE profiles indicate that UVC zircons are typical of unaltered, terrestrial igneous zircon, with a pronounced positive cerium anomaly and a minor negative europium anomaly (e.g. Hoskins and Schaltegger 2003): positive cerium anomalies are thought to develop due to oxidizing conditions in the melt leading to increased Ce^{4+} abundance, which is compatible in zircon due to ionic charge and radius (Hinton and Upton 1991); negative europium anomalies are thought to develop due to plagioclase fractionation depleting Eu from the melt (e.g. Hoskins and Schaltegger 2003) or oxidation due to sulfur degassing (Dilles et al., 2015). Other trace elements (i.e. Y, Nb) are similarly invariable between crystal surfaces and interiors, and between different eruption samples (Figure 5.3). Trace element concentrations and ratios that do show subtle variations with time (Hf and Ti) show consistent, common trends between eruptions (Figure 6.1). Finally, the restricted range in whole-rock compositions) and shared petrographic textures observed in thin section (Section 4.2) from eruption produced throughout UVC eruption history suggest that a common magmatic source is tapped to during eruptions.

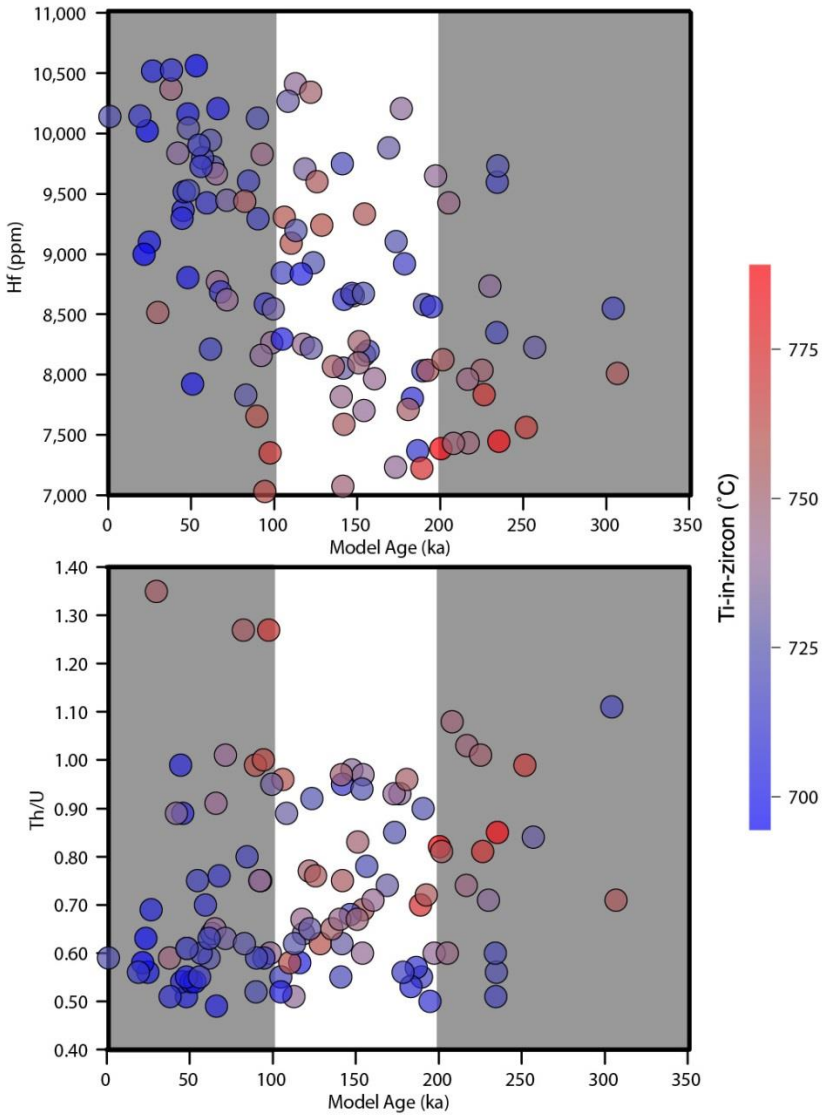

Figure 6.1 Zircon model ages vs. hafnium content (top chart) and Th/U (bottom chart), with Ti-in-zircon temperature calculations represented by bubble color (assuming a_{SiO2}=1 and a_{TiO2}=0.6). The top chart suggest that the UVC shows a trend towards a more evolved melt with time, with zircon crystallizing at lower temperatures; Hf and T_{Zr}^{Ti} show a moderate, inverse correlation ($r_{Pearson}$=-0.43; $r_{Spearman}$=-0.46). The bottom chart suggests that high Th/U ratios are generally associated with higher crystallization temperatures; Th/U and T_{Zr}^{Ti} show a moderate, positive correlation ($r_{Pearson}$=0.48; $r_{Spearman}$=0.53). However, changes in Th/U show no correlation with time; instead, elevated Th/U may indicate down-temperature crystallization of zircon following a mafic recharge event (e.g. Barth and Wooden 2010; Klemetti and Clynne 2014).

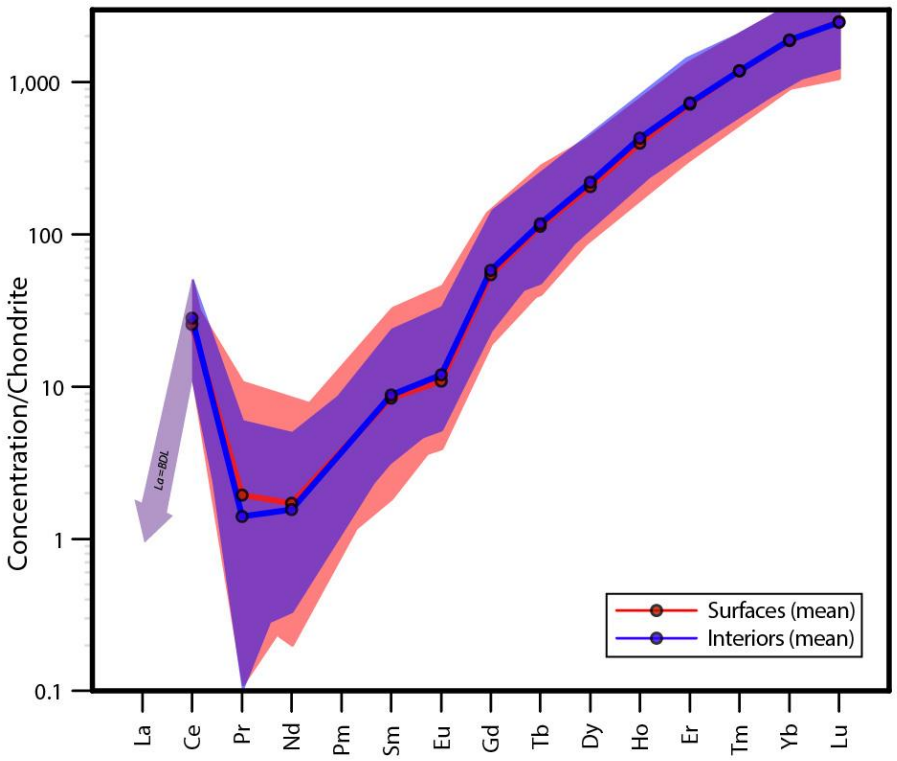

Figure 6.2 Rare-earth element profiles for surfaces and interiors of UVC zircon. Red and blue shaded regions indicate range in data, and lines are means; purple regions represent overlap between surfaces and interiors. No lanthanum (La) data was reduced due to below-dection-limit (BDL) concentrations within the MADER standard, but are expected to be low in unaltered, terrestrial igneous zircon (e.g Hoskins and Schaltegger 2003).

6.2 Zircon crystallization and mafic recharge events

Although upper-crustal magma likely remains in a low-T (near-solidus) state for the majority of its storage duration (Cooper and Kent 2014), punctuated mafic recharge events occurring on timescales of months to years (e.g. Nakamura 1995; Venezky and Rutherford 1999; Browne et al., 2006b) result in elevated temperatures for short periods within localized regions of the crystal mush (e.g. Claiborne et al., 2010; Klemetti and Clynne 2014). Ti-in-zircon temperatures and zircon crystal zonations, which show evidence for past dissoluation (Section 5.1), indicate that UVC zircon do not crystallize from the recharge and remobilized magma. This suggests that upper-crustal magma conditions during recharge events are not recorded in zircon chronochemistry.

Zircon only records magma conditions that have reached zircon saturation temperatures. In under-saturated conditions, zircons will begin to resorb, dissolving in 10s to 100s of years depending on the melt temperature and composition (Harrison and Watson 1983). Crystal zonation of UVC zircon shown in cathodoluminescence images often reveal apparent dissolution textures, such as rounded or mottled zones (Figure 5.2). Rounded zircon crystals are occasionally observed. Crystal morphologies suggest that UVC zircon have been subject to short time periods above zircon saturation temperatures, likely during episodic magma recharge events. Calculated crystallization temperatures (T_{Zr}^{Ti}) do not exceed ~790 ˚C, far below estimated recharged and remobilized magma temperatures. This evidence suggests that UVC zircon do not record short, episodic recharge events, which likely occur in zircon under-saturated conditions.

This assertion is supported by zircon studies from lavas at similar volcanic systems, such as Lassen Volcanic Center (Klemetti and Clynne 2014) and Mt. St. Helens (Claiborne et al., 2010). For these systems, the dearth of eruption-age zircons is interpreted as the result of high temperature, zircon under-saturated conditions during recharge and remobilization. While most UVC eruption samples contain 1~2 crystal surfaces within-error of eruption age, these crystals are a minority; most commonly, crystal surfaces predate eruption by ≥20 ka (Figure 5.6), which is also observed in zircon from lavas of the Lassen Volcanic Center and Mt. St. Helens (Klemetti and Clynne 2014; Claiborne et al., 2010). Zircon crystals are

interpreted as recording the localized history of the crystal mush during storage, between and after rejuvenation events, but not necessarily during one (Klemetti and Clynne 2014).Therefore, zircon growth is not thought to occur during short, periodic recharge events.

6.3 Autocrysts, antecrysts and xenocrysts

Traditionally, the term "phenocryst" is used to describe crystals precipitated from the host magma, while "xenocrysts" describe crystals entrained from wallrocks unrelated to the magmatic system. However, these terms alone do not adequately distinguish the complex origins of crystals in magmatic systems, particularly crystal mushes that accumulate incrementally through periodic pulses of magmatism. Instead, the term "phenocryst" can simply be used as a textural term to describe crystal thats are large relative to groundmass crystallization. Crystals within a lava – both phenocrysts and groundmass phases – can be further divided to distinguish crystals that precipitate from the host magma ("autocrysts") from those crystals that are recycled from earlier phases of magmatism ("antecrysts") (Miller et al., 2007). Here, the host melt is considered the erupted, remobilized crystal mush. As established above by zircon saturation and crystallization temperatures, zircon does not crystallize from either the remobilized or recharge magma. For this reason, zircon crystals are considered antecrysts within erupted materials of the UVC, as they crystallize within the storage conditions of the upper-crustal crystal mush – remnants of previous cycles of magmatism – and not the remobilized magma.

It is possible that zircon can crystallize within the conduit from remnant remobilized mush following eruption, instead of within the crystal mush of the upper-magma chamber. Though still considered antecrysts, these crystal chemistries may not accurately reflect crystal mush conditions. Nonetheless, zircon crystallization occurring within the conduit may be difficult to distinguish from crystal mush crystallization, as both occur in the upper-crustal conditions from cogenetic magmas. However, conduit zircons are likely absent in samples collected directly from dome deposits, which were targeted in sample collection for this study. This is because conduit materials are likely among the first material erupted, forming early stages of dome growth that are particularly prone to collapse into pyroclastic flows (i.e. during the 1991-1995 UVC eruption, at least 13

exogenous lobes formed and suffered collapse; only about half of erupted volume remained as the final 1995 dome; Nakada et al., 1999).

It is also possible that some zircon crystals are sourced from the re-melting of wallrocks solidified during an earlier episode of UVC magmatism (antecrysts) or sourced from basement rocks (xenocrysts). Antecrysts derived from earlier episodes of UVC magmatism still provide valuable chronochemistry data for the system, reflecting conditions of the upper-crustal magma from at the time which they crystallized. There is no indication from zircon chemistry, crystallization temperatures, or morphology (Section 5.1) from crystals younger than U/Th secular equilibrium (~350 ka) that xenocrystic, basement rock zircons comprise any significant portion of sampled crystals. However, zircon interiors at secular equilibrium (less than 10% of measurements) may be of significant age, and the presence of xenocrystic cores cannot be ruled out; these crystals were not included in calculations of unmixing age populations or for chronochemistry results.

6.4 Unzen crystal mush longevity

Zircon age spectra reveal that the upper-crustal magma of the Unzen Volcanic Complex has been accumulating and evacuating gradually over a significant period of time (≥200 ka) during which a portion has always persisted in a zircon-saturated state. Model surface and interior ages of crystals reveal the long history of the UVC crystal mush. Eruption samples contain crystals that typically range from within-error of eruption to 100~200+ ka predating eruption (Figure 5.6). Model ages ranges and PDFs suggest that zircon has been present in the upper crust since at least the late Older Unzen period, although constraining an upper limit is difficult given large age errors of crystals nearing secular equilibrium (Figure 6.3). These age spectra indicate that eruptions at the UVC tap a crystal mush of significant age (>100 ka). Peaks in zircon growth are thought to occur during cooling and crystallization events, possibly corresponding to the down-temperature crystallization after a rejuvenation event, and unmixing age populations may reveal multiple cycles of upper-crustal magma accumulation following significant recharge events (Claiborne et al., 2010; Klemetti and Clynne 2014). However, due to the large relative misfit produced by eruption ages, it is difficult to if or when large zircon populations may have developed in the system (Figure 5.9).

The ubiquitous occurrence of zircon model ages during the apparent eruptive hiatus (200-100 ka) within all eruption samples suggests that magmatic activity continued uninterrupted during this period. The apparent eruptive hiatus is inferred from a lack of surficial deposits within the 200-100 ka age range, but Hoshizumi et al. (1999) suggested that erupted products from this period might be covered by thick Younger Unzen deposits. It is possible for recharge events to occur that don't manifest in eruption (e.g. Couch et al., 2001; Burgisser and Bergantz, 2011), so magmatic activity at the UVC could have continued during the eruptive quiescence period. Continued magmatic activity during eruptive quiescence is also observed in the zircon record from lavas of the Lassen Volcanic Center, CA, USA (Klemetti and Clynne 2014).

The continuous range in model ages extending back to at least the late Older Unzen period indicate that some portion of the UVC crystal mush has always persisted in a zircon-saturated state (≤790˚C), despite short, periodic recharge events. This zircon-saturated region likely varies with time depending on the pathways of rejuvenated melts, producing localized regions or pods of magma with variable thermal histories reflected in the complex variation of zircon age populations (e.g. Claiborne et al., 2010; Storm et al., 2011; Klemetti and Clynne 2014). Individual zircon age spectra for UVC eruption samples (Figure 5.7 and 5.8) show overall similar peaks in zircon growth during the early Younger Unzen period (50-100 ka), but each sample contains complex age populations that may reflect the unique path of remobilized magma through the crystal mush.

However, similarities in age populations of widely separated eruption samples may reveal remobilized mushes that followed similar paths through the crystal mush. A quantitative method for determining if age populations from different eruptions are related is through a Kolmogorov–Smirnov (KS) test, which is a non-parametric test that can be used as a goodness-of-fit test between two sample sets. A probability value (*P)* greater than 0.05 indicates that the populations being compared are indistinguishable to the 95% confidence level, while $P<0.05$ indicates that the hypothesis that two populations are identical is rejected (Press et al., 1988). KS statistics has been successfully used to demonstrate that zircon age populations of different lavas are related (e.g. Schmitt et al., 2010; Tierney 2011). By applying this method to zircon model ages of eruption samples from the UVC, it may be possible to determine if certain eruptions tapped a similar region of crystal mush during

remobilization leading up to eruption (Table 6.1). KS statistics reveal four sets of domes that share similar zircon populations (Figure 6.4). Sets 1, 3 and 4 cluster in the center of the geographic region surrounding the main volcanic edifice, while Set 2 lavas are on the periphery; these sets may reflect eruptions that tapped a similar region within the crystal mush during eruption. Complex age population distributions between samples suggest that the physical distribution of zircon populations within the mush may not be homogenous.

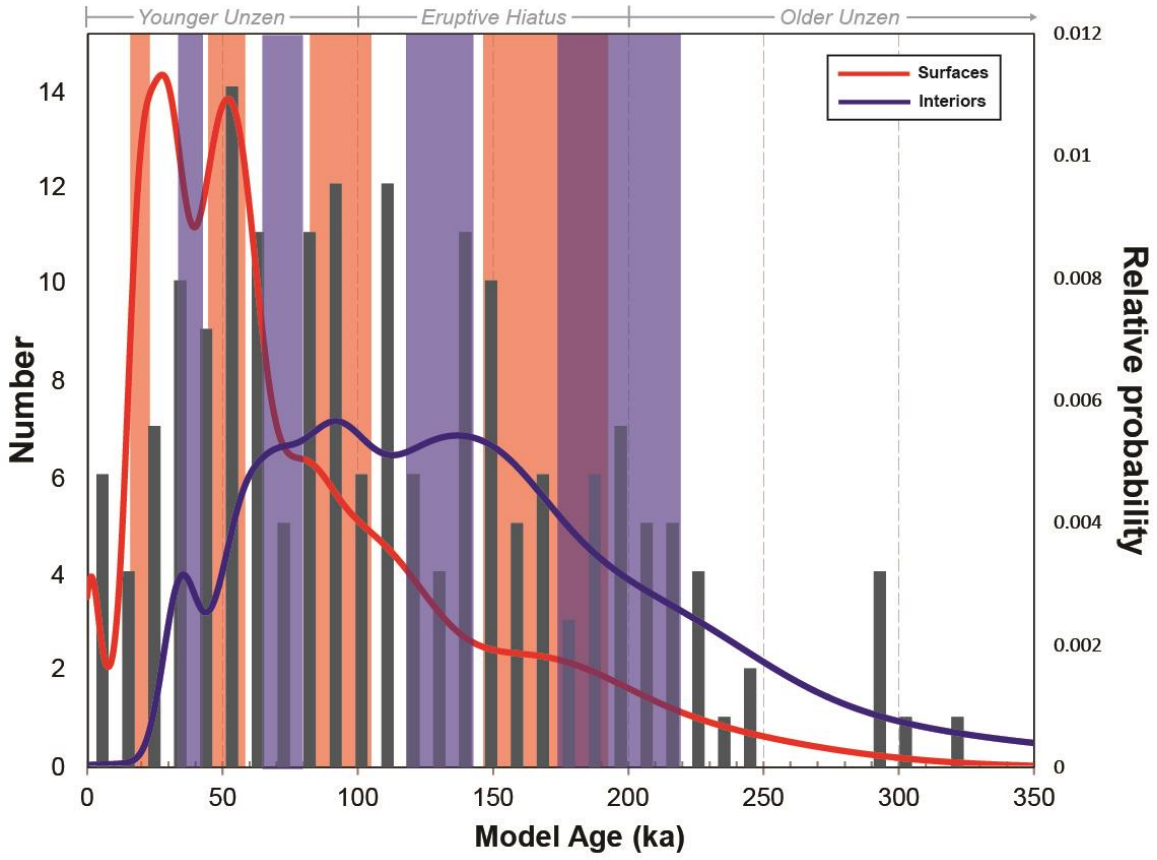

Figure 6.3 Histogram and probability density function plot of UVC zircon surfaces (red) and interiors (blue). Note, crystal model ages at secular equilibrium (≥350 ka) are not included on this diagram. Shaded red and blue regions indicate unmixing age populations for surfaces and interiors, respectively.

Dome 1	Dome 2	D	P	Related?
Heisei-shinzan	Tenguyama	0.54	0.29	x
Heisei-shinzan	Taruki-higashi	0.47	0.26	x
Heisei-shinzan	Minami-senbongi	0.81	0	
Heisei-shinzan	Iwagamiyama	0.38	0.09	x
Heisei-shinzan	Nodake	0.73	0	
Heisei-shinzan	Botanyama	0.61	0	
Heisei-shinzan	Fugen-dake	0.55	0.01	
Tenguyama	Taruki-higashi	0.39	0.09	x
Tenguyama	Minami-senbongi	0.74	0	
Tenguyama	Iwagamiyama	0.47	0.02	
Tenguyama	Nodake	0.72	0	
Tenguyama	Botanyama	0.54	0.01	
Tenguyama	Fugen-dake	0.49	0.02	
Taruki-higashi	Minami-senbongi	0.74	0	
Taruki-higashi	Iwagamiyama	0.47	0.02	
Taruki-higashi	Nodake	0.72	0	
Taruki-higashi	Botanyama	0.39	0.03	
Taruki-higashi	Fugen-dake	0.49	0.02	
Minami-senbongi	Iwagamiyama	0.55	0	
Minami-senbongi	Nodake	0.24	0.46	x
Minami-senbongi	Botanyama	0.33	0.12	x
Minami-senbongi	Fugen-dake	0.29	0.23	x
Iwagamiyama	Nodake	0.53	0	
Iwagamiyama	Botanyama	0.33	0.09	x
Iwagamiyama	Fugen-dake	0.46	0.01	
Nodake	Botanyama	0.32	0.15	x
Nodake	Fugen-dake	0.25	0.41	x
Botanyama	Fugen-dake	0.21	0.62	x

Table 6.1 KS statistics comparing zircon age populations between individual domes. *P*>0.05 indicates that samples are related.

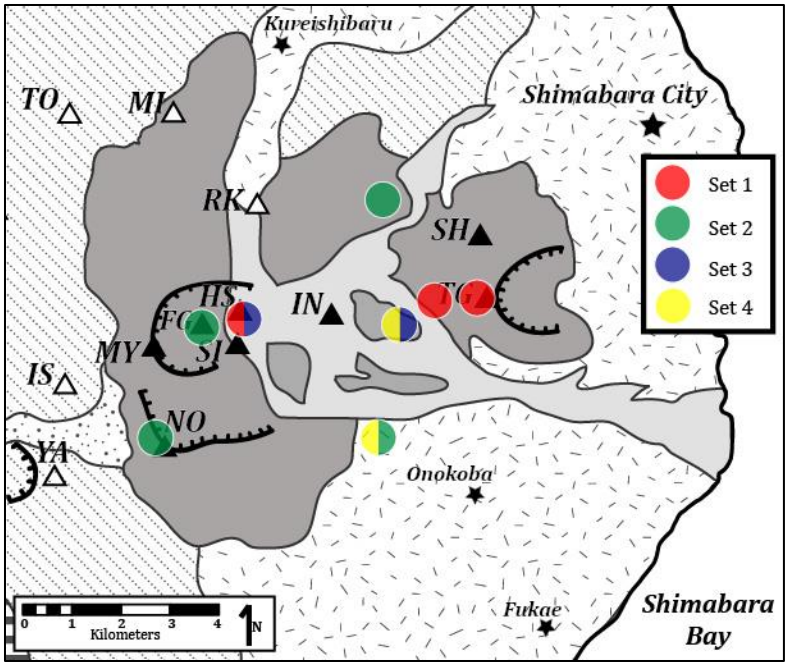

Figure 6.4 Geographic relationships between lavas with related age populations, as determined by KS statistics. Sets that overlap are indicated by circles with split colors.

6.5 Unzen crystal mush evolution

Subtle variations in zircon trace element chemistry can be used as a proxy for melt evolution (Hf contents; Claiborne et al., 2006), zircon crystallization temperatures (T_{Zr}^{Ti} thermometry; Ferry and Watson 2007), and changes in mafic input (Th/U; e.g. Klemetti and Clynne 2014). Coupled with U/Th model ages, zircon chemistry reveals how the upper-crustal magma at the Unzen Volcanic complex has evolved over the past 10^4~10^5 years.

During the Older Unzen period (500-200 ka), the UVC upper-crustal magma was a more homogeneous, well-mixed body. This is represented by restricted Th/U (LA-ICPMS: 0.3~1.0; Figure 5.5/SIMS: 0.5~1.1; Figure 6.1) and Eu/Eu* (LA-ICPMS: 0.3~0.7; Figure 5.5) values shown in data from zircon of the Older Unzen period. Titanium concentrations during this period vary from 4~10 ppm (SIMS; Figure 5.10), and T_{Zr}^{Ti} range from 790~725˚C (Figure 6.1). On average, hafnium contents are lower for zircon crystallized during the Older period (SIMS: 7000~10,000 ppm; LA-ICPMS: 6000~12,000 ppm), indicating zircon crystallization from a less evolved melt. Zircon chronochemistry suggests that the crystal mush during the Older Unzen period was a relatively homogeneous and well-mixed body.

Through the eruptive hiatus (200-100 ka) and into the Younger Unzen period (100 ka – present), the UVC crystal mush may have gradually evolved into a more mature – or, a more evolved and thermally-complex, heterogeneous – magma. This development is shown by the larger variations in Th/U (LA-ICPMS: 0.3~1.5/SIMS: 0.5~1.35) and Eu/Eu* (LA-ICPMS: 0.3~0.9) values of zircon from Younger Unzen eruption samples. Titanium concentrations are more restricted and lower (SIMS: 3~6 ppm; Figure 5.10) compared to zircon crystallized during the Older period, and T_{Zr}^{Ti} range from 750~685˚C (with one outlier at 775˚C; Figure 6.1). These crystallization temperatures show that Younger zircons crystallize at lower temperatures, which may reflect a gradual cooling of the crystal mush during storage conditions, or possibly a gradual change in melt composition leading to lower zircon saturation temperatures. Generally, hafnium contents are higher for zircon crystallizing during the Younger period (SIMS: 8000~10,500 ppm); LA-ICPMS measurements range from 6000~12,000 ppm for Younger Unzen eruption samples, but the upper-limits on timing of zircon crystallization is not known for these spots.

In particular, the past 50 ka of the Younger Unzen period show a sudden restriction in trace element concentrations (Section 5.3.2), and the two most recent sampled eruptions (Heisei-shinzan, 1995; Tenguyama 3±1 ka) contain no zircon model ages within-error of eruption; the youngest model ages for these eruptions predate eruption by 15~20 ka (Figure 5.7). In particular, T_{Zr}^{Ti} are typically <725˚C during this interval (Figure 6.1). This may suggest that differences in zircon saturation conditions between the crystal mush and recharge magma are becoming greater, leading to increasing dissolution of zircon during recharge. Or, the lack of high-temperature crystallizing zircon crystals may indicate that localized zircon-undersaturated regions of the mush have developed and are tapped frequently during the recent Younger eruptions; in these zones, zircon growth may not occur. A final possibility is that zircon growth has stalled in the past 50 ka because a large portion of the crystal mush was dropped below solidus. Recent recharge events may re-melt and entrain zircon crystals, and other antecrysts, from this hot sub-solidus body, as has been suggested to occur during large silicic eruptions (e.g. Charlier et al., 2005; Bindeman et al., 2006). All possibilities suggest that the crystal mush of the Younger Unzen period has evolved towards a more heterogeneous, poorly-mixed body, with localized regions of contrasting thermal and compositional characteristics. Geodetic surveys revealing possible pockets of magma at shallow depths (Ishihara 1993) may represent warmer regions within the mush. Since the Older Unzen period (500-200 ka), the UVC upper-crustal magma has evolved towards a more silicic and heterogeneous body that is subject to regular recharge events.

6.6 Ar/Ar geochronology and argon excess issues

$^{40}Ar/^{39}Ar$ geochronology was attempted on mineral and groundmass separates from two samples that produced crystal model ages younger than previous K/Ar and/or Ar/Ar measurements in an attempt to better constrain the eruption ages at the UVC. This dating method is difficult at the UVC, given that it is a young active system lacking sanidine. Limited results on single-crystal and multi-crystal plagioclase separates produce ages with low precision, and inverse isochrons suggest that plagioclase contains excess argon. Therefore, Ar/Ar analyses of plagioclase are unlikely to produce an accurate eruption ages at the UVC.

Incremental heating of groundmass from Minami-senbongi (UNZ14008) produced a semi-plateau of 195.6±2.2 ka, and a total fusion age of 182.5±1.5 ka (Figure 5.15). These results are within error of previous ages of 187±53 ka (K/Ar; Hoshizumi et al., 1999) and 185±7 ka (K/Ar; unpublished AIST report 2002), demonstrating that precise and reproducible results from groundmass can be obtained from this eruption sample (although the phase separates used in previous studies are not reported). Nonetheless, 2 zircon crystals produce paired interior-surface ages younger than either the groundmass ages from this study (Figure 5.7). This eruption sample contained heavily altered and/or replaced hornblende and biotite crystals, suggesting that it may be affected by alteration processes, such as hydrothermal alteration. Given the reproducibility of this age (~185 ka) from multiple K/Ar and Ar/Ar studies, it would be prudent to reconsider the outlying zircon model ages at 2 σ errors, instead of the conventional reporting of U/Th zircon model ages at 1σ errors.

Additional results from hornblende and biotite separates are forthcoming, but not reported here. Preliminary analyses of incremental heating from a multi-crystal hornblende separate of Iwagamiyama (UNZ14017) have produced extremely low-levels of radiogenic gas, reflecting either a recent (zero-age~1000s years ago) eruption, supported by zircon model ages (Figure 5.7), or argon loss. If this eruption is young (~20 ka or younger), then Ar/Ar geochronology may not be possible given available phases, specifically the lack of high-potassium minerals such as sanidine. This likely presents an issue for determining eruption ages from deposits of the Younger Unzen period by Ar/Ar dating methods.

6.7 Overall upper-crustal magma chamber model for the Unzen Volcanic Complex

Using zircon chronochemistry trends, a model of upper-crustal magma evolution can be created for the Unzen Volcanic Complex from the Older Unzen to Younger Unzen period (Figure 6.5). During the Older Unzen period (≥200 ka), the upper-crustal magma was likely a smaller, more homogenous body. Individual recharge events would result in a less evolved, well-mixed body, with zircon beginning to crystallize at ~790˚C. Surrounding wallrock consisted of basement rocks of the Shimabara Peninsula or sub-solidus volcanic rocks of the Pre-Unzen period (>500 ka), which may have been re-melted and entrained in

remobilized plumes. Less evolved, well-mixed upper-crustal magma conditions may be reflected in eruptive characteristics during this period, which are characterized primarily by thick, effusive lava flows and intermediate lavas containing more pyroxenes and fewer hydrous phases, and few pyroclastic deposits (e.g. Hoshizumi et al., 1999). Zircon crystals within an Older Unzen eruption are of a more restricted chemistry, and likely contained similar age populations between Older eruptions, due to the well-mixed nature of the Older crystal mush.

During the eruptive hiatus (200-100 ka) and into the Younger Unzen period, the UVC crystal mush became increasingly larger and more "mature," developing into a larger heterogeneous body with localized regions of contrasting thermal and possibly compositional characteristics. Whether or not changes in recharge flux or composition also occurred during this period is difficult to evaluate, because zircon does not crystallize during recharge events. However, if elevated Th/U ratios are interpreted to indicate the down-temperature crystallization of zircon following recharge events, then Th/U ratios of Unzen zircon suggest that thermal inputs continued uninterrupted from the Older period through the eruptive hiatus and into the Younger period (Figure 6.1). Spikes in Th/U ratios for interiors of Younger Unzen eruption samples may reflect down-temperature crystallization after significant recharge events occurring throughout the period (Figure 6.3). Overall, the larger volume of the Younger crystal mush will buffer temperature changes during relatively small-volume recharge events, and higher viscosity of a more evolved magma will prevent efficient mixing; therefore, minor recharge events may only influence a localized region of the mush, developing the heterogeneities within the crystal mush. For this reason, localized regions may experience different thermal events through time, and physical zircon population distributions within the upper-crustal magma will become increasingly variable.

Upper-crustal magma conditions during the Younger Unzen period are characterized by a larger, more poorly-mixed system that has been incrementally accumulating since the Older Unzen period. The crystal mush has become more poorly-mixed and cooler overall, although large localized thermal contrasts likely exist. Zircon typically begins to crystallize at ~750˚C. Wall rocks surrounding the chamber likely consist of sub-solidus volcanic rocks of the UVC, surrounded by plutonic rocks of older (>350 ka)

UVC magmatism. Upper-crustal magma conditions may be reflected in a change in eruptive character between Older and Younger Unzen periods, as Younger eruptions are dominantly characterized by dome-building and collapse events, generating significant pyroclastic flow deposits. Intermediate lavas contain more hydrous phases, and fewer pyroxenes, compared to Older eruptive products. Zircon crystals within Younger eruption samples show more variable chemistry and complex age populations, indicative of the thermal heterogeneity within the system.

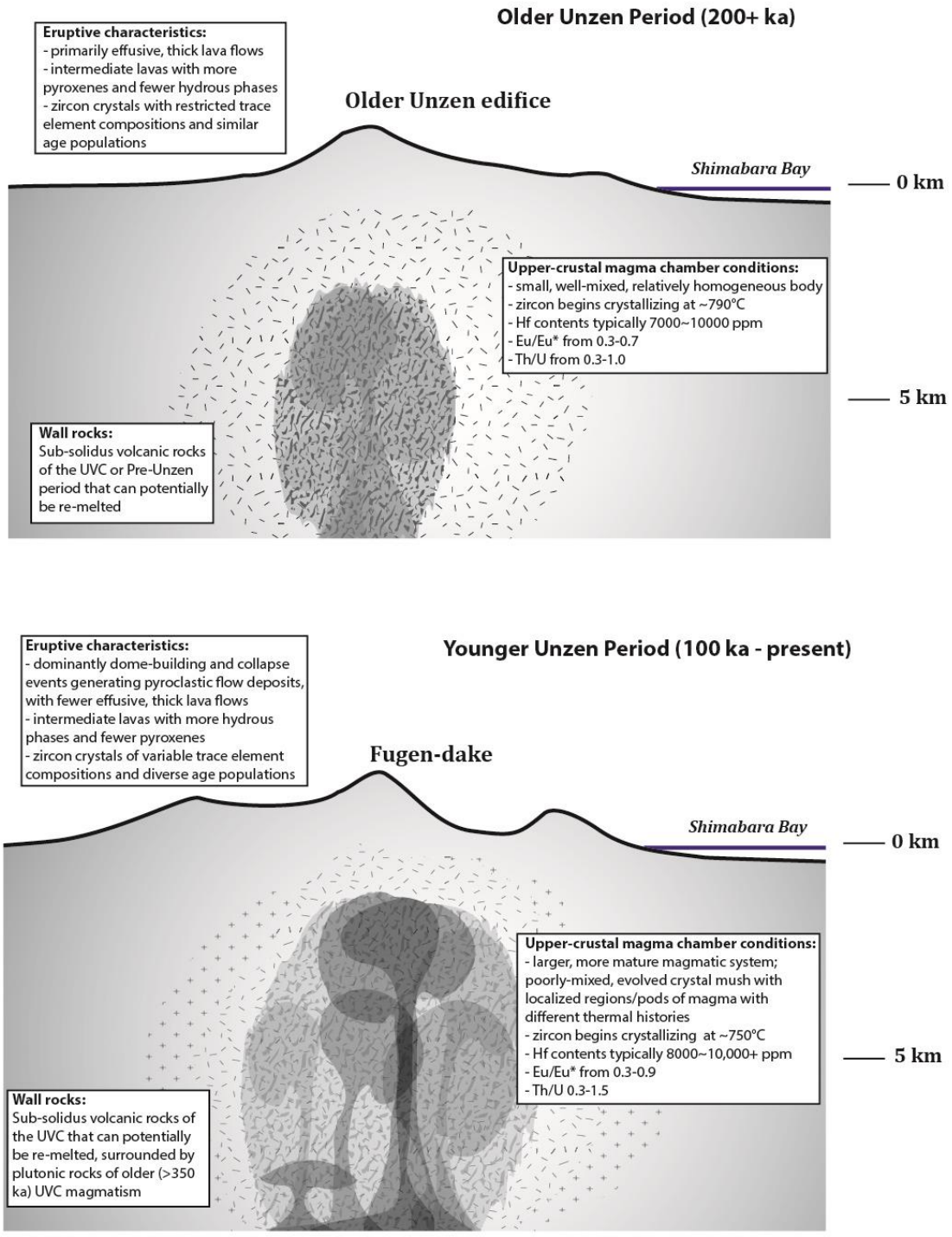

Figure 6.5 Model of crystal mush evolution at the Unzen Volcanic Complex from the Older Unzen to the Younger Unzen period. Darker shades of gray indicate regions of the magma that have been more frequently reheated during recharge events. Hatching represents hot, sub-solidus plutonic rocks of previous magmatic cycles that may be re-melted and entrained during remobilization. Hafnium ranges from SIMS data, Eu/Eu* and Th/U ratios from LA-ICPMS.

7 Conclusions

Zircon chronochemistry has revealed the history and evolution of upper-crustal magma at the Unzen Volcanic Complex. Upper-crustal magma is stored in a low temperature (≤790˚C) crystalline state known as crystal mush. Individual zircon surface-interior age pairs, together with zircon age spectra, suggest that portions of this crystal mush have been present in the crust since at least the late Older Unzen period (≥200 ka). Zircon population peaks exist during the apparent eruptive hiatus from 200-100 ka, suggesting that magmatic activity continued uninterrupted. Zircon of Older Unzen eruption samples show restrictive chemistry, suggesting that crystallization occurred in a more homogenous, less evolved crystal mush, compared to zircon of Younger Unzen (100 ka – present) that record variable storage conditions skewed towards a more evolved, poorly-mixed crystal mush. Complex age populations, particularly from eruption samples of the Younger Unzen period, suggest that localized regions within the crystal mush have different thermal histories, and that the zircon age populations within an eruption reflect the path taken by remobilized magma as it rose through the crystal mush. Since the Older Unzen period, zircon chronochemistry suggests that the upper-crustal magma has evolved to a mature, heterogeneous crystal mush zone, containing thermally contrasting localized regions.

Remaining questions:

1) Do these results reflect the typical evolution of upper-crustal magma at active intermediate arc systems? This is the fundamental question generated by this zircon study at the Unzen Volcanic Complex and can only be answered through additional studies at similar systems.
2) Approximately 5% of samples were at U/Th secular equilibrium (≥350 ka). Do these crystals represent older upper-crustal magmatic activity at the UVC? Or, are these xenocrystic basement cores? U-Pb dating on interior ages at secular equilibrium will help determine the origin of crystal interiors near or at U/Th secular equilibrium.
3) What are the upper-limits of crystal mush storage durations? U/Th age errors grow increasing larger as measurements near the equiline, making it difficult to accurately determine older ages.

4) The unexpected discovery of zircon model ages younger than available K/Ar and/or Ar/Ar ages for two samples may warrant a re-evaluation of the presumed eruption ages of these units; zircon model ages suggest both these units belong to the Younger Unzen period, not the Older Unzen period. Can Ar/Ar dating provide an accurate measure of eruptions of younger UVC eruptions given the absence of sanidine?

References Cited

** in Japanese only*

Bachmann, O., Bergantz, G.W. (2004). On the origin of crystal-poor rhyolites: extracted from batholithic crystal mushes. *Petrology, 45*(8), 1565-1582.

Bachmann, O., Bergantz, G. W. (2006). Gas percolation in upper-crustal silicic crystal mushes as a mechanism for upward heat advection and rejuvenation of near-solidus magma bodies. *Journal of Volcanology and Geothermal Research, 149*(1-2), 85-102.

Bachmann, O., Bergantz, G.W. (2008). The magma reservoirs that feed supereruptions. *Elements, 4,* 17-21.

Baker D. R., Conte A. M., Freda C., and Ottolini L. (2002) The effects of halogens on Zr diffusion and zircon dissolution in hydrous metaluminous granitic melts. *Contrib. Mineral. Petrol.* 142, 666–678.

Barth, A.P., Wooden, J.L. (2010). Coupled elemental and isotopic analyses of polygenetic zircons from granitic rocks by ion microprobe, with implications for melt evolution and the sources of granitic magmas. *Chemical Geology, 277*(1-2), 149-159.

Barth, A.P., Wooden, J.L., Jacobson, C.E., Economos, R.C. (2013). Detrital zircon as a proxy for tracking magmatic arc system: the California arc example. *Geology, 41*(2), 223-226.

Bindeman, I. N., Valley, J. W., Wooden, J. L., & Persing, H. M. (2001). Post-caldera volcanism: in situ measurement of U-Pb age and oxygen isotope ratio in Pleistocene zircons from Yellowstone caldera. *Earth and Planetary Science Letters, 189*(3-4), 197-206.

Bindeman, I., Schmitt, A., & Valley, J. (2006). U–Pb zircon geochronology of silicic tuffs from the Timber Mountain/Oasis Valley caldera complex, Nevada: Rapid generation of large volume magmas by shallow-level remelting. *Contrib Mineral Petrol, 152*, 649-665.

Blake, S. (1981). Volcanism and the dynamics of open magma chambers. *Nature*, *289*(5800), 783-785.

Blake, S., Brown, G., Butler, R., Drury, S., Harris, N., Hawkesworth, C., & Thorpe, R. (1990). Block 3: Volcanic Arcs. In *S339 Understanding the continents: Tectonic and thermal processes of the lithosphere*. Dorchester, Dorset: The Open University.

Brophy, J. (1991). Compositions gaps, critical crystallinity, and fractional crystallization in orogenic (calc-alkaline) magmatic systems. *Contributions to Mineralogy and Petrology, 109*(2), 173-182.

Browne, B., Eichelberger, J., Patino, L., Vogel, T., Dehn, J., Uto, K., et al. (2006). Generation of

porphyritic and equigranular mafic enclaves during magma recharge events at Unzen Volcano, Japan. *Journal of Petrology*, *47*(2), 301-328.

Browne, B., Eichelberger, J., Patino, L., Vogel, T., Uto, K., & Hoshizumi, H. (2006b). Magma mingling as indicated by texture and Sr /Ba ratios of plagioclase phenocrysts from Unzen volcano, SW Japan. *Journal of Volcanology and Geothermal Research,* 154, 103-116.

Brown S. J. A. and Fletcher I. R. (1999) SHRIMP U-Pb dating of pre-eruption growth history of zircons from the 340 ka Whakamaru Ignimbrite, New Zealand: Evidence for 250 k.y. magma residence times. *Geology, 27*, 1035–1038.

Burgisser, A., & Bergantz, G. (2011). A rapid mechanism to remobilize and homogenize highly crystalline magma bodies. *Nature*, 471, 212-214.

Carrigan C.R., Schubert G., Eichelberger J.C. (1992). Thermal and dynamical regimes of single- and two-phase magmatic flow in dikes. *J Geophys Res, 97,* 377–392.

Charlier, B., Peate, D., Wilson, C., Lowenstern, J., Storey, M., Brown, S. (2003). Crystallization ages in coeval silicic magma bodies: ^{238}U-^{230Th} disequilibrium evidence from the Rotoiti and Earthquake Flat eruption deposits, Taupo Volcanic Zone, New Zealand. *Earth Plant Sci Letter, 206,* 441-457.

Charlier, B., Wilson, C., Lowenstern, J., Blake, S., Van Calsteren, P., & Davidson, J. (2005). Magma Generation at a Large, Hyperactive Silicic Volcano (Taupo, New Zealand) Revealed by U–Th and U–Pb Systematics in Zircons, *Petrology, 46*(1), 3-32.

Cherniak D. J. and Watson E. B. (2001) Pb diffusion in zircon. *Chem. Geol. 172*, 5–24.

Cimarelli, C., Costa, A., Mueller, S., & Mader, H. (2011). Rheology of magmas with bimodal crystal size and shape distributions: Insights from analog experiments. *Geochem. Geophys. Geosyst., 12,* 1-14.

Claiborne, L., Miller, C., Flanagan, D., Clynne, M., & Wooden, J. (2010). Zircon reveals protracted magma storage and recylcing beneath Mount St. Helens. *Geology, 38,* 1011-1014.

Claiborne, L.L., Miller, C.F., Walker, B.A., Wooden, J.L., Mazdab, F.K., Bea, F. (2006). Tracking magmatic processes through Zr/Hf ratios in rocks and Hf and Ti zoning in zircons: An example from the Spirit Mountain batholith, Nevada. *Mineralogical Magazine, 70*(5), 517-543.

Coath, C. & Reid, M.R. (2000). In situ U-Pb ages of zircons from the Bishop Tuff: No evidence for long crystal residence times. *Geology, 28*(5), 443-446.

Cooper K., & Donnelly C. (2008). ^{238}U-^{230}Th-^{226}Ra disequilibria in dacite and plagioclase from the 2004-2005 eruption of Mount St. Helens. *A Volcano Rekindled: The renewed eruption of Mount St. Helens 2004-2006*, 827-846.

Cooper, K., & Kent, A. (2014). Rapid remobilization of magmatic crystals kept in cold storage. *Nature, 506*, 480-499.

Cooper, K., & Reid, M. (2008). Uranium-series Crystal Ages*. Reviews in Mineralogy and Geochemistry, 69*, 479-544.

Cottrell, E., Spiegelman, M., & Langmuir, C. H. (2002). Consequences of diffusive reequilibration for the interpretation of melt inclusions. *Geochemistry Geophysics Geosystems, 3*.

Couch, S., Sparks, R., & Carroll, M. (2001). Mineral disequilibrium in lavas explained by convective self-mixing in open magma chambers. *Nature*, 411, 1037-1039.

Crowley, J.L., Schoene, B., Bowring, S.A. (2007). U-Pb dating of zircon in the Bishop Tuff at the millennial scale. *Geology, 35*(12), 1123-1126.

Danyushevsky, L. V., Della-Pasqua, F. N., & Sokolov, S. (2000). Re-equilibration of melt inclusions trapped by magnesian olivine phenocrysts from subduction-related magmas: petrological implications. *Contributions to Mineralogy and Petrology, 138*(1), 68-83.

de Silva, S., Salas, G., & Schubring, S. (2008). Triggering explosive eruptions - the case for silicic magma recharge at Huaynaputina, southern Peru. *Geology, 36*(5).

Devine, J., Rutherford, M., Norton, G., & Young, S. (2003). Magma storage region processes inferred from geochemistry of Fe-Ti oxides in andesitic magma, Soufriere Hills Volcano, Montserrat, WI. *Journal of Petrology*, *44*(8), 1375-1400.

Dilles, J.H., Kent, A.J.R., Wooden, J.L., Tosdal, R.M., Koleszar, A., Lee, R.G., Farmer, L.P. (2015). Zircon compositional evidence for sulfur-degassing from ore-forming arc magmas. *Economic Geology, 110,* 241-251.

Eichelberger, J., Carrigan, C., Westrich, H., & Price, R. (1986). Non-explosive silicic volcanism. *Nature*, *323*(16), 598-602.

Eichelberger, J. (1995). Silicic volcanism: Ascent of viscous magmas from crustal reservoirs. *Annu. Rev. Earth Planet. Sci*., *23*, 41-63.

Eichelberger, J. (1978). Andesitic volcanism and crustal evolution. *Nature, 275*, 21-27.

Eichelberger, J. C., Chertkoff, D. G., Dreher, S. T., & Nye, C. J. (2000). Magmas in collision: rethinking chemical zonation in silicic magmas. *Geology*, 28(7).

Faure, F., & Schiano, P. (2005). Experimental investigation of equilibration conditions during forsterite growth and melt inclusion formation. *Earth and Planetary Science Letters, 236*(3-4), 882-898.

Ferry, J., & Watson, E. (2007). New thermodynamic models and revised calibrations for the Ti-in-zircon and Zr-in-rutile thermometers*. Contrib Mineral Petrol*, 429-437.

Harrison T. M. and Watson E. B. (1983) Kinetics of zircon dissolution and zirconium diffusion in granitic melts of variable water content. *Contrib. Mineral. Petrol., 84*, 66–72.

Harrison, T.M., Blichert-Toft, J., Muller, W., Alberede, F., Holden, P., Mojzsis, S.J. (2005). Heterogeneous Hadean Hafnium: Evidence of Continental Crust at 4.4 to 4.5 Ga., *Science, 310*(5756), 1947-1950.
Hanchar, J., & Watson, E. (2003). Zircon Saturation Thermometry. *Reviews in Mineralogy and Geochemistry*, 53.

Hildreth, W. (2004). Volcanological perspcetives on Long Valley, Mammoth Mountain, and Mono Craters: several contiguous but discrete systems. *Volcanology and Geothermal Research, 136,* 169-198.

Hinton, R.W., Upton, B.G.J. (1991). The chemistry of zircon: variations within and between large crystals from syenite and alkali basalt xenoliths. *Geochim Cosmochim Acta, 55,* 3287-3302.

Holtz, F., Sato, H., Lewis, J., Behrens, H., Nakada, S. (2005). Experimental petrology of the 1991-1995 Unzen dacite, Japan. Part 1: Phase relations, phase composition, and pre-eruptive conditions. *Petrology, 46*(2), 319-337.

Hoshizumi, H., Uto, K., & Watanabe, K. (1999). Geology and eruptive history of Unzen volcano, Shimabara Peninsula, Kyushu, SW Japan. *Journal of Volcanology and Geothermal Research, 89,* 81-94. (1), 89-112.

Hoskin, P., and Schaltegger, U. (2003). The composition of zircon and igneous and metamorphic petrogenesis. *Reviews in Mineralogy and Geochemistry, 53*, 28-61.

Huber, C., Bachmann, O., & Manga, M. (2010). Two competing effects of volatiles on heat transfer in crystal-rich magmas: Thermal insulation vs. defrosting. *Petrology*, *51*(4), 847-867.

* Ishihara, K. (1993). Continuous magma supply inferred from discharge rate of magma and ground deformation rate at Mt. Unzen, Japan. *Annals of the Disaster Prevention Research Institute, Kyoto University, 36*, 219–230.

Jain J.C., Neal C.R., Hanchar J.M. (2001). Problems associated with the determination of rare earth elements of a “gem” quality zircon by inductively coupled plasma-mass spectrometry. *Geostand News: J Geostand Geoanal, 25*, 229-237.

Johnson, C.M., Czamanske, G.K., Lipman, P.W. (1989). Geochemistry of intrusive rocks associated with the Latir volcanic field, New Mexico, and contrasts between evolution of plutonic and volcanic rocks. *Contrib Mineral Petrol, 103,* 241-264.

Kent, A. J. R. (2008). Melt Inclusions in Basaltic and Related Volcanic Rocks. *Minerals, Inclusions and Volcanic Processes, 69,* 273-331.

Kent, A. J. R., Darr, C., Koleszar, A. M., Salisbury, M. J., & Cooper, K. M. (2010). Preferential eruption of andesitic magmas through recharge filtering. Nature Geoscience, 3(9), 631-636.

Kirkland, C.L., Smities, R.H., Taylor, R.J.M., Evans, N., McDonald, B. (2015) Th/U ratios in magmatic environs. *Lithos, 212-215,* 97-414.

Klemetti EW, Clynne MA (2014) Localized Rejuvenation of a Crystal Mush Recorded in Zircon Temporal and Compositional Variation at the Lassen Volcanic Center, Northern California. *PLoS ONE 9*(12): e113157. doi:10.1371/journal.pone.0113157

Kohno, Y., Matsushima, T., & Shimizu, H. (2008). Pressure sources beneath Unzen Volcnao inferred from leveling and GPS data. *Journal of Volcanology and Geothermal Research, 175*, 100-109.

Koleszar, A. M., Kent, A. J. R., Wallace, P. J., & Scott, W. E. (2012). Controls on long-term low explosivity at andesitic arc volcanoes: Insights from Mount Hood, Oregon. *Journal of Volcanology and Geothermal Research*, *219*, 1-14.

Koppers, A. (2002) ArArCALC—Software for $^{40}Ar/^{39}Ar$ age calculations. *Comput. Geosci., 28,* 605–619. Available at [http://earthref.org/tools/ararcalc.htm]

Koppers, A., Staudigel H., Wijbrans J. R., Pringle M. (2003). Short-lived and discontinuous intraplate volcanism in the South Pacific: Hot spots or extensional volcanism?. *Geochem. Geophys. Geosyst., 4.*

Kuiper K. F., Deino A., Hilgen F. J., Krijgsman W., Renne P. R., Wijbrans J. R. (2008). Synchronizing Rock Clocks of Earth History. *Science, 320*, 500.

Mahood, G., Hildreth, W. (1983). Large partition coefficients for trace elements in high silica rhyolites. *Geochimica et Cosmochimica Acta, 47*, 11-30

Marsh, B.D. (1981). On the crystallinity, probability of occurrence, and rheology of lava and magmas. *Contributions to Mineralogy and Petrology* (78)1, 85-98.

Marsh, B.D. (1988). Crystal capture, sorting and retention in convecting magma. *Geological Society of America Bulletin, 100*(11), 1720-1737.

Marsh, B.D. (1996) Solidification fronts and magmatic evolution. *Mineralogical Magazine, 60,* 5-40.

Marsh, B. (2000). Magma chambers. *Encyclopedia of Volcanoes*, 191-206.

McDonough W.F., Sun, S.S. (1995). The composition of the Earth. *Chem Geol, 120*, 223-253.

Miles, A.J., Graham, C.M., Hawkeswoth, C.J., Gillespie, M.R., Hinton, R.W. (2013). Evidence for distinct stages of magma history recorded by the compositions of accessory apatite and zircon. *Contrib Mineral Petrol, 166,* 1-19.

Miller, T., Chertkoff, D., Eichelberger, J., & Coombs, M. (1999). Mt. Dutton volcano, Alaska: Aleutian arc analog to Unzen volcano, Japan*. Journal of Volcanology and Geothermal Research, 89,* 275-301.

Miller, J.S., Wooden, Matzel, J.E.P., Miller, C.F., Burgess, S.D., Miller, R.B. (2007). Zircon growth and recycling during the assembly of large, composite arc plutons. *J Volcanol Geotherm Res, 167,* 282-299.

Miller, C.F., Miller, J.S. (2002). Contrasting stratified plutons exposed in tilt blocks, Eldorado Mountains, Colorado River Rift, NV, USA. *Lithos, 61,*209-224.

Miller, D.S., Smith, R.B. (1999). P and S velocity structure of the Yellowstone volcanic field from local earthquake and controlled-source tomography. *Geophysical Research, 104*(B7), 15105-15121.

Min, K., Mundil R., Renne P. R., Ludwig K. R. (2003). A test for systematic errors in $^{40}Ar/^{39}Ar$ geochronology through comparison with U/Pb analysis of a 1.1-Ga rhyolite. *Geochim. Cosmochim. Acta, 64*, 73–98.

Mueller, S., Llewellin, E. W., & Mader, H. M. (2011). The effect of particle shape on suspension viscosity and implications for magmatic flows. *Geophysical Research Letters, 38.*

Murphy, M. D., Sparks, R. S. J., Barclay, J., Carroll, M. R., & Brewer, T. S. (2000). Remobilization of andesite magma by intrusion of mafic magma at the Soufriere Hills Volcano, Montserrat, West Indies. *Journal of Petrology*, *41*(1), 21-42.

* Nakada, S. and Kamata, H. (1988). Petrogenetical relationship of basalts and andesites in southern part of the Shimabara Peninsula, Kyushu, Japan. *J. Volcanol. Soc. Jpn. 33*, 273–289.

Nakada, S., & Motomura, Y. (1999). Petrology of the 1991-1995 eruption at Unzen: effusion pulsation and groundmass crystallization. *Journal of Volcanology and Geothermal Research*, *89*, 173-196.

Nakada, S., Shimizu, H., & Ohta, K. (1999). Overview of the 1990-1995 eruption at Unzen Volcano. *Journal of Volcanology and Geothermal Research, 89*(1-4), 1-22.

Nakamura, M. (1995). Continuous mixing of crystal mush and replenished magma in the ongoing Unzen eruption*. Geology, 23*(9), 807-810.

Nishimura, K., Kawamoto, T., Kobayashi, T., Sugimoto, T., & Yamashita, S. (2005). Melt inclusion analysis of the Unzen 1991-1995 dacite: implications for crystallization processes of dacite magma . *Bulletin of Volcanology*, *67*, 648-662.

Ohta, K., 1997. Reviews on the prediction of the 1990–1995 eruption of Unzen Volcano and supporting system for risk management. *Bull. Volcanol. Soc. Jpn*. *42*, 61–74.

* Ono, K., Watanabe, K., Itaya, T., Hori, S., Hoshizumi, H., Hayashi, H., Otsudsuki, H. (1992) Geology and K-Ar age of Unzen volcano (preliminary report). *Prog. Abstr., Volcanol, Soc. Jpn., 2* (1).

* Otsuka, H., Furukawa, H. (1988). Early and Middle Pleistocene stratigraphy in Kyushu, Japan. *Mem. Geol. Soc. Jpn. 30,* 155–168.

Paces, J.B., Miller, J.D. (1993). Precise U–Pb ages of Duluth Complex and related mafic intrusions, northeastern Minnesota; geochronological insights to physical, petrogenetic, paleomagnetic, and tectonomagnetic processes associated with the 1.1 Ga Midcontinent Rift System. *Journal of Geophysical Research, 98,* 13997–14013.

Pallister, J. S., Hoblitt, R. P., & Reyes, A. G. (1992). A basalt trigger for the 1991 eruptions of Pinatubo Volcano. *Nature, 356*(6368), 426-428.

Press, W.H., Flannery, B.P., Teukolsky, S.A., Vetterling, W.T. (1988). Numerical Recipes in *C: the Art of Scientific Computing*. Cambridge University Press, New York.

Reid M. R. and Coath C. D. (2000) In situ U-Pb ages of zircons from the Bishop Tuff; no evidence for long crystal residence times. *Geology, 28*, 443–446.

Reid M. R., Coath C. D., Harrison T. M., and McKeegan K. D. (1997) Prolonged residence times for the youngest rhyolites associated with Long Valley Caldera; 230Th-238U ion microprobe dating of young zircons. *Earth Planet. Sci. Lett. 150*, 27–39.

Reid, M.R., Vazquez, J.A., Schmitt, A.K. (2011). Zircon-scale insights into the history of a supervolcano, Bishop Tuff, Long Valley, California, with implications for the Ti-in-zircon geothermometer. *Contrib Mineral Petrol, 161,* 293-311.

Reubi, O., Blundy, J. (2009). A dearth of intermediate melts at subduction zone volcanoes and the petrogenesis of arc andesites. *Nature Lett. 461*, 1269-1273.

Sano Y., Terada K., Fukuoka T. (2002). High mass resolution ion microprobe analysis of rare earth elements in silicate glass, apatite and zircon: lack of matrix dependency. *Chem Geol, 184*, 217-230.

Schmitt, A. K., Grove, M., Harrison, T. M., Lovera, O., Hulen, J., & Walters, M. (2003). The Geysers – Cobb Mountain Magma System, California (Part 1): U-Pb zircon ages of volcanic rocks, conditions of zircon crystallization and magma residence times. *Geochimica et Cosmochimica Acta, 67*(18), 3423-3442.

Schmitt, A.K., Stockli, D.F., Hausback, B.P. (2006). Eruption and crystallization ages of Las Tres Virgenes (Baja California) constrained by combined $^{230Th}/^{238}U$ and (U-Th)/He dating of zircon. *Volcanology, 158,* 281-295.

Schmitt, A.K., Stockli, D.F., Lindsay, J.M., Robertson, R., Lovera, O.M., Kislitsyn, R. (2010). Episodic growth and homogenization of plutonic roots in arc volcanoes from combined U-Th and (U-Th)/He zircon dating. *Earth and Planetary Science Letters, 295,* 91-103.

Simon, J., Reid, M. (2005). The pace of rhyolitic differentiation and storage in an 'archetypical' silicic magma system, Long Valley, California. *Earth Planet Sci Letter, 235,* 123-140.

Simon, J., Renne, P., & Mundil, R. (2008). Implications of pre-eruptive magmatic histories of zircons for U–Pb geochronology of silicic extrusions. *Earth and Planetary Science Letters, 266,* 182-194.

Sparks, R. (1997). Causes and consequences of pressurisation in lava dome eruptions. *Geology*, *150*(3-4), 1089-1092.

Speer, J.A. (1982) Zircon. *Rev Mineral, 5 (2nd edn),* 67-112.

Spera, F. (2000). Physical properties of magma. *Encyclopedia of Volcanoes*, 171-190.

Sugimoto, T., Ishibashi, H., Wakamatsu, S., & Yanagi, T. (2005). Petrologic evolution of Pre-Unzen and Unzen magma chambers beneath the Shimabara Peninsula, Kyushu, Japan: Evidence from petrography and bulk rock chemistry. *Geochemical Journal, 39*, 241-256.

Steiger, R. H., Jäger E. (1977). Subcommission on geochronology: Convention on the use of decay constant in geo- and cosmochronology. *Earth Planet. Sci. Lett., 36,* 359–362.

Storm, S., Shane, P., Schmitt, A.K., Lindsay, J.M. (2011). Contrasting punctuated zircon growth in two syn-erupted rhyolite magmas from Tarawera volcano: Insights to crystal diversity in magmatic systems. *Earth and Planetary Sci Letters, 301,* 511-520.

Taylor, J. R. (1997) An Introduction to Error Analysis: The Study of Uncertainties in Physical Measurements, 327 pp., Univ. Sci. Books, Mill Valley, Calif.

Tepley, F., de Silva, S., Salas, G. (2013). Magma dynamics and petrological evolution leading to the VEI 5 2000 BP eruption of El Misti Volcano, Southern Peru. *Petrology, 0*(0), 1-33.

Tomiya, A., Miyagi, I., Saito, G., Geshi, N. (2013). Short time scales of magma-mixing processes prior to the 2011 eruption of the Shinmoedake volcano, Kirishima volcanic group, Japan. *Bull Volcan, 75*, 750-769.

Tierney, C. (2011). *Timescales of Large Silicic Magma Systems: Implications from Accessory Minerals in Pleistocene Lavas of the Altiplano-Puna Volcanic Complex, Central Andes.* Masters' Thesis. Oregon State University, 2011.

Umakoshi, K., Shimizu, H., & Matsuwo, N. (2001). Volcano-tectonic seismicity at Unzen Volcano, Japan, 1985-1999. *Journal of Volcanology and Geothermal Research, 112,* 117-131.

* Uto, K., Hoang, N., Oguri, K., Hoshizumi, H. and Uchiumi, S. (2002) Volcanic history and magma evolution in the Shimabara Peninsula. *Chikyu Monthly 24*(12), 835–842.

Vavra G (1990) On the kinematics of zircon growth and its petrogenetic significance: a cathodoluminescence study. *Contrib Mineral Petrol 106*, 90-99.

Vazquez J. A. and Reid M. R. (2002) Time scales of magma storage and differentiation of voluminous high-silica rhyolites at Yellowstone caldera, Wyoming. *Contrib. Mineral. Petrol. 144,* 274–285.

Venezky, D., & Rutherford, M. (1999). Petrology and Fe–Ti oxide reequilibration of the 1991 Mount Unzen mixed magma. *Journal of Volcanology and Geothermal Research, 89*, 213-230.

Walker, B., Grunder, A., Wooden, J. (2010). Organization and thermal maturation of long-lived arc systems: Evidence from zircons at the Aucanquilcha volcanic cluster, northern Chile. *Geology, 38*(11), 1007-1010.

Wang, X. Griffin, W.L., O'Reilly, S.Y., Wuxian, L. (2007). Three stages of zircon growth in magmatic rocks from the Pingtan Complex, eastern China. *Acta Geologica Sinica (Eng. Edn), 81,* 68-80.

Wang, X. Griffin, W.L., Chen, J., Huang, P., Li, X. (2011). U and Th contents and Th/U ratios of zircon in felsic and mafic magmatic rocks: improved zircon-melt distribution coefficients. *Acta Geologica Sinica, 85,* 164-174.

Watson, E.B. (1996). Dissolution, growth, and survival of zircons during crustal fusion: kinetic principals, geological models and implications for isotopic inheritance. *Transactions of the Royal Society of Edinburgh Earth Sciences,* 43-56.

Watson E. B., Cherniak D. J., Hanchar J. M., Harrison T. M., and Wark D. A. (1997) The incorporation of Pb into zircon. *Chem. Geol. 141*, 19–31.

Watson, E.B., Harrison, T.M. (1983). Zircon saturation revisited: temperature and composition effects in a variety of crustal magma types. *Earth and Planetary Science Letters, 64*, 295-304.

Watson, E.B., Harrison, T.M. (2005). Zircon thermometer reveals minimum melting conditions on earliest Earth. *Science, 308*(5723), 841-844.

Watts, R.B., de Silva, S.L., Jimenez de Rios, G., Croudace, I. (1999). Effusive eruption of viscous magma triggered and driven by recharge: a case study of the Cerro Chascon-Runto Jarita Dome Complex in southwest Bolivia. *Bull Volcanol, 60,* 241-264.

Wickham, S.M. (1987). The segregation and emplacement of granitic magmas. *Journal of the Geological Society London, 144,* 281-297.

Wiedenbeck, M., Allé, P., Corfu, F., Griffin, W.L., Meier, M., Oberli, F., Von Quadt, A., Roddick, J.C., Spiegel, W. (1995). Three natural zircon standards for U–Th–Pb, Lu–Hf, trace element and REE analyses. *Geostandards Newsletter, 91*, 1–23.

Winter, J. (2010). Subduction-related igneous activity, Parts I and II. In *Principles of igneous and metamorphic petrology* (2nd ed.). New York: Prentice Hall.

Xu, S., Hoshizumi, H., Uto, K., & Freeman, S. (2013). Radiocarbon dating of Fugendake volcano in Unzen, SW Japan. *Radiocarbon, 55*(2-3), 1850-1861.

* Yamagata T., Takashima, I., Watanabe, K., Izawa, E. (2004). TL dating of a new lava dome in Unzen volcano – activities history restoration toward the younger lava dome than 20,000 years. *Bullentin of the Volcanological Society of Japan, 49,* 73-81.

* Yokoyama, T., Ohtsuka, H., Takemura, K., Hayashida, A. (1982). K–Ar ages of volcanic rocks from the Kuchinotsu Group in Kyushu, Japan*. Tsukumo Earth Sci., Inst. Earth Sci. Kyoto Univ. 16*, 28-31.

York, D. (1969) Least squares fitting of a straight line with correlated errors. *Earth Planet. Sci. Lett., 5,* 320–324.

APPENDICES

Appendix A: Detailed sample descriptions

Iwagamiyama (岩上山); UNZ14017

32˚45.686 N

130˚ 19.610 E

Elevation: 390 m

Dating: 440±240 ka (K-Ar); 335±61 ka (K-Ar); 213±18 ka (Ar-Ar)

The Iwagamiyama lava is located downslope of the eastern flank of the most recent eruption. It is on north of the Mizunashi River, bounded by two valleys to the north and south that were channels for the most recent eruption's pyroclastic flows. To the west and upslope is the Inaoyama dome. The eruption age for this dome is uncertain; ages include 440 ±240 ka and 335±61 ka (unpublished internal AIST report 2002; K-Ar) and 213±18 ka (unpublished internal AIST report; Ar-Ar on plagioclase). It is considered part a flow of the Older Unzen volcanics (500-200 ka). The sample was collected directly from the outcrop, on the north facing side. It is a crystal-rich vesicular dacite, containing phenocrysts of plagioclase > hornblende ≈ biotite.

Minamisenbongi (南千本木); UNZ14008

32˚46.611 N

130˚ 19.295 E

Elevation: 369 m

Dating: 187±53 (K-Ar); 185±7 (K-Ar)

This lava is an undifferentiated unit, considered part of the Older Unzen group (500-200 ka). It is located south of the village of Senbongi, which was destroyed by pyroclastic flows during the most recent eruption. The sample name, "Minami-senbongi", was given when collected; Hoshizumi et al. 1999 sampled within this undifferentiated unit to the north, naming the sample "Tarukidaichi NW". This unit is located east of the Senbongi lava, which was erupted 13±4 ka (Xu et al., 2013). Hoshizumi et al. (1999) dated their sample at 187±53 ka through K-Ar dating, and an unpublished K-Ar age from the AIST 2002 internal near our sampling location is 185±7 ka. The sample is a moderately crystal-rich andesite or dacite, with plagioclase >> hornblende (likely replaced with Fe-Ti oxides).

Botanyama (ボタン山); UNZ14013

32˚44.646 N

130˚ 18.986 E

Elevation: 448 m

Dating: 23±4 ka (Ar-Ar)

Botanyama is a lava located southeast of the most recent eruption's dome. It is a flow of the Younger Unzen volcanics (100 ka –present). It has been dated through Ar-Ar on plagioclase to be 23±4 ka (unpublished internal AIST report 2002). The sample was collected from the peak of Botanyama, off-trail from the Kamionokobanitatoge Mountain Trail (上大野木場仁田峠線登山遊歩道). The sample is a crystal-rich dacite, with plagioclase > hornblende ≈ biotite.

Taruki-higashi (垂木東); UNZ14016

32˚45.715 N

130˚ 19.725 E

Elevation: 441 m

Dating: 35±8 ka (Ar-Ar); 25±12 ka (K-Ar)

The Taruki-higashi lava is located downslope on the western flank of Mayuyama volcano. It is a part of the Younger Unzen volcanics and possibly represents the oldest activity of Fugendake (Hoshizumi et al., 1999). The lava has been dated at 25±12 (Hoshizumi et al., 1999; K-Ar) and 35±8 ka (unpublished internal AIST report 2002; Ar-Ar on plagioclase). The sample was collected off the Highway 207. It is a crystal-rich dacite, with plagioclase > hornblende >> biotite.

Nodake (野岳); UNZ14029

32.7450˚ N

130.28543˚ E

Elevation: 1103 m

Dating: 73±4 ka (K-Ar); 100±7 ka (K-Ar); 112±6 (K-Ar);230±30 (K-Ar)

The Nodake dome is the oldest center of Younger Unzen volcanics; there is no stratigraphic relationship to Myoken or Fugen domes. Eruptions from this center are thought to range in age from 73-112 ka (Hoshizumi et al., 1999; K-Ar); an earlier study published a K-Ar date of 230±30 ka (Ono et al., 1992). The sample was collected from the dome center, off from the main trail. It is a vesicular, moderately crystal-rich andesite to dacite, bearing plagioclase >> hornblende.

Fugendake (普賢岳); UNZ14033

32.759940˚ N

130.29214˚ E

Elevation: 1355 m

Dating: 3.1±0.6 (TL); 3.4±0.6 (TL); 6±2 ka (zircon fission track)

Fugendake developed inside the scar of Myokendake. Eruptions from this dome are thought to span from about 25 ka to historical times; it is the currently active volcanic center of Unzen, where the most recent eruption occurred (Hoshizumi et al., 1999). The sample was collected from the summit of Fugendake, which is a composite lava dome of andesite to dacite. Summit dates include two thermoluminescence dates, 3.1 ka and 3.4 ka (Yamagata et al., 2004), and a zircon fission-track age of 6 ka. The sample is a crystal-rich dacite, bearing plagioclase > hornblende >>biotite.

Heisei-shinzan (平成新山); UNZ14032 and UNZ13001

32.76083˚ N

130.29820˚ E

Elevation: 1449 m

Dating: 1990-1995 (historical)

Heisei-shinzan is the most recent dome of Unzen, formed during the 1990-1995 eruption. This eruption began in the scar of Fugendake volcano and is considered a continuation of activity at the Fugendake center. With permission from local authorities, two samples were collected from the dome summit area, which is currently off-limits due to continued hazards: the first in July 2013 (“Unzen”), and the second (“UNZ14032”) in August 2014. GPS coordinates indicate the location of the second sampling, although both samples are

considered to be the same age. The same is a crystal-rich dacite, bearing plagioclase > hornblende ≈ biotite.

Tenguyama (天狗山); UNZ14023 and UNZ13002

32.76341˚ N

130.33591˚ E

Elevation: 593 m

Dating: 3.0±1.0 ka (TL); 4.1±0.8 ka (TL); 1792 (historical debris avalanche)

Tenguyama is one of two lava domes within Mayuyama volcano (the other being Shichimenzan), which is stratigraphic ally separated from Fugendake and Nodake. It is part of the Younger Unzen volcanics. In 1792, a sector of Tenguyama volcano collapsed in a debris avalanche; it is thought to have been triggered by volcano-tectonic earthquakes related to the eruption of the Shinyake lava from the Fugendake center (Hoshizumi et al., 1999). Two samples were collected of this dome: the first in July 2013, which is a block from the most 1792 debris avalanche ("Mayuyama/1792 DA"), and the second from the western flank of the Tenguyama dome (UNZ14023). GPS coordinates indicate the location of the Tenguyama dome sample; no GPS coordinates are available for the "Mayuyama/1792 DA" sample, which was collected from a block within Shimabara City, east of the dome. The "Mayuyama" sample was analyzed for preliminary zircon geochronology at the ULCA SIMS.

Myoken-dake (妙見岳); UNZ14030

32.75651˚ N

130.28568˚ E

Elevation: 1324 m

Dating: 20-30 ka (K-Ar)

The Myoken-dake volcano is composed primarily of the main edifice, within which sits Fugen-dake and Heisei-shinzan, and several pyroclastic flow and debris avalanche deposits. The main edifice has a "horseshoe" shaped scar that opens to the east. There are two main andesite flows within the edifice, which are interpreted as dissected lava domes. K-Ar ages obtained on the edifice range in age from 20-30 ka (Hoshizumi et al., 1999). One sample was collected from the west-side of the main edifice, up-trail from the Myoken shrine.

Kusenbudake (九千部岳); UNZ14028

32.77392˚ N

130.26328˚ E

Elevation: 995 m

Dating: 200 ± 10 ka (K-Ar)

Kusenbudake dome is located northwest of the most recently erupted dome, and it is considered a part of the Older Unzen period. Faults trending to the east-west have dissected the deposits, and the sampled dome has subsided about 200 m within the Unzen graben (Hoshizumi et al., 1999). The eruption age is thought to be approximately 200 ka, according to K-Ar dating (Watanabe et al., 1993). Azumadake and Torikabutoyama, to the north, are likely dissected remnants of Kusenbudake (field notes). The sample was collected from the Kusenbudake summit.

Yadake (矢岳); UNZ14026

32.74117˚ N

130.26954˚ E

Elevation: 824 m

Dating: 240 ± 10 ka (K-Ar)

Yadake dome is located southwest of the most recent dome. It is consider a part of the Older Unzen period. The dome potentially has a scar opening to the west, although overgrowth and erosion make it difficult to interpret. The dome is located within the town of Unzen Onsen and accessible by trail from the town center. The eruption age is thought to be 240 ka, according to K-Ar dating (Watanabe et al., 1993).

Sarubayama (猿葉山); UNZ14005

32.77063˚ N

130.19876˚ E

Elevation: 376 m

Dating: 260 ± 20 ka (K-Ar)

Sarubayama dome is the most westward located volcano of the complex. It is considered a part of the Older Unzen period. The dome appears to be stratigraphically separate from adjacent domes. The eruption age is thought to be approximately 260 ka, according to K-Ar dating (Watanabe et al., 1993). The sample was collected from the summit, off-trail from the hand-gliding station.

Appendix B: Thin section descriptions

Iwagamiyama (UNZ14017)

Phenocrysts (45%)

Plagioclase (24%): Range in size seriate, from groundmass to approximately 15 mm (hand-sample). There are clearly distinct populations, as crystals vary in morphology and texture. Crystals morphologies include: 1) euhedral with sharp edges (typically large to medium-sized crystals); 2) dusty-edged subhedral (typically medium-sized); 3) to few rounded grains (typically small to medium-sized); 4) glomerocrysts up to 1.5 cm incorporating a variety of sizes and textures. Textures include: 1) inclusion-free, oscillatory zoned crystals (typically medium-large, euhedral crystals); 2) inclusion-rich (Fe-Ti oxides, hornblende, zircon, others), mottled-core crystals (typically medium-large, euhedral to subhedral crystals, often in glomerocrysts); and 3) oscillatory-zoned crystals with thick sieve zones or inclusion-rich zones (typically medium-small subhedral to rounded crystals).

Hornblende (7%): Range in size seriate, from groundmass to approximately 10 mm (hand-sample); primarily 1-10 mm. Black to dark reddish brown in hand-sample; pleochroic from yellow-green to orange to reddish brown. Crystals are typically euhedral with sharp edges; often in contact with plagioclase. Inclusion-rich, including Fe-Ti oxides, biotite, plagioclase, zircon and apatite (?). No resorption rims seen in thin section.

Biotite (7%): Range in size seriate, from groundmass to approximately 5 mm (hand-sample); typically 0.5-2.5mm. Black to dark brown in hand-sample; pleochroic from yellow to orange to reddish brown. Crystals euhedral to subhedral. Inclusion-rich, primarily Fe-Ti oxides, zircon and plagioclase. Majority of grains have a thick reaction rim (0.1-0.2 mm) of fine-grained biotite and Fe-Ti oxides.

Quartz (3%): Range in size from 0.5-2 mm. Gray to clear in hand-sample. Crystals are all rounded and often embayed, few with broken edges and dusty edges.

Orthopyroxene (1%): Typically 1 mm or less. Rare euhedral phenocrysts present, pleochroic from yellow to light yellow, often showing perfect 90˚ cleavage and low birefringence (up to 1st order yellow). Crystals are inclusion-free and isolated in matrix.

Fe-Ti oxides: Ubiquitous crystals ranging in size from groundmass up to 1 mm. Crystals are euhedral to anhedral or rounded. Primarily groundmass component, but a common inclusion of hornblende and biotite.

Clinopyroxene (1%): Groundmass component only. Crystals appear rounded and are light yellow in plain light, showing no pleochroism. Typically twinned. It appears as isolated crystals within the groundmass.

Olivine (T?): Possibly trace amounts of isolated olivine present in groundmass. Crystals are clear in plain light and show second to third order birefringence under cross-polars.

Zircon (T): Often found as euhedral to subhedral, doubly-terminated inclusions within hornblende, biotite and (less commonly) plagioclase. Possibly present, but not observed, in groundmass.

Groundmass (55%)

The groundmass is devitrified and approximately 40-50% microlites of acicular plagioclase, with lesser amounts of hornblende, biotite, clinopyroxene, olivine (?), and zircon (?).

Minami-senbongi (UNZ14008)

Phenocrysts (40%):

Plagioclase (20%): Fairly continuous size range from groundmass to 8 mm (hand-sample), with phenocrysts typically 3-6 mm. Crystals range from euhedral to anhedral to rounded; many have broken or dusty edges. Crystals are usually isolated, with glomerocrysts of plagioclase crystals, and few glomerocrysts of plagioclase with hornblende or biotite. Multiple populations of crystals is evident. Textures vary considerably: 1) oscillatory zoned euhedral crystals (medium-large sized) occurring as isolated grains or in plagioclase glomerocrysts; 2) thick (0.1-0.2 mm) dusty rimmed grains (size varies; few with a thin clear rim after thick dusty zone) occurring as isolated grains; 3) few crystals with fine-grained "feathery" interiors; interiors have low birefringence and are a mixture of colorless and opaque in PPL; 4) rare, entirely resorbed crystals identifiably in groundmass by euhedral to subhedral outlines.

Hornblende (10%): Sizes range from 0.5 – 5 mm. Crystals are typically euhedral to subhedral. Grains are almost entirely opaque, likely oxidized or replaced. Modal abundance is difficult to determine, as biotite phenocrysts are also often opaque. Interiors occasionally

have fine grained, cryptocrystalline portions; few have identifiable inclusions of pyroxene and plagioclase. Grains occur as isolated phenocrysts.

Biotite (5%): Size range from 0.2 – 1 mm. Crystals are typically euhedral to subhedral, isolated grains. Almost all grains have been oxidized or replaced by cryptocrystalline (possibly pyroxene and plagioclase) masses.

Quartz (T): Occurs as rare, isolated grains up to 0.4 mm that are rounded, embayed and often fractured.

Clinopyroxene (3%): Sizes range from groundmass to 0.4 mm. Light yellow in PPL; twinned in XPL. Crystals typically euhedral to subhedral (few appear rounded). Commonly have thick, black rims. Occur as isolated crystals in groundmass, and occasionally as inclusions (hornblende and plagioclase) or replacement minerals (biotite).

Orthopyroxene (T*): Occurs as isolated grains in the groundmass, up to 0.3 mm. Colorless to yellow in PPL. Euhedral, hexagonal crystals, occasionally with thin black rims.

Olivine (T*): Few fine-grained grains in groundmass, <0.1 mm. Colorless in PPL; 2nd-3rd order birefringence.

Fe-Ti oxides (2%): Ubiquitous subhedral to anhedral grains, ranging from groundmass up to 0.2mm. Often embayed, showing some resorption textures.

Zircon (T): Not observed in thin section, but collected during mineral separation.

Groundmass (60%):

Devitrified glass with abundant, altered microlites of acicular plagioclase crystals, with less amounts of pyroxenes and few olivine crystals. Approximately 10% vesicles.

Fugen-dake (UNZ14033)

Phenocrysts (40%):

Plagioclase (23%): Sizes range from groundmass up to 9 mm (hand-sample). Multiple populations exist: 1) large phenocrysts with oscillatory zoning and edges that are rounded and dusty, but appear to have originally been euhedral; 2) large to medium phenocrysts with subhedral edges that have complex zoning of inclusions and sieved-textures; 3) groundmass microlites that range from acicular to euhedral with no zoning; 4) groundmass microlites that appear skeletal.

Hornblende (7%): Occurs in two populations, as large phenocrysts (1-3 mm) and as groundmass microlites (< 1 mm). Phenocrysts are euhedral to subhedral, with thick black rims and occasionally interiors that are fine-grained or contain plagioclase crystals (up to 0.2 mm). Groundmass grains are euhedral to anhedral, occasionally rounded and embayed. All have thin, black rims and many interiors include rounded plagioclase crystals. Few occur as masses attached to plagioclase phenocrysts (up to 0.6 mm).

Biotite (7%): Occurs in two populations, as large phenocrysts (2-5 mm), and groundmass up to 1 mm crystals. Large phenocrysts are euhedral to subhedral, showing a variety of resorption textures such as replacement rims or mantling by plagioclase and thick, black rims; occasionally entire crystals are opaque. Groundmass and small phenocrysts (up to approximately 1 mm) are euhedral to subhedral, commonly with thin black rims.

Quartz (T): Few, rounded and embayed isolated grains up to 3.5 mm. Rarely occurs as fractured crystals, with a combination of rounded, dusty and sharp edges.

Clinopyroxene (2%): Groundmass component up to 0.4 mm. Light yellow in PPL; twinned in XPL. Crystals typically subhedral to anhedral or rounded. Occasionally occurs in small masses with 2-4 other pyroxene crystals.

Orthopyroxene (1%): Groundmass component typically 0.2 mm or less. Occurs as euhedral to subhedral crystals, rarely embayed, occasionally in small masses with 2-4 other pyroxene crystals. Clear to light yellow in PPL. Typically has thin, black rim.

Fe-Ti oxides (2%): Groundmass component up to 0.5 mm. Crystals typically anhedral, rounded or embayed.

Zircon (T): Occurs as inclusions in biotite and hornblende; not observed in groundmass.

Groundmass (58%):

The groundmass is devitrified and primarily contains microlites of plagioclase, with lesser amounts of hornblende, biotite and pyroxenes. Vesicles account for 10-15% of sample volume.

Nodake (UNZ14029)

Phenocryst(38%)

Plagioclase (15%): Ranges in size from groundmass to 6 mm, with sizes concentrated between large phenocrysts (4-6 mm), medium phenocrysts (1-2.5 mm), and groundmass

(<1 mm). Large and medium phenocrysts are typically subhedral to anhedral to rounded; few are euhedral. Occur primarily as isolated phenocrysts, with few as glomerocrysts with 3-4 other plagioclase grains. Most large phenocrysts are oscillatory zoned, with several zones that are inclusion/sieve-rich. Medium-sized grains are often rounded or have dusty edges. Phenocrysts of all sizes commonly have dusty or feathery fine-grained cores or thick interior zones. Few medium-sized grains are euhedral and with typical oscillatory zoning; few are euhedral with no apparent zonation. Groundmass crystals are unusually euhedral and rectangular.

Hornblende (8%): Discontinuous sizes: large phenocrysts (2-5 mm), and groundmass to 1 mm. Large phenocrysts are typically euhedral to subhedral; all show resorption textures, including thick black rims (most grains are entirely black), replacement mineralization (pyroxenes and plagioclase), and few with fractures. Groundmass to small phenocrysts are euhedral to subhedral, with thick black rims. Most occur as isolated crystals, with few occurring as glomerocrysts with 3-5 anhedral to subhedral pyroxene and olivine grains.

Biotite (7%): Discontinuous sizes: large phenocrysts (2-4 mm), and groundmass up to 0.9 mm. Large phenocrysts are typically euhedral to subhedral, most showing resorption characteristics such as thick black rims and replacement by plagioclase. Groundmass grains euhedral to subhedral, and have acicular shapes; most have thick black rims.

Quartz (T): Few crystals up to 1.2 mm. All occur as isolated grains that are rounded and embayed.

Orthopyroxene (2%): Sizes are less than 1 mm. Crystals are euhedral to anhedral, occurring as replacement minerals in hornblende, within glomerocrysts of pyroxenes/olivine/hornblende, and rarely as isolated crystals.

Clinopyroxene (4%): Sizes are less than 1 mm. Crystals are subhedral to anhedral, occurring commonly as isolated grains, replacement minerals in hornblende, and in glomerocrysts of pyroxenes/hornblende/olivine.

Fe-Ti oxides (1%): Groundmass up to 0.7 mm. Crystals are anhedral to rounded, occurring commonly as inclusions or replacements in biotite and hornblende, in glomerocrysts of pyroxenes (and olivine?), and as isolated crystals.

Zircon (T): Not observed in thin section, but collected during mineral separations.

<u>Groundmass (62%):</u>

Primarily devitrified glass, acicular to rectangular plagioclase microlites, and vesicles (15%). Fine-grained psuedomorphs of hornblende and biotite, composed of plagioclase, pyroxenes and rarely olivine, can rarely be observed.

Taruki-higashi (UNZ14016)

Phenocrysts (42%):

Plagioclase (20%): Sizes range from groundmass to 8 mm (hand-sample). Crystals are euhedral to subhedral, often with rounded, broken or dusty edges. Grains occur as isolated crystals and as glomerocrysts with 3-4 plagioclase grains, rarely in glomerocrysts with 2-3 hornblende and plagioclase; often 0.1-0.3 mm grains are found included in hornblende and biotite. Crystals are mostly normal, oscillatory-zoned (occasionally lacking zoning), with few zones of melt or mineral inclusions; few grains have dusty interiors, are highly included or have a think melt-inclusion zone. Multiple populations possibly present, but phenocrysts are relatively uniform compared to other Unzen andesite and dacite samples.

Hornblende (7%): Sizes range from groundmass up to 4 mm (average size is less than 1 mm); distinct size populations <1 mm grains and 2-4 mm phenocrysts. Grains are euhedral to subhedral, rarely rounded. Large phenocrysts (2-4 mm) are often inclusion-rich, typically containing plagioclase and Fe-Ti oxides. Few crystals have opaque rims, or dusty opaque edges. Few small to medium crystals present as glomerocrysts with Fe-Ti oxides and plagioclase.

Biotite (10%): Sizes range from groundmass up to 8 mm (hand-sample). Euhedral crystals, occasionally with one or two broken or dusty edges. Grains less than 2 mm often have curved edges, are wavy, and sometimes “stringy”; vapor phase biotite is evident in some vesicles. Grains are inclusion-rich (plagioclase, quartz, zircon). Rarely, grains contain fine-grained rims or are broken down into fine-grained masses. Grains commonly appear inter-grown with a single plagioclase crystal.

Quartz (T): Rare grains up to 3 mm. Always rounded grains that are highly fractured and contain a broken edge. Rarely included as rounded grains in biotite and hornblende.

Fe-Ti oxides (5%): Groundmass up to 0.8 mm. Grains occur as isolated subhedral to anhedral crystals, as glomerocrysts with hornblende, as inclusions with hornblende and

biotite, and as a groundmass component. Commonly contains opaque (in PPL and reflective light) speckles.

Groundmass (52%):

Devitrified, vesiculated groundmass; vesicles are typical elongate and aligned, suggested a compaction or flow textures. Microlites do not appear aligned. "Stringy" grains of biotite often cut across or along edges of vesicles. Majority of microlites are opaque or altered and unidentifiable.

Botanyama (UNZ14013)

Phenocrysts (40%):

Plagioclase (20%): Sizes range from groundmass up to 7 mm (hand-sample). Crystals are always subhedral to anhedral or rounded (often appear as if formerly euhedral grains). Dusty and/or broken edges are common. Multiple populations of phenocrysts are present, with textures varying from oscillatory-zoned crystals with a thin clear rim and adjacent thick sieve zone, to inclusion-rich cores, to crystals with multiple zones of inclusions. Occur most commonly as isolated grains, with few glomerocrysts of 2-3 plagioclase, and rarely as glomerocrysts with 3-4 hornblende and Fe-Ti oxide grains.

Hornblende (9%): Groundmass up to 6 mm (hand-sample). Euhedral to subhedral phenocryst, often with broken and/or dusty edges. Commonly have a thin, opaque rim. Grains are all inclusion-rich, with Fe-Ti oxides, plagioclase and zircon. Few are present as glomerocrysts with 3-4 other hornblende crystals, with Fe-Ti oxides and plagioclase.

Biotite (6%): Sizes range from 0.2 mm to 2 mm. Euhedral to anhedral grains with broken edges. Grains are often 1) cloudy or opaque, 2) occur as a fine-grained mass, or 3) have a fine-grained rim. Rare "stringy" groundmass biotite can be found. Large phenocrysts sometimes inter-grown with a single plagioclase grain.

Quartz (2%): Up to 2.5 mm grains. All crystals are rounded and embayed, often with broken and/or dusty edges.

Fe-Ti oxides (3%): Up to 0.3 mm. Occurs as subhedral to anhedral isolated grains, inclusions in biotite and hornblende, and occasionally in glomerocrysts with hornblende.

Pyroxenes (T): Crystals are all less than 0.1 mm anhedral grains, colorless in PPL with near 90˚ cleavage; rarely clinopyroxene twinning can be seen in XPL. It is difficult to determine

relative proportions of clinopyroxene and orthopyroxene, given small grain size and a thin section with non-uniform thickness.

Groundmass (60%):

Devitrified groundmass with euhedral plagioclase microlites and Fe-Ti oxides, with few hornblende and biotite micro-phenocrysts. Few vesicles (less than 5%).

Tenguyama (UNZ14023, Matuyama 17, and Matuyama 18)

Phenocrysts (45%):

Plagioclase (15%): Sizes range from 1 – 9 mm (hand-sample), with somewhat discontinuous size range (<1 m and 3 mm +). Crystals are euhedral to subhedral, often with rounded edges and few with dusty edges. Textures vary: 1) mottled cores; 2) mottled zones with a clear core; 3) inclusion-rich interiors (melt, hornblende, etc.); 4) inclusion-rich zones; 5) normal oscillatory zoned with few/no inclusions. Few occur as glomerocrysts with 3-4 plagioclase, or hornblende, biotite and quartz.

Hornblende (10%): Sizes range from 0.4 – 5 mm. Crystals are euhedral to subhedral, few with broken or resorbed edges. Grains are inclusion-rich (zircon, Fe-Ti oxides), and all have a thick opaque rim or fine-grained, Fe-Ti oxide rich rim. Groundmass hornblende (<1 mm) are almost entirely opaque or replaced by Fe-Ti oxides. Few phenocrysts occur as glomerocrysts with quartz and plagioclase.

Biotite (7%): Sizes range from 0.2 – 4 mm. Crystals are euhedral to subhedral, and inclusion-rich (plagioclase, quartz, zircon, Fe-Ti oxides). Often have thick opaque or fine-grained rims. Few glomerocrysts with plagioclase, quartz and hornblende.

Quartz (10%): Sizes range from 0.5 – 5 mm. Occurs primarily as isolated grains that are rounded, embayed and fractured. Occasionally found touching a single hornblende crystal, and as a glomerocrysts with plagioclase, hornblende or biotite.

Fe-Ti oxides (3%): Groundmass up to 0.7 mm. Occurs as isolated crystals, inclusions in hornblende and biotite, and as a replacement or rim in hornblende and biotite. Grains are anhedral to rounded, with few subhedral cubic grains.

Pyroxene (?): Trace amounts of colorless (PPL), 2nd order birefringent mineral. Occurs as rare grains (less than 0.2 mm) almost always included in or touching hornblende crystals, or touching Fe-Ti oxides.

Groundmass (55%):

The groundmass is devitrified and contains few vesicles (less than 5%). Groundmass phases included acicular to euhedral plagioclase, with opaque hornblende and biotite, and Fe-Ti oxides.

Heisei-shinzan (UNZ14032, Unzen 15, and Unzen 16)

Phenocrysts (44%)

Plagioclase (20%): Grains up to 8 mm in hand-sample. Most samples are 2-8mm or less than 1 mm. Larger grains are euhedral to subhedral, often with broken or dusty edges. Textures vary: 1) inclusion-rich interior zone; 2) inclusion-free oscillatory zoned; 3) sieve-rich outer zone followed by a clear rim; 4) mottled core. Grains occur most commonly as isolated phenocrysts, few touching a single grain of plagioclase or hornblende, and rarely as fine grained glomerocrysts (~0.5 mm) with hornblende and biotite.

Hornblende (11%): Grains up to 5 mm, with two populations: 1) 2+ mm, and 2) less than 0.5 mm. Phenocrysts are euhedral to subhedral, occasionally with broken or fine-grained edges. Thin opaque rims are common. Grains are inclusion-rich, including plagioclase, quartz, Fe-Ti oxides and zircon. Typically isolated, few touching a plagioclase grain, and rarely as fine-grained glomerocrysts with plagioclase and biotite.

Biotite (5%): Grains up to 2.5 mm, with most grains 1.5 mm or less. Euhedral to subhedral faces; smaller grains appear acicular. Large phenocrysts are typically altered to fine-grained masses or are entirely opaque. Grains are inclusion-rich, including maining Fe-Ti oxides and plagioclase.

Quartz (7%): Grains up to 5 mm. Crystals are always rounded and embayed, occurring primarily as isolated phenocrysts or included in biotite and hornblende.

Fe-Ti oxides (1%): Grains are typically less than 0.1 mm, although rarely occur as large (0.5 mm) anhedral crystals touching hornblende and biotite.

Groundmass (56%):

Primarily composed of glass, euhedral to acicular plagioclase and vesicles (5-10%). Groundmass also includes microlites of biotite and hornblende.

Appendix C. Correlation coefficients for trace element analysis

LA-ICPMS correlation coefficients:

Pearson Product-Moment Correlation Coefficient	
Independent variable:	Y
Dependent variable:	Nb
r:	0.50315
Fisher's z_r:	0.553516
df:	216
r (two-tailed) 0.05:	0.132
r (two-tailed) 0.01:	0.172
r (one-tailed) 0.05:	0.111
r (one-tailed) 0.01:	0.156
t:	8.55679
df:	216
p (two-tailed):	< 0.001
p (one-tailed):	< 0.001

Spearmans's Rank-Order Correlation Coefficient	
Variable 1:	Y
Variable 2:	Nb
r_S (tie corrected):	0.539632
n:	218
r_S (two-tailed) 0.05:	0.134
r_S (two-tailed) 0.01:	0.174
r_S (one-tailed) 0.05:	0.112
r_S (one-tailed) 0.01:	0.158
t:	9.42027
df:	216
p (two-tailed):	< 0.001
p (one-tailed):	< 0.001
z:	7.94927
p (two-tailed):	< 0.001
p (one-tailed):	< 0.001

Pearson Product-Moment Correlation Coefficient	
Independent variable:	179-Hf*
Dependent variable:	Th/U
r:	0.0229063
Fisher's z_r:	0.0229103
df:	216
r (two-tailed) 0.05:	0.132
r (two-tailed) 0.01:	0.172
r (one-tailed) 0.05:	0.111
r (one-tailed) 0.01:	0.156
t:	0.336741
df:	216
p (two-tailed):	> 0.5
p (one-tailed):	0.368

Spearmans's Rank-Order Correlation Coefficient	
Variable 1:	179-Hf
Variable 2:	Th/U
r_S (tie corrected):	0.187764
n:	218
r_S (two-tailed) 0.05:	0.134
r_S (two-tailed) 0.01:	0.174
r_S (one-tailed) 0.05:	0.112
r_S (one-tailed) 0.01:	0.158
t:	2.80953
df:	216
p (two-tailed):	0.005
p (one-tailed):	0.003
z:	2.76594
p (two-tailed):	0.006
p (one-tailed):	0.003

Pearson Product-Moment Correlation Coefficient	
Independent variable:	179-Hf*
Dependent variable:	Eu/Eu*
r:	0.0108387
Fisher's z_r:	0.0108391
df:	216
r (two-tailed) 0.05:	0.132
r (two-tailed) 0.01:	0.172
r (one-tailed) 0.05:	0.111
r (one-tailed) 0.01:	0.156
t:	0.159305
df:	216
p (two-tailed):	> 0.5
p (one-tailed):	0.437

Spearmans's Rank-Order Correlation Coefficient	
Variable 1:	179-Hf
Variable 2:	Eu
r_S (tie corrected):	-0.135816
n:	218
r_S (two-tailed) 0.05:	0.134
r_S (two-tailed) 0.01:	0.174
r_S (one-tailed) 0.05:	0.112
r_S (one-tailed) 0.01:	0.158
t:	-2.01476
df:	216
p (two-tailed):	0.045
p (one-tailed):	0.023
z:	-2.0007
p (two-tailed):	0.045
p (one-tailed):	0.023

SIMS correlation coefficients:

Pearson Product-Moment Correlation Coefficient	
Independent variable:	Model Age (ka)
Dependent variable:	Ti (ppm)
r:	0.408028
Fisher's z_r:	0.433243
df:	106
r (two-tailed) 0.05:	0.189
r (two-tailed) 0.01:	0.246
r (one-tailed) 0.05:	0.159
r (one-tailed) 0.01:	0.223
t:	4.60136
df:	106
p (two-tailed):	< 0.001
p (one-tailed):	< 0.001

Pearson Product-Moment Correlation Coefficient	
Independent variable:	Model Age (ka)
Dependent variable:	Hf (ppm)
r:	-0.504888
Fisher's z_r:	-0.555845
df:	106
r (two-tailed) 0.05:	0.189
r (two-tailed) 0.01:	0.246
r (one-tailed) 0.05:	0.159
r (one-tailed) 0.01:	0.223
t:	-6.02205
df:	106
p (two-tailed):	< 0.001
p (one-tailed):	< 0.001

Pearson Product-Moment Correlation Coefficient	
Independent variable:	Model Age (ka)
Dependent variable:	Th/U
r:	0.129772
Fisher's z_r:	0.130507
df:	134
r (two-tailed) 0.05:	0.168
r (two-tailed) 0.01:	0.218
r (one-tailed) 0.05:	0.141
r (one-tailed) 0.01:	0.198
t:	1.51503
df:	134
p (two-tailed):	0.132
p (one-tailed):	0.065

Pearson Product-Moment Correlation Coefficient	
Independent variable:	Model Age (ka)
Dependent variable:	Th (ppm)
r:	0.0172732
Fisher's z_r:	0.0172749
df:	134
r (two-tailed) 0.05:	0.168
r (two-tailed) 0.01:	0.218
r (one-tailed) 0.05:	0.141
r (one-tailed) 0.01:	0.198
t:	0.199982
df:	134
p (two-tailed):	> 0.5
p (one-tailed):	0.421

Pearson Product-Moment Correlation Coefficient	
Independent variable:	Model Age (ka)
Dependent variable:	U (ppm)
r:	-0.0436545
Fisher's z_r:	-0.0436823
df:	134
r (two-tailed) 0.05:	0.168
r (two-tailed) 0.01:	0.218
r (one-tailed) 0.05:	0.141
r (one-tailed) 0.01:	0.198
t:	-0.50582
df:	134
p (two-tailed):	> 0.5
p (one-tailed):	0.307

Spearmans's Rank-Order Correlation Coefficient	
Variable 1:	Model Age (ka)
Variable 2:	Ti (ppm)
r_S (tie corrected):	0.429123
n:	108
r_S (two-tailed) 0.05:	0.190
r_S (two-tailed) 0.01:	0.247
r_S (one-tailed) 0.05:	0.160
r_S (one-tailed) 0.01:	0.224
t:	4.89134
df:	106
p (two-tailed):	< 0.001
p (one-tailed):	< 0.001
z (not recommended):	4.43888
p (two-tailed):	< 0.001
p (one-tailed):	< 0.001

Spearmans's Rank-Order Correlation Coefficient	
Variable 1:	Model Age (ka)
Variable 2:	Hf (ppm)
r_S:	-0.525556
n:	108
r_S (two-tailed) 0.05:	0.190
r_S (two-tailed) 0.01:	0.247
r_S (one-tailed) 0.05:	0.160
r_S (one-tailed) 0.01:	0.224
t:	-6.36012
df:	106
p (two-tailed):	< 0.001
p (one-tailed):	< 0.001
z (not recommended):	-5.43639
p (two-tailed):	< 0.001
p (one-tailed):	< 0.001

Spearmans's Rank-Order Correlation Coefficient	
Variable 1:	Model Age (ka)
Variable 2:	Th/U
r_S (tie corrected):	0.19691
n:	136
r_S (two-tailed) 0.05:	0.169
r_S (two-tailed) 0.01:	0.220
r_S (one-tailed) 0.05:	0.142
r_S (one-tailed) 0.01:	0.200
t:	2.32491
df:	134
p (two-tailed):	0.022
p (one-tailed):	0.011
z (not recommended):	2.28789
p (two-tailed):	0.022
p (one-tailed):	0.011

Spearmans's Rank-Order Correlation Coefficient	
Variable 1:	Model Age (ka)
Variable 2:	Th (ppm)
r_S (tie corrected):	0.0135061
n:	136
r_S (two-tailed) 0.05:	0.169
r_S (two-tailed) 0.01:	0.220
r_S (one-tailed) 0.05:	0.142
r_S (one-tailed) 0.01:	0.200
t:	0.156358
df:	134
p (two-tailed):	> 0.5
p (one-tailed):	0.438
z (not recommended):	0.156926
p (two-tailed):	> 0.5
p (one-tailed):	0.438

Spearmans's Rank-Order Correlation Coefficient	
Variable 1:	Model Age (ka)
Variable 2:	U (ppm)
r_S (tie corrected):	-0.141809
n:	136
r_S (two-tailed) 0.05:	0.169
r_S (two-tailed) 0.01:	0.220
r_S (one-tailed) 0.05:	0.142
r_S (one-tailed) 0.01:	0.200
t:	-1.65831
df:	134
p (two-tailed):	0.100
p (one-tailed):	0.050
z (not recommended):	-1.64767
p (two-tailed):	0.099
p (one-tailed):	0.050

Pearson Product-Moment Correlation Coefficient	
Independent variable:	Th/U
Dependent variable:	Gd (ppm)
r:	0.885714
Fisher's z_r:	1.40168
df:	109
r (two-tailed) 0.05:	0.186
r (two-tailed) 0.01:	0.242
r (one-tailed) 0.05:	0.157
r (one-tailed) 0.01:	0.220
t:	19.9192
df:	109
p (two-tailed):	< 0.001
p (one-tailed):	< 0.001

Spearmans's Rank-Order Correlation Coefficient	
Variable 1:	Th/U
Variable 2:	Gd (ppm)
r_S (tie corrected):	0.86812
n:	111
r_S (two-tailed) 0.05:	0.187
r_S (two-tailed) 0.01:	0.243
r_S (one-tailed) 0.05:	0.158
r_S (one-tailed) 0.01:	0.221
t:	18.26
df:	109
p (two-tailed):	< 0.001
p (one-tailed):	< 0.001
z [not recommended]:	9.10492
p (two-tailed):	< 0.001
p (one-tailed):	< 0.001

Pearson Product-Moment Correlation Coefficient	
Independent variable:	Th/U
Dependent variable:	Y (ppm)
r:	0.8206
Fisher's z_r:	1.15865
df:	109
r (two-tailed) 0.05:	0.186
r (two-tailed) 0.01:	0.242
r (one-tailed) 0.05:	0.157
r (one-tailed) 0.01:	0.220
t:	14.9908
df:	109
p (two-tailed):	< 0.001
p (one-tailed):	< 0.001

Spearmans's Rank-Order Correlation Coefficient	
Variable 1:	Th/U
Variable 2:	Y (ppm)
r_S (tie corrected):	0.801753
n:	111
r_S (two-tailed) 0.05:	0.187
r_S (two-tailed) 0.01:	0.243
r_S (one-tailed) 0.05:	0.158
r_S (one-tailed) 0.01:	0.221
t:	14.0056
df:	109
p (two-tailed):	< 0.001
p (one-tailed):	< 0.001
z [not recommended]:	8.40886
p (two-tailed):	< 0.001
p (one-tailed):	< 0.001

Pearson Product-Moment Correlation Coefficient	
Independent variable:	Th/U
Dependent variable:	Ti-in-zircon (°C)
r:	0.482919
Fisher's z_r:	0.526784
df:	109
r (two-tailed) 0.05:	0.186
r (two-tailed) 0.01:	0.242
r (one-tailed) 0.05:	0.157
r (one-tailed) 0.01:	0.220
t:	5.75771
df:	109
p (two-tailed):	< 0.001
p (one-tailed):	< 0.001

Spearmans's Rank-Order Correlation Coefficient	
Variable 1:	Ti-in-zircon (°C)
Variable 2:	Th/U
r_S (tie corrected):	0.551893
n:	111
r_S (two-tailed) 0.05:	0.187
r_S (two-tailed) 0.01:	0.243
r_S (one-tailed) 0.05:	0.158
r_S (one-tailed) 0.01:	0.221
t:	6.9095
df:	109
p (two-tailed):	< 0.001
p (one-tailed):	< 0.001
z [not recommended]:	5.7883
p (two-tailed):	< 0.001
p (one-tailed):	< 0.001

Pearson Product-Moment Correlation Coefficient	
Independent variable:	Hf (ppm)
Dependent variable:	Ti (ppm)
r:	-0.436989
Fisher's z_r:	-0.468504
df:	109
r (two-tailed) 0.05:	0.186
r (two-tailed) 0.01:	0.242
r (one-tailed) 0.05:	0.157
r (one-tailed) 0.01:	0.220
t:	-5.07223
df:	109
p (two-tailed):	< 0.001
p (one-tailed):	< 0.001

Spearmans's Rank-Order Correlation Coefficient	
Variable 1:	Hf (ppm)
Variable 2:	Ti (ppm)
r_S (tie corrected):	-0.413897
n:	111
r_S (two-tailed) 0.05:	0.187
r_S (two-tailed) 0.01:	0.243
r_S (one-tailed) 0.05:	0.158
r_S (one-tailed) 0.01:	0.221
t:	-4.74689
df:	109
p (two-tailed):	< 0.001
p (one-tailed):	< 0.001
z [not recommended]:	-4.34098
p (two-tailed):	< 0.001
p (one-tailed):	< 0.001

Pearson Product-Moment Correlation Coefficient	
Independent variable:	Hf (ppm)
Dependent variable:	Ti-in-zircon (°C)
r:	-0.429433
Fisher's z_r:	-0.459202
df:	109
r (two-tailed) 0.05:	0.186
r (two-tailed) 0.01:	0.242
r (one-tailed) 0.05:	0.157
r (one-tailed) 0.01:	0.220
t:	-4.96448
df:	109
p (two-tailed):	< 0.001
p (one-tailed):	< 0.001

Spearmans's Rank-Order Correlation Coefficient	
Variable 1:	Hf (ppm)
Variable 2:	Ti-in-zircon (°C)
r_S (tie corrected):	-0.414352
n:	111
r_S (two-tailed) 0.05:	0.187
r_S (two-tailed) 0.01:	0.243
r_S (one-tailed) 0.05:	0.158
r_S (one-tailed) 0.01:	0.221
t:	-4.7532
df:	109
p (two-tailed):	< 0.001
p (one-tailed):	< 0.001
z [not recommended]:	-4.34577
p (two-tailed):	< 0.001
p (one-tailed):	< 0.001

Pearson Product-Moment Correlation Coefficient	
Independent variable:	Th/U
Dependent variable:	Ti-in-zircon (°C)
r:	0.482919
Fisher's z_r:	0.526784
df:	109
r (two-tailed) 0.05:	0.186
r (two-tailed) 0.01:	0.242
r (one-tailed) 0.05:	0.157
r (one-tailed) 0.01:	0.220
t:	5.75771
df:	109
p (two-tailed):	< 0.001
p (one-tailed):	< 0.001

Spearmans's Rank-Order Correlation Coefficient	
Variable 1:	Ti-in-zircon (°C)
Variable 2:	Th/U
r_S (tie corrected):	0.551893
n:	111
r_S (two-tailed) 0.05:	0.187
r_S (two-tailed) 0.01:	0.243
r_S (one-tailed) 0.05:	0.158
r_S (one-tailed) 0.01:	0.221
t:	6.9095
df:	109
p (two-tailed):	< 0.001
p (one-tailed):	< 0.001
z [not recommended]:	5.7883
p (two-tailed):	< 0.001
p (one-tailed):	< 0.001

Spearmans's Rank-Order Correlation Coefficient	
Variable 1:	Model Age (ka)
Variable 2:	Ti-in-zircon (°C)
r_S (tie corrected):	0.428841
n:	108
r_S (two-tailed) 0.05:	0.190
r_S (two-tailed) 0.01:	0.247
r_S (one-tailed) 0.05:	0.160
r_S (one-tailed) 0.01:	0.224
t:	4.8874
df:	106
p (two-tailed):	< 0.001
p (one-tailed):	< 0.001
z [not recommended]:	4.43596
p (two-tailed):	< 0.001
p (one-tailed):	< 0.001

Appendix D. Electronic datasets

All raw datasets for LA-ICPMS, SIMS and Ar/Ar geochronology are available in the Scholars@OSU Collections, available online to the public through the Oregon State University Libraries.

Item Record:
Murphy, Bethany; de Silva, Shanaka (2015): Datasets from Upper-Crustal Magma Evolution at Intermediate Arc Systems: Uranium-Series Zircon Chronochemistry of the Unzen Volcanic Complex, Southwestern Japan. Oregon State University Libraries. Dataset. http://dx.doi.org/10.7267/N98G8HMR.